PREDICTIVE/ADAPTIVE STEERING
FOR THE
ATMOSPHERIC BOOST PHASE OF A SPACE VEHICLE

by

ARTHUR HIRONARI OZAKI

B.S.M.E., Massachusetts Institute of Technology
(1982)

Submitted in Partial Fulfillment
of the Requirements for the
Degree of

MASTER OF SCIENCE
in
MECHANICAL ENGINEERING

at the

MASSACHUSETTS INSTITUTE OF TECHNOLOGY

June 1987

Signature of Author _____
Department of Mechanical Engineering
August 1987

Certified by _____
Professor Ernesto E. Blanco
Thesis Advisor

Approved by _____
Gilbert S. Stubbs
CSDL Project Manager

Accepted by _____
Ain A. Sonin
Chairman, Department Thesis Committee

Predictive/Adaptive Steering
for the
Atmospheric Boost Phase of a Space Vehicle

by

Arthur Hironari Ozaki

Submitted to the Department of Mechanical
Engineering in partial fulfillment of the
requirements for the degree of Master of Science
in Mechanical Engineering

ABSTRACT

A new predictive/adaptive steering method, along with a new thrust-mass estimator which supplies the steering method with current estimates of thrust and mass throughout the trajectory, were developed for the Stage I atmospheric boost phase of a multi-stage, solid-rocket, single-gimballedengine boost vehicle. The predictive steering method employs a simple vehicle simulation which periodically integrates along a zero angle of attack trajectory from current state to engine burnout. If the targeted end condition is not met at simulated engine burnout, the steering command is modified to meet desired end conditions by interpolation/extrapolation. The predictive steering method is an improvement over conventional systems in that it can adapt to off-nominal conditions such as unexpected thrust variations which continually act to perturb the vehicle from its desired trajectory. By following the low angle of attack trajectory to the desired dynamic pressure at staging, the loads normal to the vehicle longitudinal axis are minimized.

The steering methods investigated in this thesis are designed under the principle of controlling the direction of the vehicle's earth-relative velocity vector, also referred to as flight path angle, to a desired trajectory. In conjunction with the steering method, an angle of attack feedback control system is used. The performance of the predictive steering method was compared to a steering method based on a functional relationship between flight path angle and time.

The stability of the steering system was also evaluated. Extensive simulation studies of the predictive steering system to analyze its behavior and therefore determine system effectiveness were performed.

ACKNOWLEDGEMENTS

The past two years here at MIT and Draper have been an experience that I will not forget. The task of completing a master's degree program at MIT was a difficult one for me and at times it seemed almost impossible, but I can now see the light at the end of the tunnel and reflect on all that has happened during the past two years. I would like to thank the following individuals for whom without their help all of this would not have been possible.

I would like to thank Mr. Gilbert S. Stubbs for taking the time to sit down with me and teach me the fundamentals of spacecraft steering and control design. He provided the concepts for the predictive steering and thrust-mass estimator discussed in this thesis and spent countless hours helping me develop them. Additionally, I would like to thank him as well as The Charles Stark Draper Laboratory for giving me the opportunity to attend graduate school by granting me the Draper Fellowship.

I am grateful to Mr. Richard D. Goss for his constant encouragement and for teaching me to be thorough in my analysis techniques.

Finally, I would like to thank Prof. Ernesto E. Blanco for his constant encouragement and support over the past years. His advise has also been greatly appreciated.

This report was prepared at The Charles Stark Draper Laboratory, Inc. under Contract F04704-85-C-8081 with the Ballistic Missile Office of the Air Force Systems Command.

Publication of this report does not constitute approval by the Draper Laboratory or the sponsoring agency of the findings or conclusions contained herein. It is published for the exchange and stimulation of ideas.

_____

Arthur Hironari Ozaki

TABLE OF CONTENTS

TABLE OF CONTENTS (Cont.)

TABLE OF CONTENTS (Cont.)

TABLE OF CONTENTS (Cont.)

LIST OF FIGURES

LIST OF FIGURES (Cont.)

LIST OF FIGURES (Cont.)

LIST OF TABLES

LIST OF TABLES (Cont.)

CHAPTER 1

INTRODUCTION

This thesis presents a new predictive/adaptive steering method for the first stage of a symmetrical launch vehicle which is controlled by a two degree of freedom gimballed engine nozzle. In addition, a thrust-mass estimator was developed to supply the steering system with current values of thrust and mass. The steering method is designed to shape the trajectory in the pitch plane with the sideslip angle commanded to be zero. In addition to the predictive steering method, both an exponential and a logarithmic fixed functionalized steering method are described. The latter two systems are compared and, based on simulation results, one is selected for comparison with the predictive steering method. In all of these steering methods, the steering loop is designed to control the direction of the earth-relative velocity vector, also known as the flight path angle, in conjunction with either an attitude or angle of attack control system. The predictive steering method is designed for use with an angle of attack control system and the stability analysis of this steering method will include its interaction with the control system.

Previous uses of the flight path angle steering philosophy are described in theses by Bonnice [1], Fader [2], and Dailey [3] and are briefly outlined below.

1.1 History of Velocity Direction Steering Method Development

The objective of the steering methods is to produce desired end conditions through a boost trajectory in which transverse loads to the

vehicle are kept at a minimum. Since the loads are proportional to the product of dynamic pressure q times angle of attack α the minimization of these loads involves minimizing the $q\alpha$ product. This is done by carrying out the steering in two phases. The first of these phases is a rapid pitchover to initialize the second phase; the second phase is a near zero angle of attack trajectory to reach the desired end conditions. The first phase, called the "launch maneuver" minimizes $q\alpha$ by completing the maneuver before q grows to a significant level. The steering during this first phase is designed to produce an initial velocity vector orientation for the second phase that will allow the desired end conditions at engine burnout to be achieved with a near zero angle of attack trajectory. Thus in the first phase q is small and in the second phase α is small, such that the $q\alpha$ product is minimized in both phases.

Bonnice, Fader and Dailey all relied primarily on attitude control to implement the launch maneuver. Bonnice accomplished this by retaining the estimated angle of attack feedback during the maneuver, but modified the estimator so that its output was essentially an attitude signal. Fader employed a separate attitude feedback in the launch maneuver and commanded a predetermined fixed attitude during the maneuver. Dailey also employed attitude feedback but used a more sophisticated algorithm developed by James Herner of Autonetics in which the commanded attitude was varied continuously during the maneuver in such a way as to produce close to zero angle of attack as well as a desired attitude at the end of the maneuver. In this thesis we shall also employ the Autonetics launch maneuver implementation.

For any of the launch maneuver systems, large deviations can occur in the desired vehicle state at the end of the maneuver. These variations can be the result, for example, of unpredicted thrust levels or thrust transients, wind distubances, and unmodelled changes in the initial attitude of the vehicle at launch. The ability of the steering and control system to accommodate these variable conditions at the end of

the launch maneuver as well as other disturbances encountered subsequently was the major problem addressed by Bonnice, Fader and Dailey, and will also receive primary attention in this thesis.

Bonnice, Fader and Dailey all employed flight path angle steering in combination with angle of attack control for the period subsequent to the launch maneuver. The "flight path angle" (γ) is defined as the angle between the earth-relative velocity vector and the horizontal. Bonnice employed an exponential function of time to generate the commanded flight path angle. This function was selected to produce a trajectory having a small angle of attack during the entire Phase 1 boost phase subsequent to the launch maneuver. Bonnice's method gave excellent control of the flight path angle but the terminal altitude and resulting terminal dynamic pressure were sensitive to winds, off-nominal launch conditions and thrust variations. Fader also used a predetermined function to define a reference trajectory, but made altitude as the primary reference variable rather than velocity direction. The altitude was tabulated or functionalized in terms of sensed velocity and was based on a zero angle of attack trajectory to a desired terminal dynamic pressure. He derived and commanded a reference flight path angle based on the slope of the altitude function and then augmented this commanded reference angle by a term proportional to the error between estimated and reference altitude. Fader's approach gave better control of terminal altitude and terminal dynamic pressure than Bonnice's method, but suffered some disadvantages inherent in attempting to use an add-on altitude loop to force both the altitude and velocity of the vehicle to follow a reference trajectory.

Dailey explored the possiblity of interpolating between three reference trajectories terminating at three different flight path angles but resulting in the same dynamic pressure. He generated these three reference trajectories for each of three values of thrust, assumed constant over the entire boost phase. The steering trajectory was then selected by interpolating between the reference trajectories on the basis

of estimated thrust. Although Dailey's approach yielded better performance than the previous methods, it required a large memory allocation for its functionalization. Furthermore, like the previous methods, Dailey's use of prelaunch functionalization had some inherent disadvantages such as the need to refunctionalize for changes in vehicle payload and other parameters and the inability to compensate for effects of unanticipated inflight conditions such as the effect on thrust of unmeasured temperature gradients in the booster.

1.2 Predictive/Adaptive Steering

The predictive/adaptive steering method is considerably more flexible than the above steering methods, and offers the possiblity of improved performance because it can adapt to unanticipated inflight conditions. This method employs a simple vehicle simulation in the on-board computer to periodically integrate along a zero-angle-of-attack trajectory from the current state to the point of engine burnout. If the predicted burnout state (e.g., dynamic pressure) differs from the desired state, the simulation will proceed to (1) perturb the current flight path angle, (2) repeat the integration to burnout and (3) interpolate or extrapolate between first and second integration results to obtain a flight path angle that will produce the desired end state. The flight path angle obtained by this predictive integration is employed to update a steering algorithm that is used until the next periodic predictive integration. Although some functionalizations of vehicle properties is required in the predictive/adaptive approach, it avoids the steering functionalizations of previous methods and the problems of lack of flexibility and adaptability associated with these functionalizations. For the sake of brevity the term "predictive/adaptive steering" will henceforth be simplified to "predictive steering".

To evaluate the relative merits of the predictive steering method, its performance will be compared to the performance of a fixed functionalized steering method. Initially, two fixed functionalized

steering methods, based on exponential and logarithmic functions of time, will be investigated and one will be selected based on performance for comparison with the predictive method.

The primary advantages of the fixed functionalized steering methods is that they are simple and therefore are easy to implement in the flight computer. However, accuracy in achieving desired end conditions is decreased due to the steering system's inability to effectively compensate for off-nominal inflight conditions. The predictive steering method, on the other hand, is a more complicated system with greater computational requirements. It does, however, meet end conditions more effectively under a variety of off-nominal flight conditions.

It may be possible to design a predictive steering system for a variety of choices of steering and control variables, including the conventional approach of acceleration direction steering combined with attitude control with an additional feedback loop for load relief. However, the use of flight path angle (velocity direction) steering in combination with angle of attack control offers the following advantages:

(1) Velocity direction (or flight path angle) is in itself a potentially important variable which might be specified in lieu of dynamic pressure as an end-of-stage condition, depending on vehicle design and mission requirements.

(2) Velocity direction and angle of attack are particularly compatible as outer and inner loop variables since the former is proportional to the integral of the latter variable. (See Chapter 6.)

(3) By using the steering to command the angle of attack it is possible to precisely constrain the effects of steering on vehicle loads by limiting the commanded angle of attack to a value compatible with a load-related limit on the product of angle of attack α and dynamic pressure q.

1.3 Control System

The angle of attack control system to be used in this thesis for predictive steering is of the same form considered by Bonnice, Fader, and Dailey. The control gains chosen for the angle of attack system do not differ greatly from those chosen for an attitude control system, since attitude and angle of attack tend to be proportional in the frequency range determining rigid-body stability. As originally described by Bonnice, the angle of attack control system employs a complementary filter estimator in which measured ΔV increments normal to the vehicle longitudinal axis and measured nozzle deflections, δ, are used for low frequencies and measured attitude increments $\Delta\theta$ are used for high frequencies. The estimator updates the angle of attack every control cycle based on ΔV and $\Delta\theta$ increments over the past cycle in conjunction with the current values of measured nozzle deflections.

Integrations are employed along with proportional gains in the forward paths of both the angle of attack control and predictive steering loops. The effects of these integrations and the various proportional-signal gains will be examined in linear stability analyses presented in Chapter 6 of this thesis.

1.4 Thrust-Mass Estimator

A thrust-mass estimator was developed to supply the new predictive/adaptive steering method with values of thrust and mass at steering update times over the entire boost trajectory. It uses attitude and acceleration measurements obtained from the inertial measurement unit (IMU) as primary inputs. Also, it uses estimated angular rate in pitch and yaw to correct for centripetal acceleration effects and employs estimated atmospheric pressure on thrust to compensate for effects of the atmospheric pressure on thrust.

1.5 Thesis Outline

The material to be presented in the remainder of this thesis is summarized as follows:

Chapter 2: Overall vehicle description including vehicle dynamics, propulsion, control and steering system.

Chapter 3: Derivation of the predictive/adaptive steering method.

Chapter 4: Description and evaluation of the thrust-mass estimator.

Chapter 5: Derivations of both the logarithmic and exponential functionalized steering methods: both steering methods are compared and, based on the performance results, one method is selected for comparison with the predictive steering method.

Chapter 6: Stability analysis of the steering and control loops.

Chapter 7: Simulation results comparing performances of the predictive/adaptive steering method with the selected functionalized steering method.

Chapter 8: Conclusions and Recommendations.

CHAPTER 2

SYSTEM DESCRIPTION

2.1 Vehicle

2.1.1 Description

The vehicle used in this thesis is a multistage spacecraft propelled by a solid propellant booster with a gimballed nozzle. It is approximated by a rigid body model. The vehicle mass is assumed to be symmetrically distributed about the roll, pitch, and yaw axes. Therefore, the product of inertia terms are zero. The center of gravity (cp), center of pressure (cp), and nozzle hinge point (hp) are assumed to always lie along the longitudinal (roll) axis. The cp moves along this axis as the Mach number changes and the cg moves along this axis as the propellent is expended.

The thrust vector is directed by a two degree of freedom gimballed nozzle. The nozzle deflection is limited to six degrees relative to the vehicle roll axis and the nozzle rate is limited to 40 deg/sec. The nozzle actuator dynamics are represented by a linear second order model with a natural frequency of 10 Hz (62.8 rad/sec) and a damping ratio of 0.5.

The on-board navigation system provides values of inertial velocity and position in inertial space. An estimator, which is described in Chapter 4, provides values of thrust, mass, and mass flow rate. The specific impulse is assumed to be constant.

2.1.2 Pitch Plane, Lateral, Translational Vehicle Dynamics

For the analysis and simulation of pitch plane steering methods, it is necessary to express the acceleration normal to the vehicle longitudinal axis as a function of the thrust, aerodynamic, and gravity forces acting on the vehicle. (See Figure 2-1.)

The normal acceleration is given by the following relationship

$$a_{np} = \frac{1}{M}\left[F \sin(\alpha_p - \alpha_{p_w} - \delta_p) - F_A \sin(\alpha_p - \alpha_{p_w}) - F_N \cos(\alpha_p - \alpha_{p_w}) - M g \cos \gamma\right] \quad (2.1)$$

where

M = Mass of vehicle

g = Acceleration due to gravity

F = Engine thrust

F_A = Axial aerodynamic force on the vehicle

F_N = Vehicle body z axis component of the aerodynamic force normal to the vehicle x axis.

α_p = Angle of attack in pitch

α_{p_w} = Angle between the earth-relative and and air-relative vehicle velocity vectors in the pitch plane.

γ = Flight path angle

δ_p = Nozzle deflection in the vehicle body pitch plane.

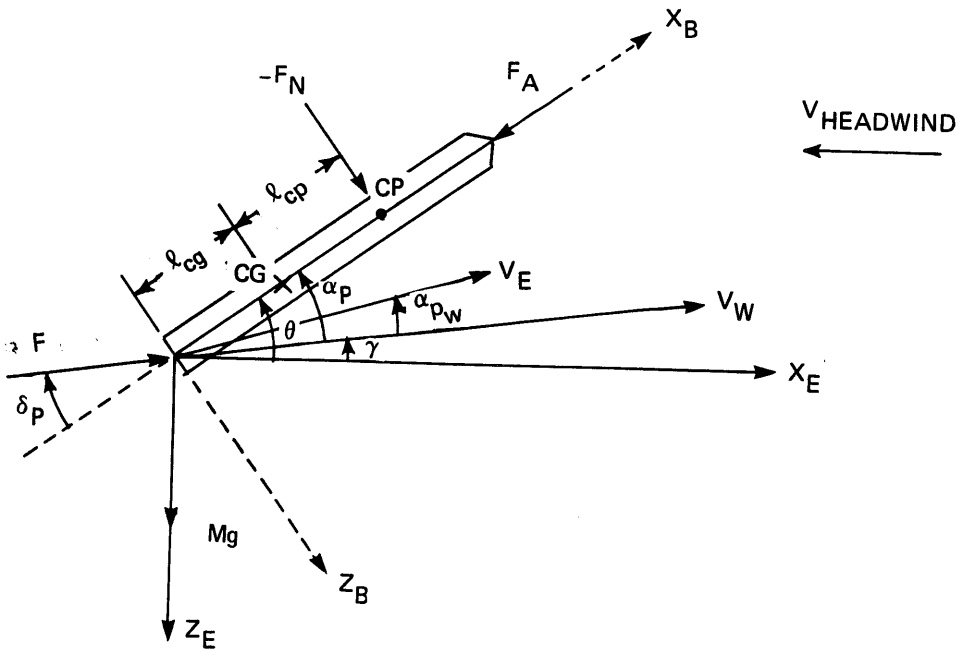

Figure 2-1. Pitch plane forces.

2.2 Propulsion Models

To thoroughly evaluate the performance of predictive steering in comparison to fixed functionalized steering methods, several thrust profiles were employed. To generate these profiles several assumptions were made. As previously mentioned, the specific impulse is assumed to be constant throughout the trajectory. It is also assumed that the fuel is completely expended by burnout. A nominal, constant thrust profile is simulated along with a variety of other profiles. Although the profiles have different shapes each profile is designed such that the total impulse remains the same, thereby producing the same burnout mass.

The total impulse is defined as

$$\text{Total Impulse (Constant)} = \int_{t_2}^{t_1} F \, dt = \Delta m \, I_{sp} \, g \qquad (2.2)$$

where:

t_1 = ignition time

t_2 = burnout time

Δm = total mass change from t_1 to t_2

The selected thrust profiles are as follows:

(1) Nominal, Constant Thrust Profile

(2) Off-nominal Constant Thrust Profile

(3) Temperature Gradient Profile

(4) Sawtooth Thrust Profile

Profiles (2) and (3) were derived from the nominal profile by a set of relationships that are also used in predictive steering. These relationships, derived in Appendix A, provide a means for modifying a thrust profile described by tabulated values of thrust, mass and time. The relationships modify the time values to be consistant with new values of thrust versus mass, with the burnout mass unaltered. Profile (4) was designed to represent thrust fluctuations for the same burnout mass of the other profiles. A more detailed description of the above profiles follows:

2.2.1 Nominal, Constant Thrust Profile

The constant thrust profile represented in Figure 2-2 is used as an initial test of the performances of the steering methods. This profile has an initial rise period of one-second duration in which thrust is assumed to rise linearly and a final thrust tailoff period of one-second duration in which thrust is assumed to decrease linearly to zero.

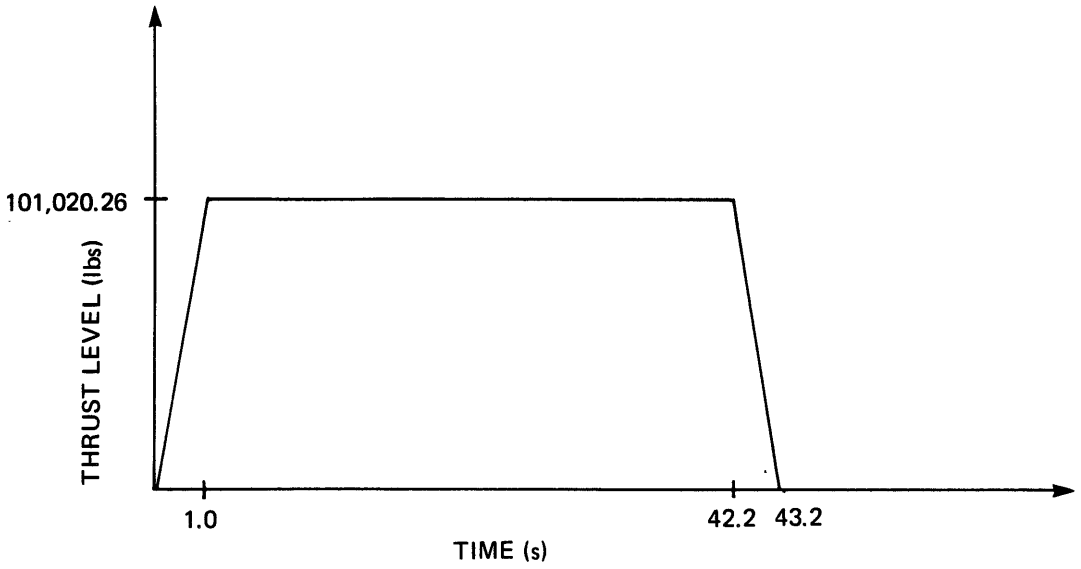

Figure 2-2. Nominal, constant thrust profile (not to scale).

2.2.2 Off-Nominal Profiles

Constant Thrust Profile

Off-nominal constant thrust profiles are used to evaluate the ability of the steering methods to adapt to thrust values which are either higher or lower than expected over the entire trajectory due to off-nominal temperatures at launch. The nominal constant thrust profile is scaled by a constant factor, KBURN2, which has the values of either .9 or 1.1 representing 10% below and 10% above nominal thrust levels respectively. Figure 2-3 illustrates these profiles and their relationship to the nominal thrust profile which has a KBURN2 value of 1.0 .

This concept of scaling thrust profiles is used in flight for the predictive steering method. The reference thrust profile is scaled by a factor K_B, which is the ratio between the estimated and nominal thrust values, at every update time, thus allowing the steering method to follow thrust transients.

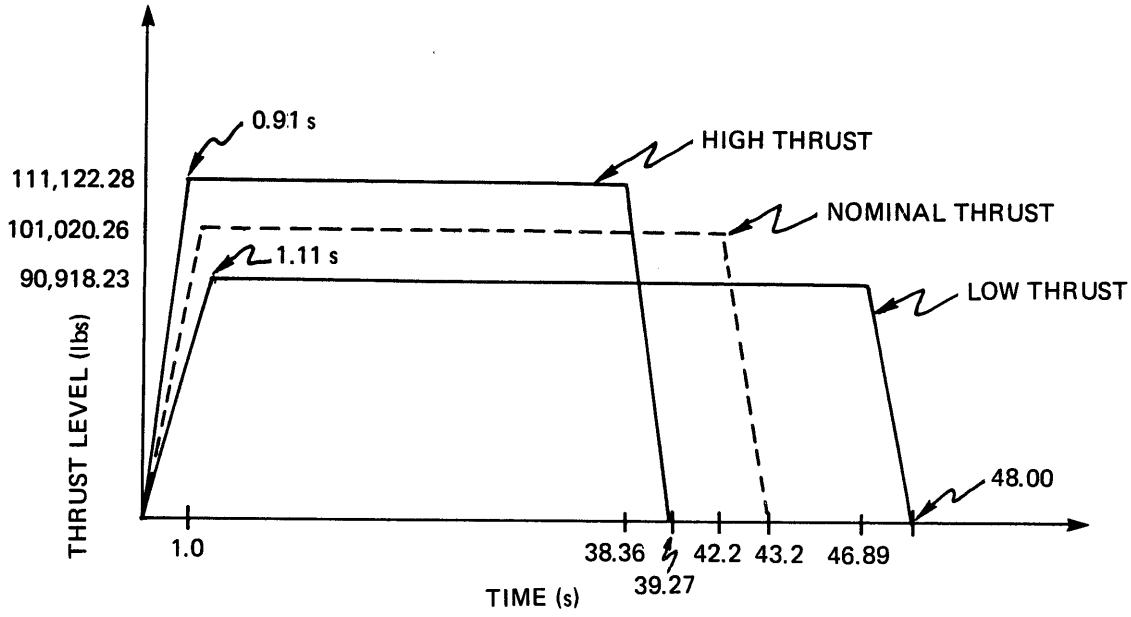

Figure 2-3. Off-nominal constant thrust profiles (not to scale).

Temperature Gradient Profile

The effect on thrust of a temperature gradient is simulated to evaluate the response of the steering methods to variations in thrust caused by temperature deviations. The gradient is simulated by a thrust that increases linearly with time to a specified percentage above nominal. Figure 2-4 gives an example of a 10% thrust gradient, which is a profile that deviates from the nominal thrust value by 10% just before tailoff.

Sawtooth Thrust Profile

The sawtooth thrust profile, shown in Figure 2-5, is used to evaluate the steering methods response to variable thrust. The sawtooth profile varies a maximum of $\pm$ 4% from the nominal value of 100,000 lbs. This profile has the same one-second thrust rise and tailoff characteristics of the nominal, constant thrust profile.

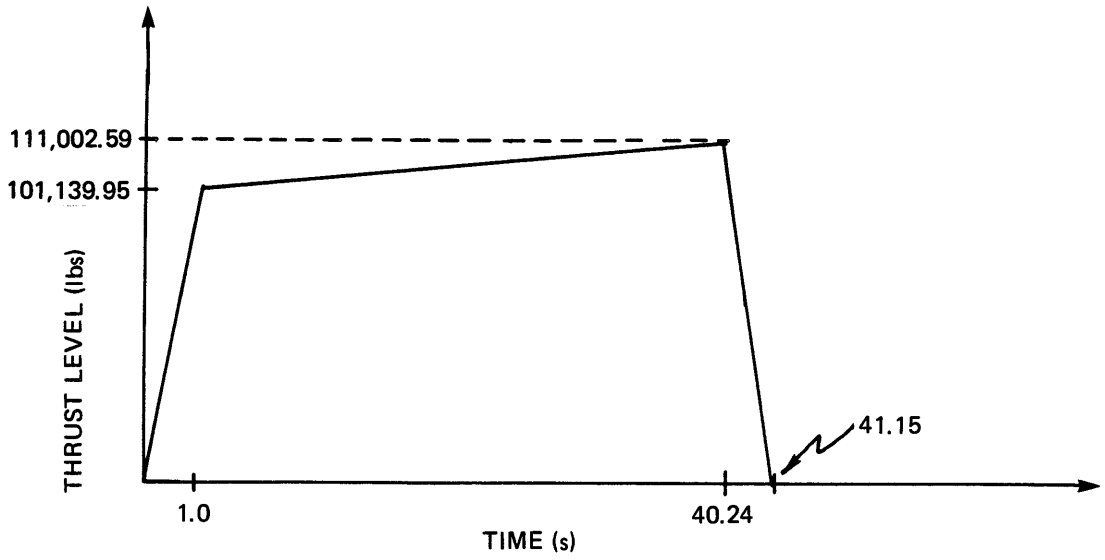

Figure 2-4. 10% thrust gradient profile (not to scale).

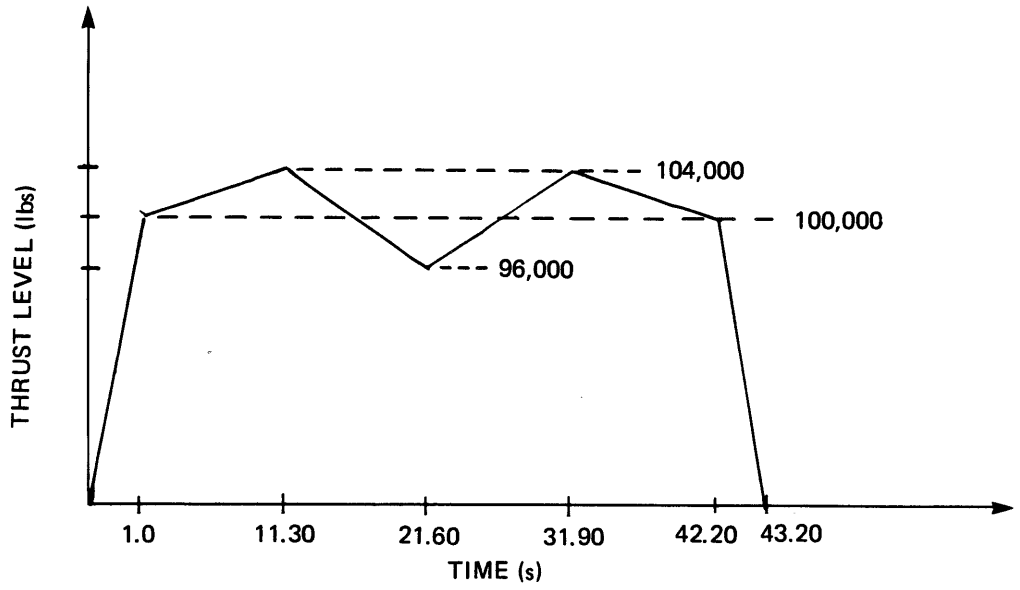

Figure 2-5. Sawtooth thrust profile (not to scale).

2.3 Launch Conditions

Three different launch conditions are utilized in this study to investigate the adaptability of the predictive steering method in comparison to the fixed functionalized steering methods to off-nominal launch angles. A nominal launch angle of 90 deg (which is a vertical launch) is employed along with off-nominal launch angles of 62 and 119 deg in the pitch plane.

2.4 Atmospheric Conditions

The atmospheric conditions simulated are air density, atmospheric pressure, and winds. Values for air density and atmospheric pressure were obtained from US Standard Atmospheric Tables and were approximated by curve fitting.

A wind profile given in Figure 2-6 was used to evaluate the vehicle's response to wind disturbances. The wind profile (velocity vs. altitude) is simulated as occurring in a single plane and can be specified as a tail wind, head wind or cross wind. The profile covers an altitude range from sea level to 100,000 ft. The profile has a wind spike introduced at an altitude of 30,000 ft with a maximum speed of 265 ft/sec.

2.5 Overall Steering and Flight Control System

The steering and control systems used during the stage I boost phase are designed for three separate phases: a rapid pitchover maneuver called the launch maneuver ($0 < t < t_{kick}$), a trajectory phase ($t_{kick} < t < t_{tailoff}$) and a tailoff period ($t_{tailoff} < t < t_{burnout}$).

2.5.1 Steering

The purpose of the steering system is to generate flight path angles that will guide the vehicle to the desired end conditions. The steering commands are generated at a sample period of 100 ms (0.1 sec).

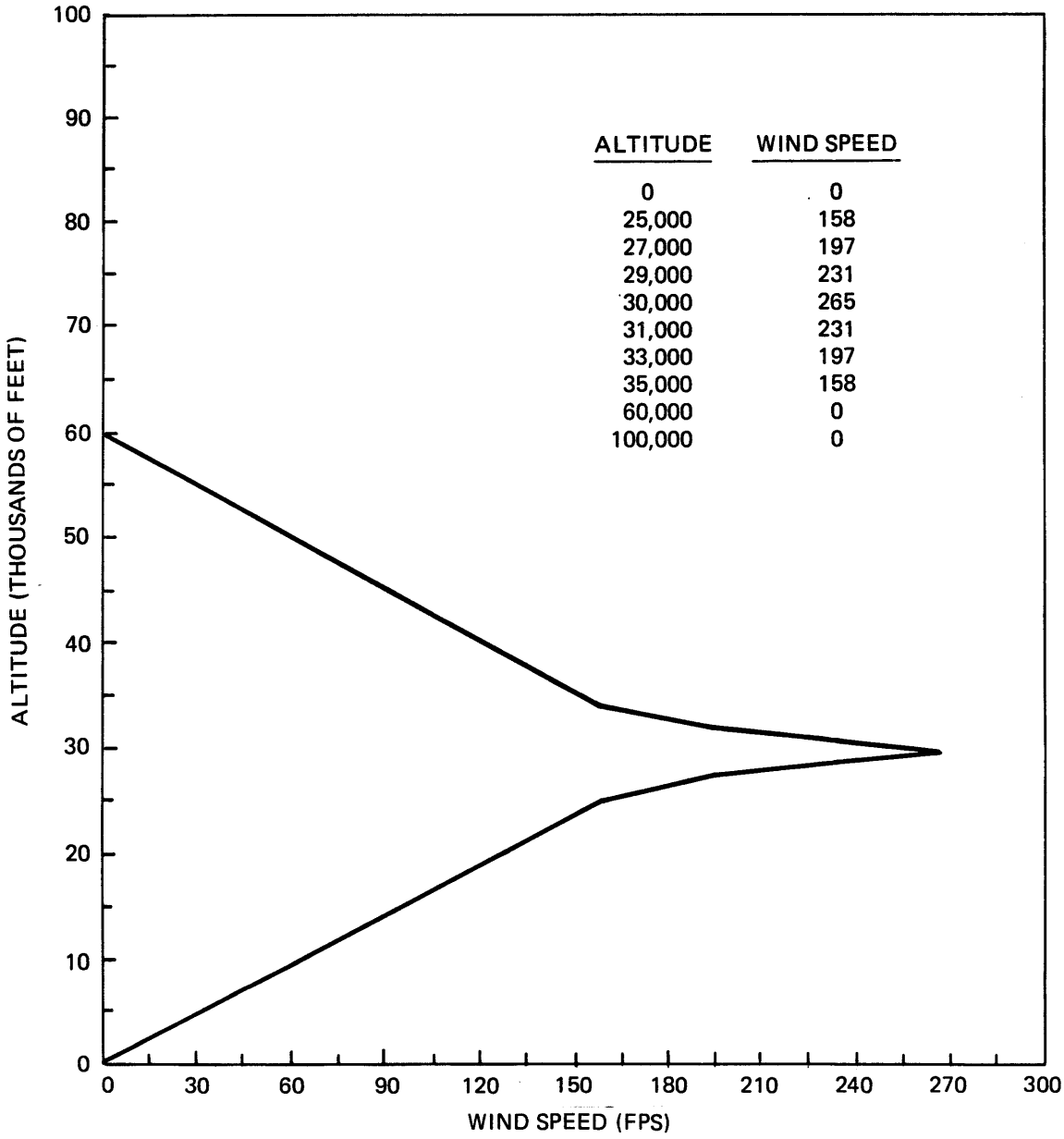

Figure 2-6. Wind profile (altitude vs wind speed).

During the first 12 seconds after ignition the launch maneuver is implemented. The purpose of the launch maneuver is to pitch the vehicle over at a sufficiently high rate so as to intersect the zero angle of attack trajectory that terminates in the desired conditions at the end of the Stage I boost phase. This maneuver is performed during the initial stage of the trajectory while the product of dynamic pressure and total angle of attack ($q\alpha$) is low so that loads normal to the vehicle are small. The maneuver is adapted from the Autonetic's launch maneuver [4]. The launch maneuver itself consists of two phases: The first phase is an initial rapid pitchover to a flight path angle, γ_0. The next phase starts from γ_0 and uses a constant pitchover rate computed to achieve the desired flight path angle, γ_{kickf}, at launch maneuver termination. Although this maneuver does not achieve as high a velocity at the end of the maneuver as a constant rate pitchover maneuver, the benefits achieved in fuel expenditure minimization and angle of attack reduction at the end of launch manuever outweigh this disadvantage.

During the zero-alpha trajectory phase, which follows the launch maneuver, one of the three velocity direction steering methods being investigated in this thesis is implemented. These three steering methods are exponential, logarithmic, and predictive. In velocity direction steering the difference between commanded flight path angle and the actual flight path angle is used to generate the angle of attack command necessary to correct for this discrepancy (See Figure 2-7).

During the tailoff period the steering loop gain is set to zero, so that the angle of attack input to the control loop is zero.

2.5.2 Control

The purpose of the flight control system is to follow the steering commands while stabilizing the vehicle. The control system is updated at a sample rate of 10 ms (.01 secs).

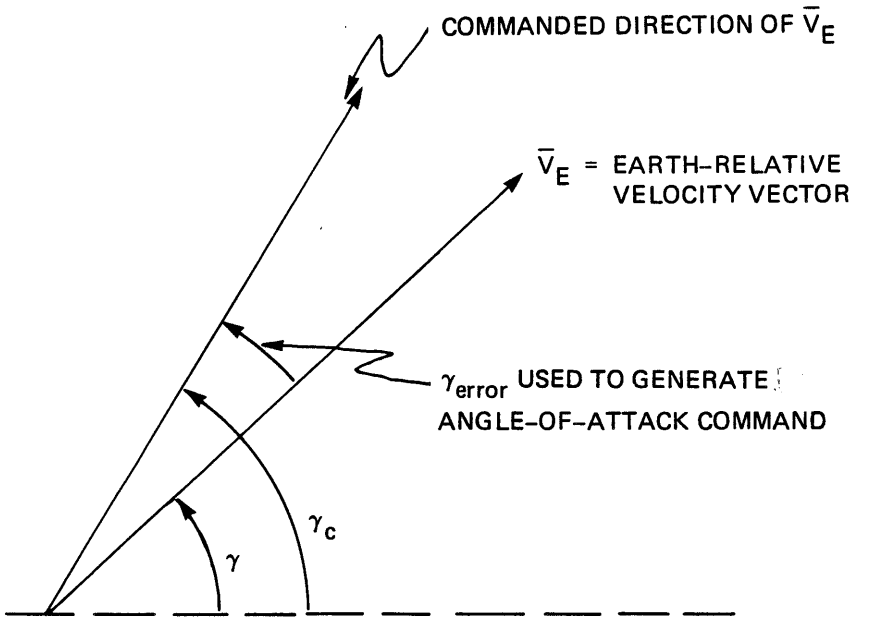

Figure 2-7. Flight path angle (velocity-direction) steering illustrated in pitch plane.

For both the kick maneuver and zero-alpha trajectory phases there are two feedback control loops: an inner and an outer loop. The inner loop of both phases uses attitude rate feedback. The outer loop of the kick maneuver uses attitude feedback (See Figure 2-8), and the outer loop of the zero-alpha trajectory phase uses angle of attack feedback (See Figure 2-9). The angle of attack feedback control system was initially designed by Bonnice [1] and will not be discussed here.

During the tailoff phase, zero angle of attack is commanded, so that transients at tailoff can be kept to a minimum.

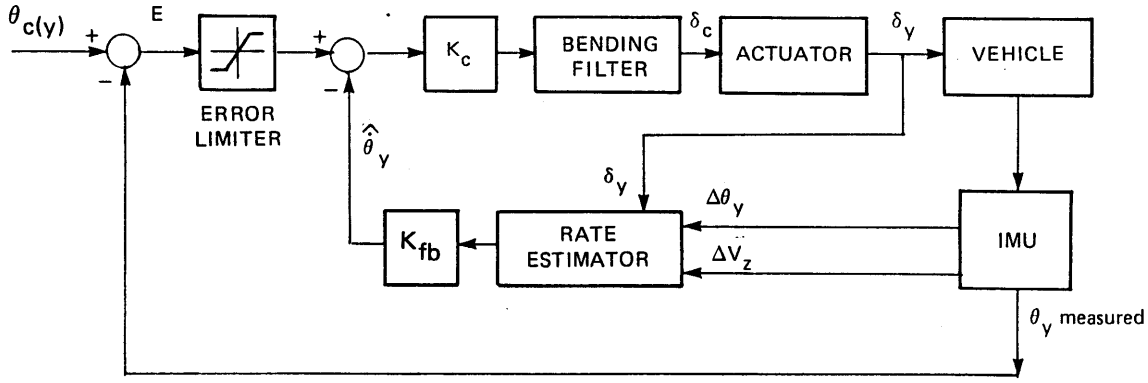

Figure 2-8. Functional block diagram of the attitude control loop (for the pitch axis in the launch maneuver).

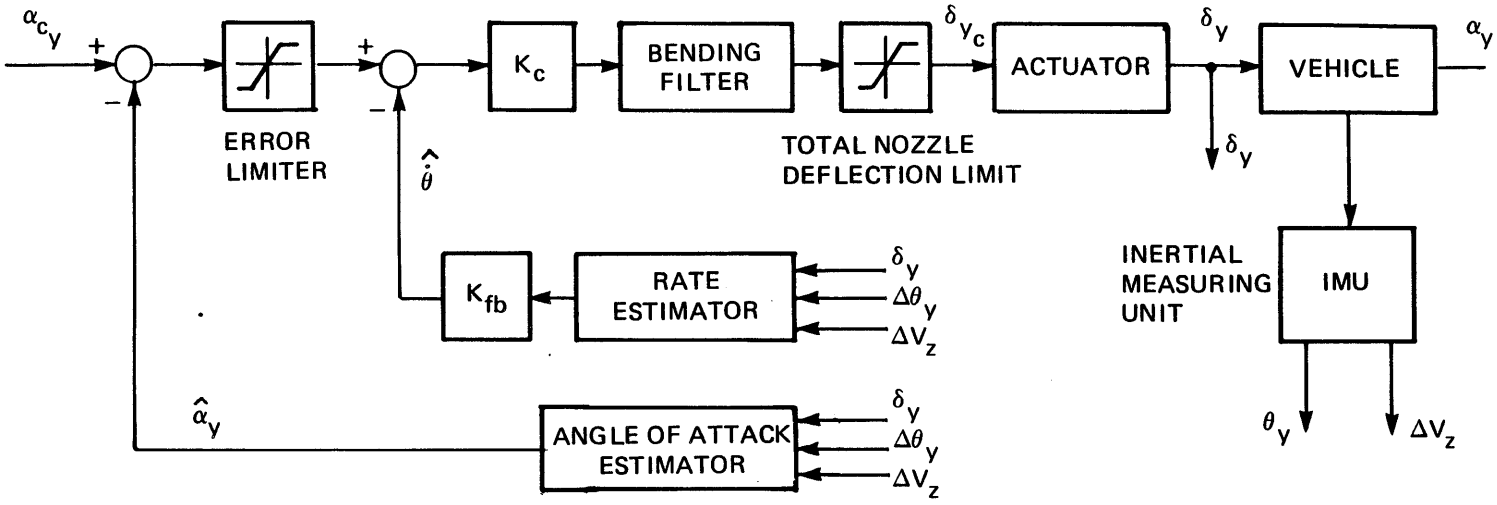

α_{c_y} ANGLE OF ATTACK COMMAND

α_y ANGLE OF ATTACK

$\hat{\alpha}_y$ ESTIMATED ANGLE OF ATTACK

$\hat{\dot{\theta}}_y$ ESTIMATED ATTITUDE RATE IN X_c-Z_c PLANE

δ_{y_c} COMMANDED ENGINE NOZZLE DEFLECTION IN THE X_c-Z_c PLANE

δ_y ENGINE NOZZLE DEFLECTION IN THE X_c-Z_c PLANE

θ_y ATTITUDE OF THE VEHICLE IN THE X_c-Z_c PLANE

ΔV_z MEASURED CHANGE IN VELOCITY SENSED BY ACCELEROMETERS RESOLVED ALONG THE Z_c AXIS EVERY CONTROL LOOP SAMPLING TIME (THIS DOES NOT INCLUDE THE EFFECTS OF GRAVITY)

K_{fb} ATTITUDE RATE FEEDBACK GAIN

K_C FORWARD LOOP GAIN

Figure 2-9. Functional block diagram of the angle of attack control loop for the pitch axis.

CHAPTER 3

PREDICTIVE STEERING: THEORY

3.1 Introduction

The predictive steering concept is designed to put a vehicle on a zero angle of attack trajectory that will achieve a desired end condition. The end condition can be specified as earth-relative velocity, height, or dynamic pressure. In this thesis dynamic pressure is chosen as the desired end condition. The performance of the predictive steering method will be compared to the performance obtained from a fixed functionalized steering method which will be described in Chapter 5. The primary advantage of the predictive steering concept is its flexibility in adapting to off-nominal flight conditions. The steering method adapts to these conditions by periodically computing through predictive inflight simulations the value of current velocity direction (flight path angle) that would put the vehicle on a zero angle of attack trajectory to the desired end condition. The inflight simulation, which starts at the current vehicle state, includes the effects of perturbations in velocity, altitude, vehicle mass and engine thrust that are ignored in the fixed functionalized steering approach. The predicitive steering thereby compensates for effects of any off-nominal conditions that occur before launch or during the boost phase. Such off-nominal conditions could include (1) variations in the initial launch attitude, (2) changes in the thrust characteristics resulting from unmodelled variations in the composition and temperature of the rocket grain and (3) wind disturbances.

3.2 Basic Concept

The periodic inflight predictions involve two trial-and-error inflight simulations that are performed to determine the value of current flight path angle, γ, that will put the vehicle on a zero angle of attack trajectory leading to the desired end condition. The first of these simulations is initialized at the current vehicle state with the flight path angle equal to the current value. The deviation from the desired end condition produced by this first simulation is stored and utilized in determining a different initial flight path angle for a second trial simulation. The first and second end conditions are compared to the desired end conditions to estimate a value of current γ that will produce the desired conditions. This estimated value of required γ is supplied as the steering command. The command is then decremented at each steering cycle time to compensate for the change in γ produced by gravity over the steering interval. This process is continued until the next predictive simulation time. Options that deviate from this basic approach are examined subsequently in this thesis.

The procedure for generating the commanded flight path angle may be described in terms of the following steps:

(1) At each predition time, determine the following "initial conditions":

(a)	vehicle altitude	From IMU Measurements
(b)	vehicle earth-relative velocity	From Navigation Routine
(c)	flight path angle	
(d)	thrust	From Thrust-mass Estimator
(e)	mass	

(2) From initial conditions given in (1), simulate a zero angle of attack trajectory to thrust burnout to determine the final value of dynamic pressure.

(3) Increment the flight path angle initial condition given in (1) by a specified amount, in a direction to reduce the error between the dynamic pressure of (2) and the desired pressure, keeping all other initial conditions the same.

(4) From the new set of initial conditions simulate a second zero angle of attack trajectory to thrust burnout to determine a second value of dynamic pressure

(5) From the two values of dynamic pressure at burnout and the corresponding initial values of flight path angles at the update time, interpolate (or extrapolate) to determine the flight path angle that will yield the desired dynamic pressure at burnout.

3.3 Implementation of Predictive Simulation

Ideally it would be desirable to perform the predictive simulations to generate a new commanded flight path angle every steering cycle. However, it is assumed that throughput limitations of the flight computer will permit these simulations to be performed only at intervals of N_{steer} steering cycles. It is further assumed that throughput limitations result in a time delay of $COUNT_{delay}$ steering cycles between the initiation of the predictive simulations and the updating of the steering algorithm based on these simulations.

The time line of the steering computations is shown in Figure 3-1. The predictive simulations are initiated at the points A, separated by N_{steer} steering cycles. The steering command based on the predictive simulations is introduced at the points B, $COUNT_{delay}$ cycles beyond the points A. In the example given in Figure 3-1, the predictive simulations are performed every 2.5 sec (N_{steer} = 25 steering cycles) and the updates are delayed by 0.2 sec ($COUNT_{delay}$ = 2 steering cycles).

The predictive steering computations can be separated into three categories: (1) computations initiated at point A, (2) computations implemented at point B, and (3) computations performed every steering cycle.

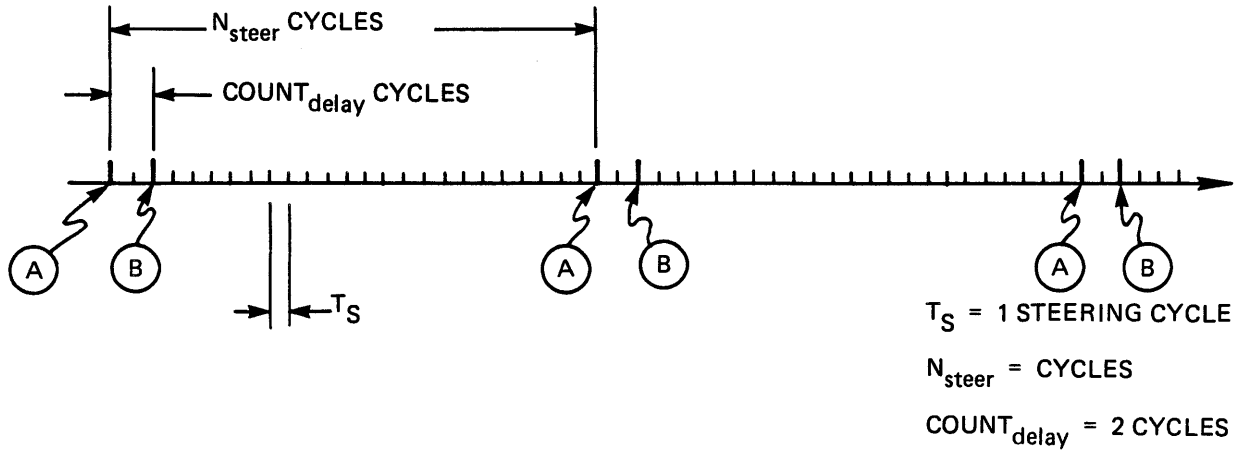

Figure 3-1. Predictive steering time line.

3.3.1 Computations Initiated at Point A

The following computations are performed at every prediction time using the values obtained from the current vehicle state.

(1) Save the flight path angle at time A as γ_{sim1}.

(2) Simulate zero angle of attack trajectory from A until the time at which the propellant is completely expended. (All simulations utilize a simple vehicle simulation model described in the following section.)

(3) Save final values of altitude, velocity, flight path angle, and dynamic pressure as H1, V1, γ1 and Q1.

(4) Perturb the "initial" flight path angle γ_{sim1} by one degree in the direction that will reduce the error between Q1 and the desired terminal value of dynamic pressure $Q_{desired}$, keeping other conditions at A unchanged. Designate the new flight path angle as γ_{sim2}.

(5) Using the new flight path angle with previous initial conditions at A, again simulate zero angle of attack trajectory from A until the propellant is completely expended.

(6) Save final values of altitude, velocity, flight path angle and dynamic pressure as H2, V2, $\gamma 2$ and Q2.

(7) Interpolate/Extrapolate on the flight path angles used at time A to compute a flight path angle γ_{simA} that will yield a zero angle of attack trajectory with a terminal dynamic pressure of $Q_{desired}$:

$$\gamma_{simA} = \gamma_{sim2} + K_Q(\gamma_{sim2} - \gamma_{sim1}) \tag{3.1}$$

where,

$$K_Q = \frac{(Q_{desired} - Q1)}{(Q2 - Q1)} \tag{3.2}$$

(8) Since the results from the prediction are not computed and implemented instantaneously, a correction to γ_{simA}, H_{init} must be computed to account for the change in vehicle state during the delay time from point A to point B. To accomplish this task, assume a flight path angle of γ_{simA} at time A and simulate a zero angle of attack trajectory from time A to time B (end of delay time; i.e., time at which prediction results are to be implemented) to obtain γ_{simB}. Save the values of flight path angle and altitude at B as γ_{simB}, H_B respectively. Definitions of the predictive steering parameters used above are illustrated in Figure 3-2.

(9) In between the update points (B), relationships described subsequently in Section 3.3.3 are used to compute a flight path angle γ_p and a corresponding altitude H_p based on the effects of gravity on a zero angle of attack trajectory. The commanded

flight path angle can be taken as the value of γ_p or it can be computed by compensating γ_p to correct for the difference between the actual altitude and the zero angle of attack trajectory value, H_p. In the latter case it is necessary to compute an altitude compensation gain K_H.
The reciprocal of K_H is the sensitivity of terminal altitude to changes in current flight path angle. The value of K_H can be computed from quantities already determined in the two predictive simulations:

$$K_H = (\gamma_{sim2} - \gamma_{sim1})/(H2 - H1) \tag{3.3}$$

In addition, the results of predictive simulations can be used either to make a one-shot correction of γ_p at point B or to apply a series of equal corrections every steering cycle between the B points. In the latter case it is necessary to compute the quantities $\Delta\gamma_{p_{cor}}$ and $\Delta H_{p_{cor}}$ from γ_{simA} and the values of H_p, γ_p, and the current altitude H at point A.

$$\Delta H_{p_{cor}} = H - H_p \tag{3.4}$$

$$\Delta\gamma_{p_{cor}} = (\gamma_{simA} - \gamma_p)/N_{steer} \tag{3.5}$$

The variables H_p and γ_p are computed as part of the steering computations described in Section 3.3.3. These variables are then updated with $\Delta H_{p_{cor}}$ and $\Delta\gamma_{p_{cor}}$ as described below.

3.3.2 Computations Implemented at Point B

The commanded flight path angle supplied by the predictive simulations is used at point B to reinitialize other steering relationships that are used to compute the commanded flight path angle between update

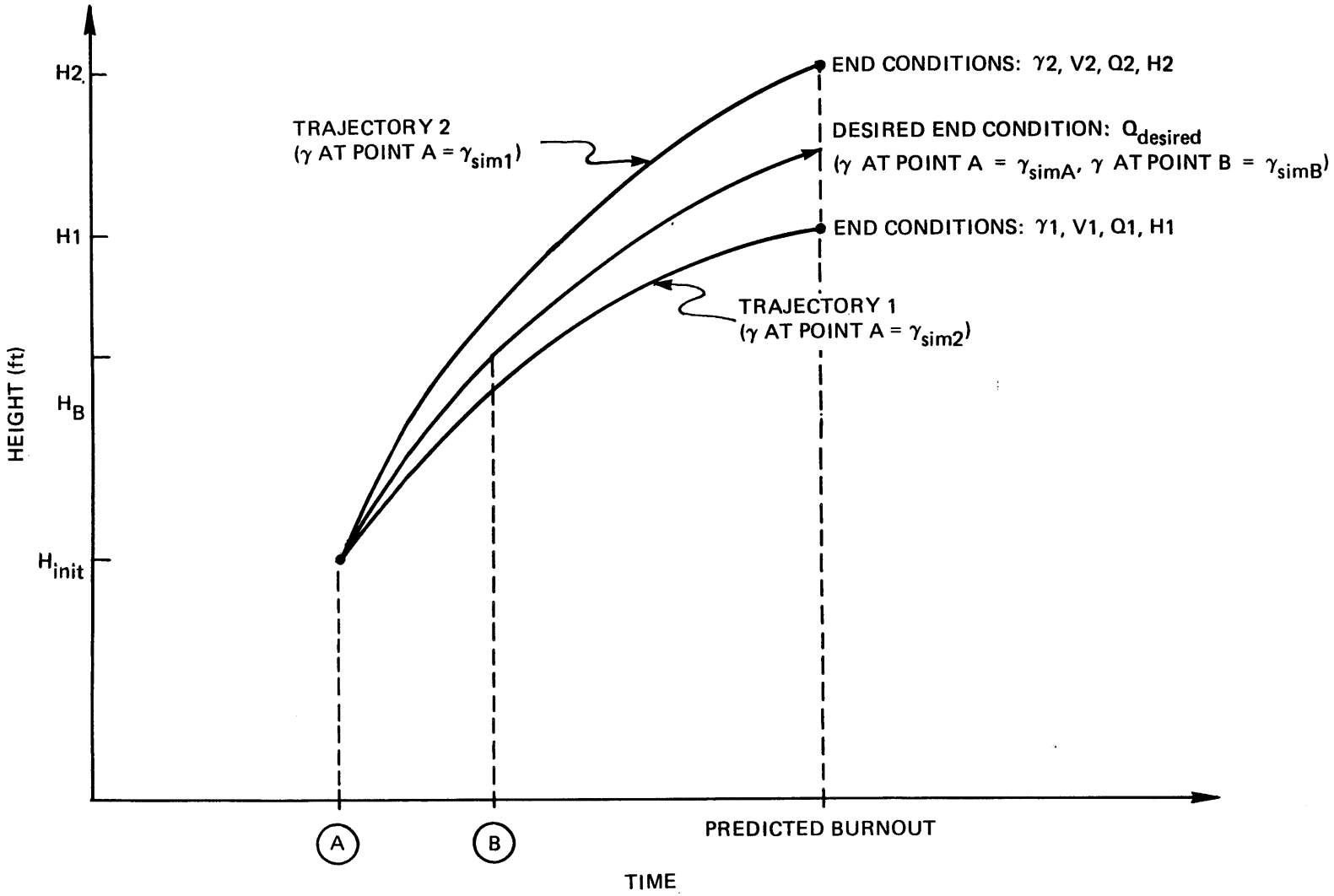

Figure 3-2. Definition of predictive steering parameters.

times. This thesis investigates the options of (1) abruptly introducing the full values of corrections at the points B or (2) parceling out over N_{steer} cycles the change in commanded flight path angle that is otherwise introduced instantaneously in (1).

If the first option is chosen

$$\gamma_p = \gamma_{simB} \tag{3.6}$$

$$H_p = H_B \tag{3.7}$$

If the second option is chosen the quantities $\Delta\gamma_{p_{cor}}$ and $\Delta H_{p_{cor}}$ computed in Eq.s (3.4) and (3.5) are applied to correct γ_p and H_p every steering cycle starting at point B, as described in the next section.

3.3.3 Computations Performed Every Steering Cycle

The following operations are performed every steering cycle regardless of whether there is an update from predictive steering computations.

(1) The values of γ_p, H_p are extrapolated based on the assumption that the vehicle is following a zero angle of attack trajectory.

$$\gamma_p(t_n) = \gamma_p(t_{n-1}) - (g/\bar{V}_n)\cos(\gamma_p(t_{n-1}))\ TIME_{steer} \tag{3.8}$$

$$H_p(t_n) = H_p(t_{n-1}) + \bar{V}_n \sin(\gamma_p(t_{n-1}))\ TIME_{steer} \tag{3.9}$$

where

$\bar{V}_n = (V_n + V_{n-1})/2$ and V_n, V_{n-1} are earth-relative velocity magnitudes obtained from the navigation system.

The above equations were previously derived in Appendix B.

(2) (Optional) If the option of parceling out the corrections in flight path angle every steering cycle is chosen, then γ_p and H_p are updated according to

$$\gamma_p = \gamma_p + \Delta\gamma_{p_{cor}} \tag{3.10}$$

$$H_p = H_p + \Delta H_{p_{cor}} \tag{3.11}$$

(3) (Optional) If the option of compensating steering computations for altitude pertubations from the desired zero angle of attack trajectory is chosen, the ratio K_H computed in step (9) of Section 3.3.1 is implemented to adjust the values of γ_p:

$$\gamma_p = \gamma_p - K_H H_{error} \tag{3.12}$$

where

$$H_{error} = H - H_p$$

Note: The values of altitude H_p is computed only for the purposes of compensating for the deviation of the vehicle from the desired trajectory.

A flowchart of the predictive steering computational procedures is given in Figure 3-3.

3.4 Vehicle Simulation Equations

The mathematical implementation of the simple vehicle model used in the predictive steering concept is described below. Starting with the current values of the earth-relative velocity V, the flight path angle γ, the altitude H, the vehicle mass M, and the engine thrust F at point A, a

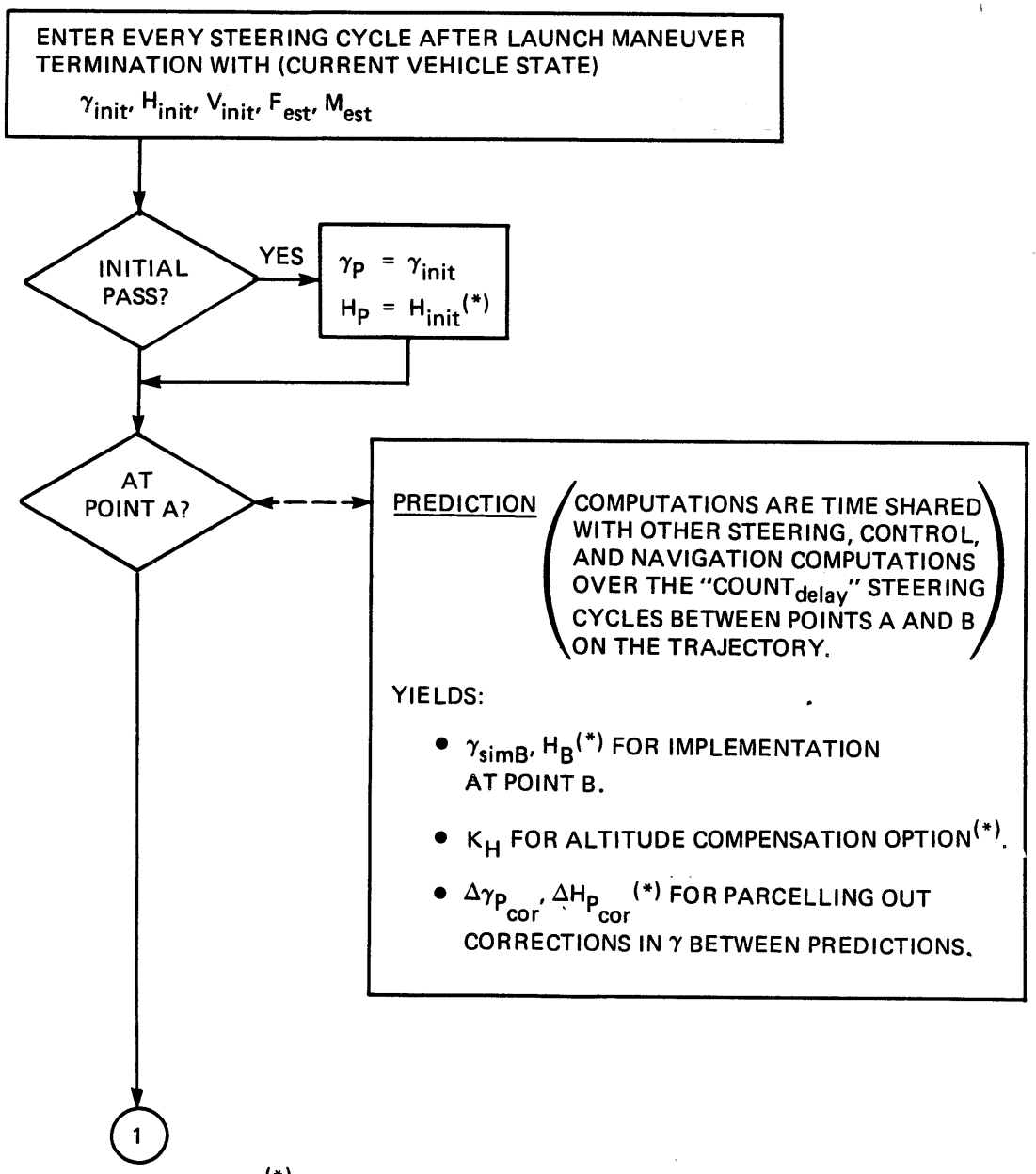

Figure 3-3. Predictive steering flowchart.

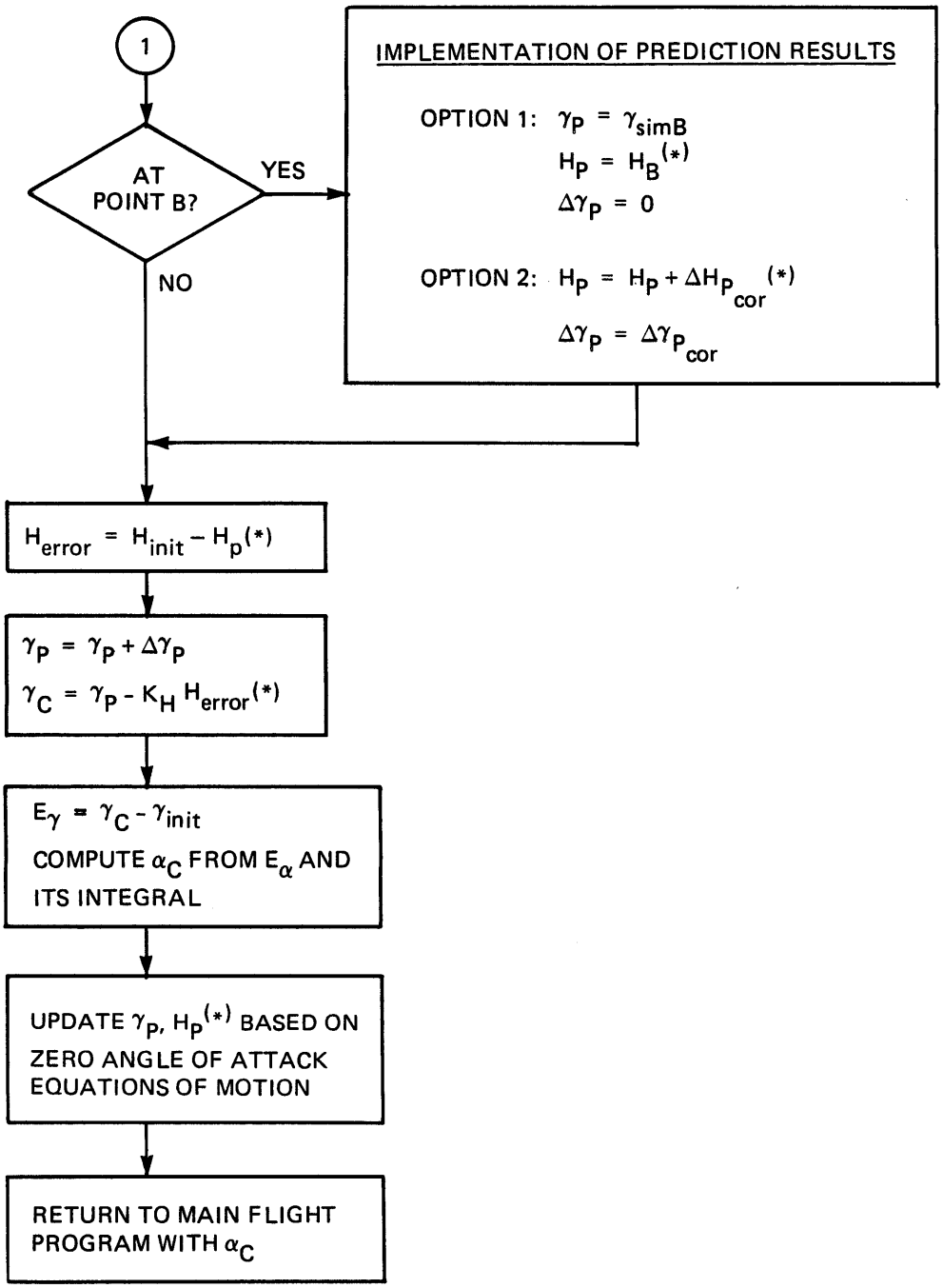

Figure 3-3. Predictive steering flowchart. (Cont.)

zero angle of attack trajectory is simulated to engine burnout by numerically integrating these variables till burnout.

The values of V, γ, and H are obtained by integrating the following zero angle of attack equations derived in Appendix B:

$$\frac{dV}{dt} = \frac{(F - p\,A)}{m} - \frac{S\,q\,C_A}{m} - g \sin \gamma \tag{3.13}$$

where

A = Nozzle cross-sectional area
S = Vehicle cross-sectional area
p = Atmospheric pressure (functionalized vs. H)
m = Vehicle mass
V = Vehicle earth-relative velocity
F = Vacuum thrust
C_A = Axial force coefficent (functionalized vs. V)

$$\frac{d\gamma}{dt} = -(g/V) \cos(\gamma) \tag{3.14}$$

$$\frac{dH}{dt} = V \sin(\gamma) \tag{3.15}$$

The mass parameter employed in Eq. (3.13) is obtained by integrating

$$\frac{dm}{dt} = -\frac{F}{(I_{sp}\,g)} \tag{3.16}$$

The value of thrust required in Eqns. (3.13) and (3.16) is generated by linearly interpolating between points in a thrust vs. time table. The time values for this table are updated as follows each predictive steering cycle from the current estimated thrust and a prelaunch-

stored table of nominal thrust vs. mass. First, the ratio K_B is computed by dividing the current estimated thrust $\hat{F}$ by the value of nominal thrust F_{nom} corresponding to the current estimated mass.

$$K_B = \frac{\hat{F}}{F_{nom}} \tag{3.17}$$

Since the estimated mass does not necessarily correspond to any of the points in the table of nominal thrust vs. mass, it is necessary to employ an interpolation scheme to compute the nominal thrust corresponding to the estimated mass. This interpolation scheme assumes that the thrust varies as a linear function of time between the mass points of the table. This assumption leads to the following interpolation formula for computing F_{nom}:

$$F_{nom} = \{F_{i-1}^2 - g\, I_{sp}\, (m_i - m_{i-1})(F_i - F_{i-1})/(t_i - t_{i-1})\}^{1/2} \tag{3.18}$$

The table of nominal thrust vs. mass is then modifed by multiplying all the thrust values by the factor K_B. These new thrust levels are employed with the tabulated mass values to obtain boost times corresponding to these thrust and mass values, using Eq. (A.7) in Appendix A. The predictive simulation then computes the thrust by interpolating between points in thistable.

The use of different integration methods are evaluated in Chapter 7 where the performances of the predictive steering method alternatives are analyzed. The accuracy and computational requirements of the integration methods are compared.

3.5 Computation of Commanded Angle of Attack and Sideslip Angle

Once the commanded flight path angle is computed each steering cycle the value of estimated flight path angle is subtracted to obtain the flight path angle error E_γ. The commanded angle of attack is then

computed from a linear combination of the error and its integral. This commanded angle of attack is then limited according to a specified maximum product of dynamic pressure times the commanded angle of attack. The expressions for the computation of the commanded angle of attack are as follows:

Error Computation: $$E_\gamma = \gamma_c - \gamma \tag{3.19}$$

Error Integration: $$\gamma_{E_{int}} = \gamma_{E_{int}} + E_\gamma T_S \tag{3.20}$$

where

$$\gamma_{E_{int}} = 0 \text{ initially}$$

Proportional plus integration signal computation:

$$\gamma_{comp} = \gamma_E + K_{int} \gamma_{E_{int}} \tag{3.21}$$

Angle of Attack command computation:

$$\alpha_{p_c} = K'_{st} K_{st} \gamma_{comp} \tag{3.22}$$

Gain factor: K'_{st} = variable gain compensating for vehicle dynamics, which is derived in Appendix D.

K_{st}, K_{int} = steering and integration gains which are selected in Chapter 6.

A block diagram of the steering loop in combination with the control loop is presented in Figure 6-1.

3.6 Launch Maneuver to Steering Transition

An algorithm to smooth the control error during the transition from the launch maneuver to velocity direction steering is desireable since the control system switches from an attitude to angle of attack feedback. This is accomplished by saving the last attitude error at the end of the launch maneuver as E_{bias}, pictured in Figure 3-4a, and using this as an additional input into the angle of attack control loop as shown in Figure 3-4b. The value of E_{bias} is then ramped down to zero during the first second of the steering phase. At the same time the value of the steering constant K_{st}, used to generate the commanded angle of attack, is ramped up to its selected value.

3.7 Flare-in of Steering Commands

The steering commands during both the launch maneuver and subsequent boost phase are computed every 100 ms, or every 10 control cycles of 10 ms duration. Instead of applying these commands abruptly when computed, the changes in these commands are parceled out evenly over the 10 control cycles between the steering updates. This results in a smoother operation of the control systems.

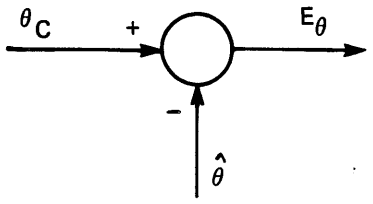

E_θ = LAST VALUE OF ATTITUDE ERROR AT LAUNCH MANEUVER TERMINATION

Figure 3-4a. Attitude feedback junction (excerpt from Figure 2-9).

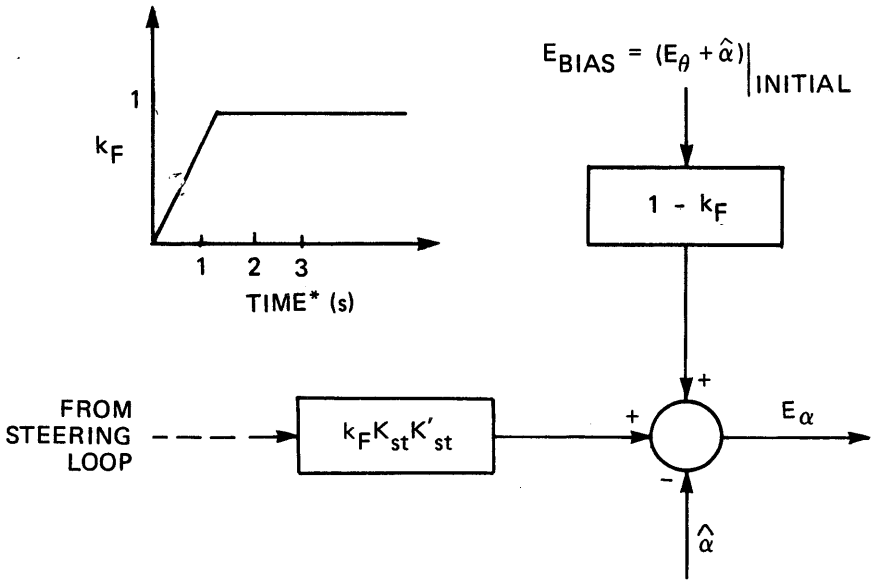

(*)TIME FROM LAUNCH MANEUVER TERMINATION

Figure 3-4b. Angle of attack feedback junction (excerpt from Figure 2-10).

CHAPTER 4

THRUST-MASS ESTIMATION: THEORY AND SIMULATION RESULTS

4.1 Introduction

The main purpose of the thrust-mass estimator is to supply the predictive steering method with estimated values of thrust and mass at discrete intervals. In addition, thrust estimation is used to adjust steering and control parameters during Phase I. Also, if the calibration of the nozzle deflection system is thrust-dependant, this calibration can be corrected through the use of estimated thrust. As described in Chapter 3, the estimated mass is employed to determine the nominal thrust which is divided into the estimated thrust to obtain the factor K_B used in predictive steering simulations. The estimated mass is also used to compute steering and control parameters that are expressed or functionalized in terms of mass. The estimator investigated in this thesis continually estimates thrust and mass over the entire trajectory from vehicle measurements of ΔV corrected for aerodynamic forces, atmospheric effects, and centripetal acceleration effects.

4.2 Mass-Thrust Estimation

4.2.1 Inputs Required for Thrust-Mass Estimator

To derive estimates of thrust and mass the following inputs are necessary from navigation and IMU measurements every steering cycle: the change in sensed velocity along the vehicle longitudinal (x) axis (ΔV_x), the altitude (H_{in}), the accumulated sum of ΔV_x, the inertial velocity

(V_{in}), the angular rotation rate of the vehicle (Ω_{est}), and the distance between the IMU and the center of gravity (L_{imu}). The IMU accelerometers generate a signal that represents the integral of sensed acceleration (not including gravity). The x-component of this sensed velocity is differenced every control cycle (.01s), and the differences are then summed over each steering cycle to produce the quantity ΔV_x required by the thrust-mass estimator. Both the altitude and earth-relative velocity are determined from the vehicle's navigation system. Ω_{est} and L_{imu} are used to compute the centripetal acceleration of the IMU about the CG point. Ω_{est} is the output of the rate estimator which uses a combination of nozzle angle, IMU-measured change in velocity, and change in attitude to arrive at its estimate. L_{imu}, which is dependent on CG location, is functionalized in terms of mass.

The specific impulse is assumed to be temperature independent (constant), and the thrust estimate is initialized at zero just prior to ignition.

4.2.2 Derivation of Thrust-Mass Estimates

The values of estimated vacuum thrust and mass are derived from the estimated total acceleration of the vehicle. The acceleration due to vacuum thrust is measured over a steering cycle as the rate of change in sensed velocity corrected for decelerations due to aerodynamic drag, atmospheric effects over the nozzle, and centripetal acceleration of the IMU about the center of gravity. Specifically,

$$A_{thrust} = (\Delta V_x / T_S) + (A_{aero} + A_{atmo} + A_{cent}) \qquad (4.1)$$

where

A_{thrust} = Axial acceleration due to vacuum thrust

A_{aero} = Axial deceleration due to aerodynamic forces

A_{atmo} = Deceleration compensation for effects of atmospheric pressure on thrust

A_{cent} = Centripetal deceleration at IMU

The deceleration due to axial aerodynamic effects is determined by

$$A_{aero} = S\ q\ CA_{est}/M_{est} \tag{4.2}$$

Substituting the expression for q,

$$A_{aero} = S\ ((1/2)\ \rho_{est}\ V_{in}^2)\ CA_{est}/M_{est} \tag{4.3}$$

where

S = Reference cross sectional area of vehicle

ρ_{est} = Functionalized air density, f(altitude).

CA_{est} = Linearly functionalized axial force coefficient, f(sensed velocity).

M_{est} = Estimated value of mass.

The air density required for Eq. (4.3) is estimated by a simple exponential function of the form

$$\rho_{est}(\text{slugs/ft}^3) = \rho_0\ e^{-h/h_s} \tag{4.4}$$

where

h = Current altitude (ft)

h_s = Functionalized scale height (ft)

ρ_0 = Air density at sea level (slug/ft^3)

The axial force coefficient for Eq. (4.3) is functionalized in terms of sensed velocity and is approximated by 4 straight line segments fitted to data from a nominal-thrust, no-wind reference run. (See Figure 4-1.) The first segment is the least accurate fit of the four lines. However, accuracy is not critical during this interval since values of q are low, and therefore A_{aero} does not contribute significantly to the

total acceleration (Eq. 4.1) . Although the axial coefficient is actually a function of Mach number, it is approximately represented as a function of sensed velocity to simplify the computer implementation.

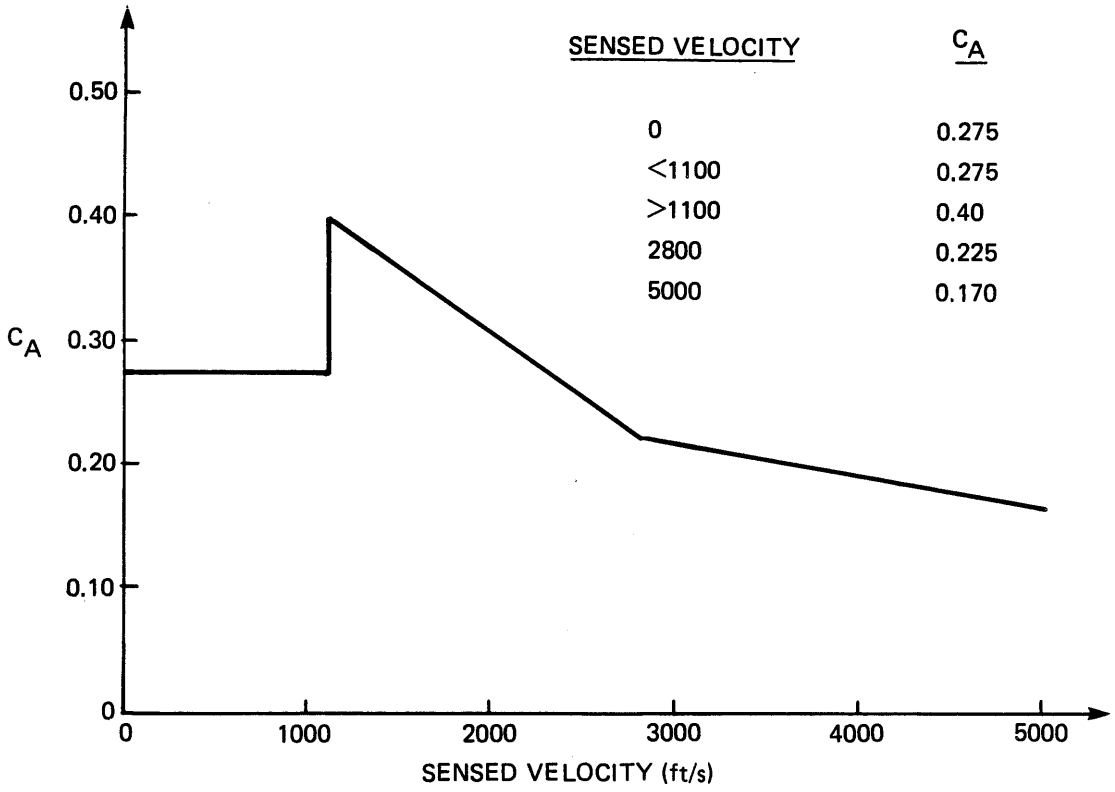

Figure 4-1. Functionalization of axial force coefficient (C_A) vs sensed velocity.

The atmospheric decleration due to the atmospheric pressure over the nozzle area is approximated by the exponential relationship

$$A_{atmo} = A_{nozzle} P_0 e^{-h/h'_s} / M_{est} \qquad (4.5)$$

where

A_{nozzle} = Nozzle area, ft^2

P_0 = Atmospheric pressure at sea level, lb/ft

h'_s = Single value of scale height giving exact atmospheric pressure at 30 kft.

The curve is fitted so that the atmospheric pressure is exact at 30kft which is in the vicinity of maximum dynamic pressure. The errors in thrust due to this approximation are given in Table 4-1.

Table 4-1. Errors in exponential approximations of atmospheric pressure reduction of thrust.

ALTITUDE	0	10K	20K	30K	50K	80K
PERCENTAGE THRUST ERROR*	0	0.23	0.16	0	0.19	0.13

*CONSTANT-THRUST PROFILE

The deceleration due to centripetal acceleration of the IMU about the center of gravity is computed as follows from estimated angular rates:

$$A_{cent} = L_{imu} \left(\Omega^2_{est_k} + \Omega^2_{est_k}\ \Omega^2_{est_{k-1}} + \Omega^2_{est_{k-1}}\right)/3 \qquad (4.6)$$

where

Ω_{est_k} = rate estimates obtained from current steering cycle

$\Omega_{est_{k-1}}$ = rate estimates obtained from previous steering cycle

ℓ_{imu} = distance from center of gravity to the IMU location which is derived from center of gravity estimates.

Eq. (4.6) is derived in Appendix C. Figure 4-2 illustrates the vehicle geometry involved in defining this deceleration component.

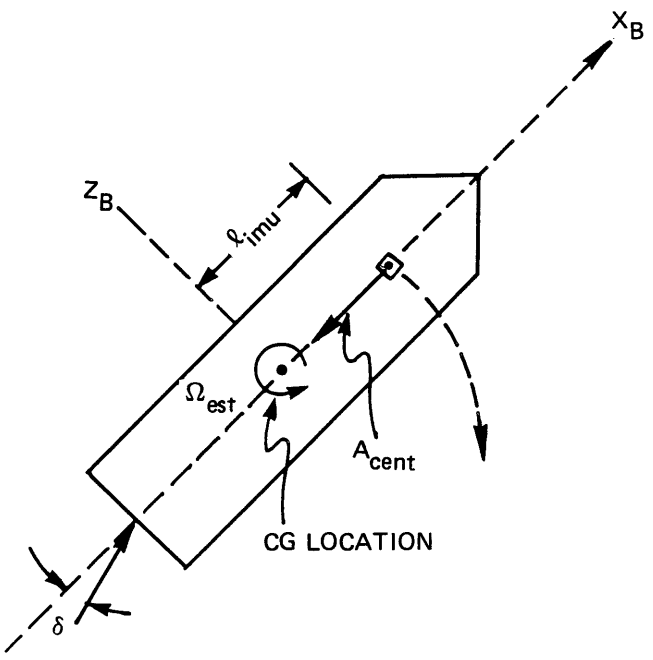

NOTE: Ω_{est} IS THE VEHICLE ROTATION ABOUT THE Y_B AXIS

Figure 4-2. Vehicle centripetal acceleration geometry in the pitch plane.

Once the total acceleration is computed the total mass expended over the steering cycle can be estimated by

$$\Delta M \simeq \dot{m} T_S \tag{4.7}$$

where m is constant and is defined as

$$\dot{m} \simeq \frac{M_{est_{k-1}} A_{thrust}}{I_{sp} g} \tag{4.8}$$

Substituting Eq. (4.8) into Eq. (4.7) and letting $\Delta M = \Delta M_{est}$,

$$\Delta M_{est} = M_{est_{k-1}} (A_{thrust} T_S)/(I_{sp} g) \tag{4.9}$$

Using Eq. (4.9) the estimated mass can be updated:

$$M_{est_k} = M_{est_{k-1}} - \Delta M_{est} \tag{4.10}$$

The average mass over a steering interval is given by

$$M_{est_{avg}} = M_{est_{k-1}} - (\Delta M_{est} / 2) \tag{4.11}$$

Multiplying this average values by the estimated vacuum thrust acceleration A_{thrust} gives the estimated average vacuum thrust over the steering cycle,

$$F_{est} = A_{thrust} M_{est_{avg}} \tag{4.12}$$

where A_{thrust} and $M_{est_{avg}}$ are obtained from Eq.s (4.1) and (4.11).

These estimated values of thrust and mass are then used for vehicle steering and control purposes. A flow chart summarizing the above operations is given in Figure 4-3.

4.3 Estimator Performance

Simulation runs investigating the performance characteristics of the thrust-mass estimator were made for the following conditions:

(1) Thrust profile
   (a) Constant
   (b) Variable, as described in Figure 2-5.
   (c) Constant thrust gradient, producing a 10% thrust changes over the entire boost phase as described in Figure 2-4.

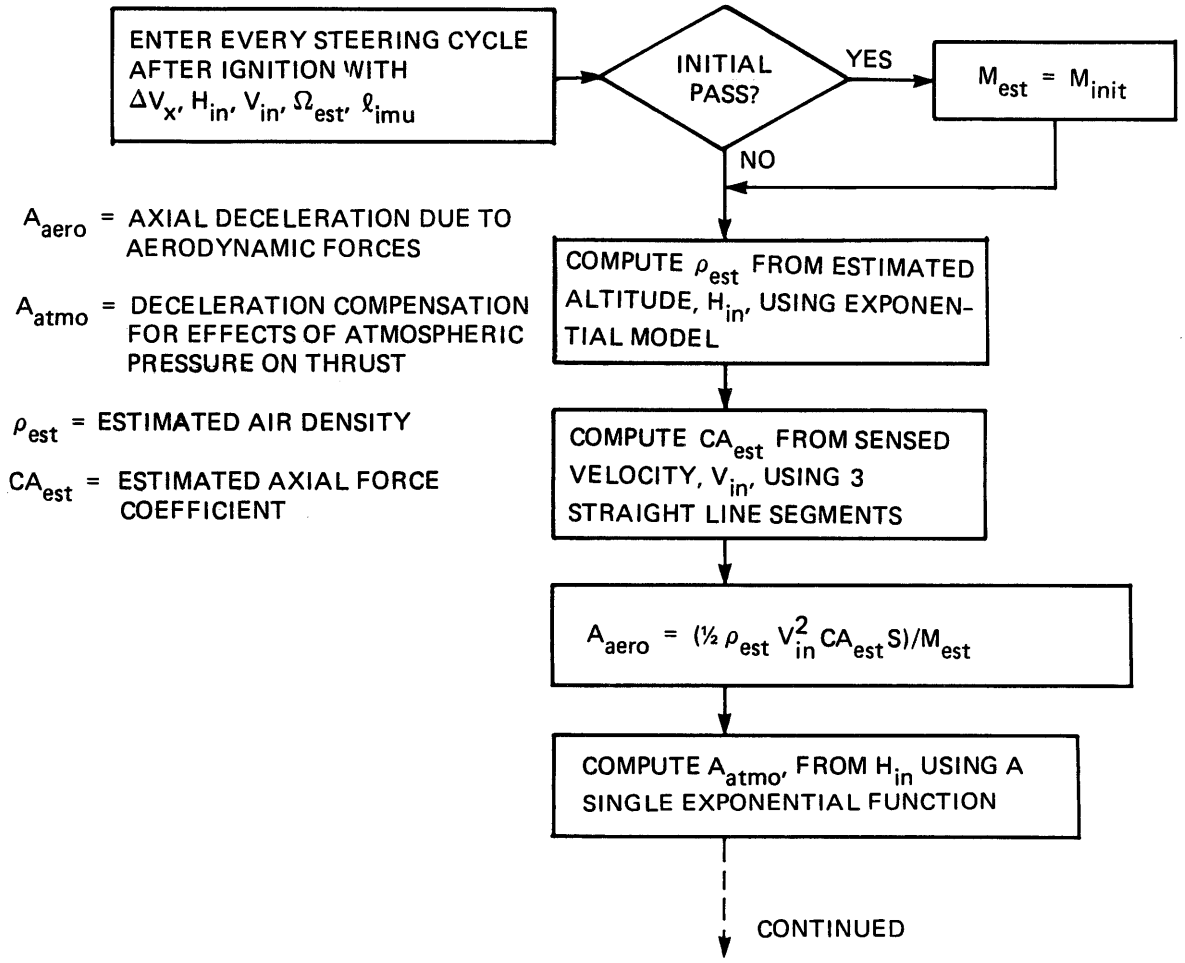

Figure 4-3. Thrust and mass estimator flowchart.

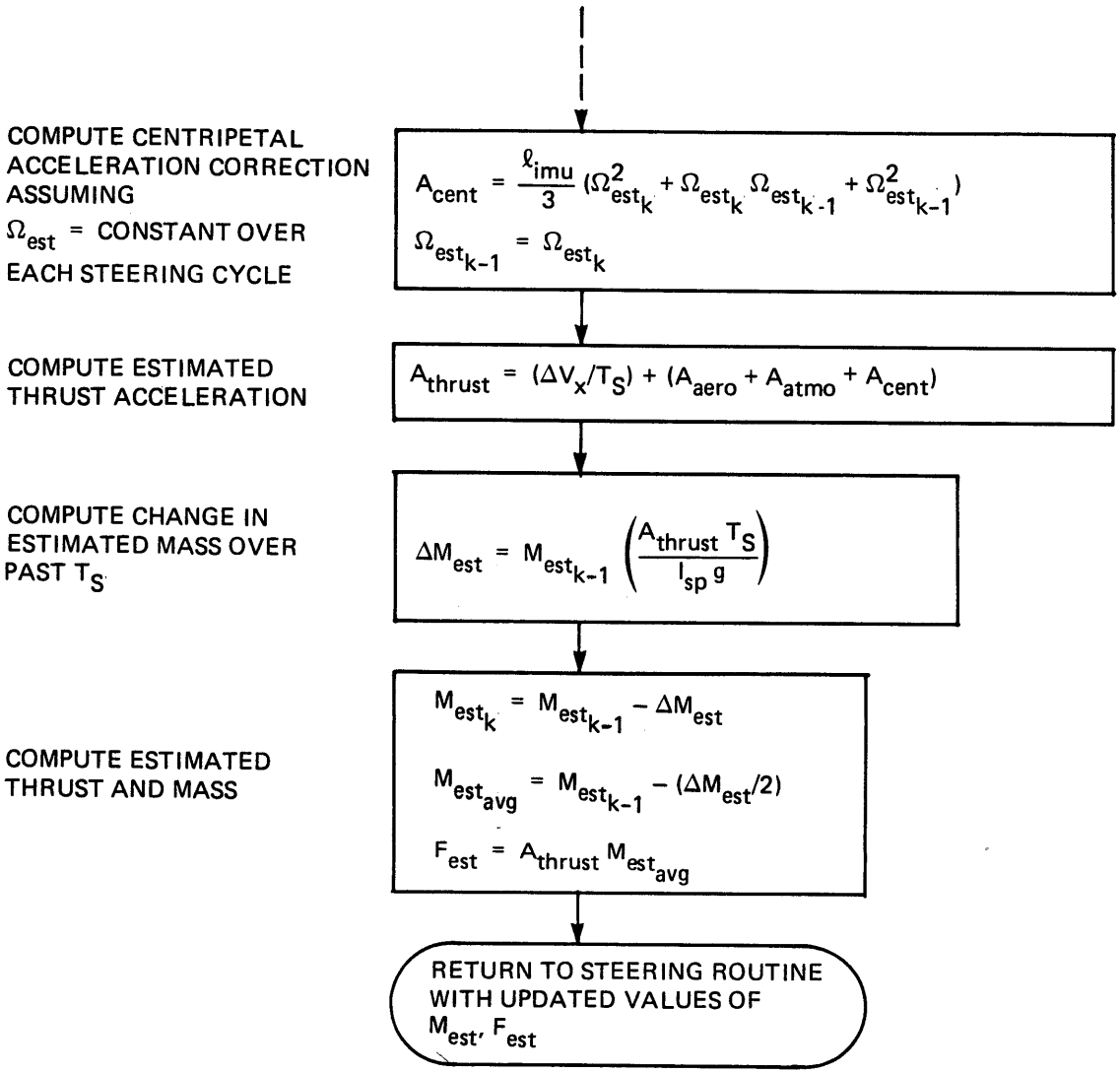

Figure 4-3. Thrust and mass estimator flowchart. (Cont.)

(2) Thrust-mass estimator functionalizations

(a) Functionalizations as described in this chapter

(b) Functionalizations same as (a) except C_A is multiplied by 1.05 to represent a fixed percentage error of 5%. (Since the air mass density ρ multiplies C_A in the computation of the axial aerodynamic force, a 5% error in C_A is equivalent to a 5% error in P.)

(c) Functionalizations same as (a) except P is multiplied by 1.05 to represent a fixed percentage error of 5%.

(3) Winds

(a) No Wind

(b) 99 percentile Head Wind

(c) 99 percentile Tail Wind

(d) 99 percentile Cross Wind

Various combinations of the above conditions were employed in eleven simulation runs. The conditions of these runs and their thrust and mass estimation performance are summarized in Table 4-2. Plots of percentage errors in estimated vacuum thrust, in estimated atmospheric thrust and in estimated mass for the runs of Table 4-2 are presented in Figures 4-4 to 4-14.

4.4 Discussion of Results

The maximum percentage error in estimated vacuum thrust and estimated mass for $t > 16$ seconds are tabulated along with the values of these percentage errors at 39 seconds (near the end of the boost phase) in Table 4-2. By considering the maximum estimation errors for $t > 16$ seconds, this table ignores the errors in the launch maneuver prior to the takeover of predictive steering. The table also ignores the large but short excursion in estimated thrust that occurs as the result of C_A approximation as the Mach number passes through unity for t between 12 and 16 seconds. This thrust error excursion ranges from roughly 1.2% to

1.6% in all cases as seen in the plots presented in Figures 4-4 to 4-14. These plots show that the brief thrust error excursion does not appreciably affect the estimated mass error in any of the cases. The following performance features are indicated by Table 4-2:

Table 4-2. Thrust-mass estimation errors.

Run #	Steering Method	Winds	Flight Conditions (90° Launch)	Maximum Percentage Estimation Errors and (Time of Occurrence)		Percentage Estimation Errors at T = 39 s	
				Vac. Thrust	Mass	Vac. Thrust	Mass
1	Predictive	No		-0.41 (16.80)	0.035 (23.09)	0.091	-0.027
2		No	5% error in CA	0.55 (26.39)	-0.23 (39.00)	0.13	-0.23
3		No	5% error in P	-0.39 (30.39)	-0.23 (39.00)	-0.041	-0.23
4		Tail		0.57 (26.99)	-0.17 (39.00)	-0.016	-0.17
5		Head		-0.65 (27.89)	-.18 (33.00)	0.23	0.14
6		XWind		-0.43 (17.09)	0.052 (32.39)	0.091	-0.0021
7		No	10% gradient	-0.44 (16.79)	0.034 (31.29)	-0.14	-0.027
8		Head	10% gradient	-0.73 (27.39)	0.17 (31.89)	0.011	0.13
9		No	Variable profile	-0.40 (16.79)	0.034 (22.99)	0.096	-0.032
10	Logarithmic	No		-0.44 (16.79)	0.032 (23.09)	0.091	-0.031
11		Head		-0.64 (18.49)	0.18 (32.99)	0.26	0.14

(1) The percentage errors are essentially identical for the no wind and head wind cases simulated with the predictive and logarithmic steering methods. Therefore, for at least these two cases investigated the performance of the thrust, mass estimator is not significantly affected by the choice of steering (and the resulting differences in response).

(2) The primary effect of wind on the thrust-mass estimator is to cause the true dynamic pressure based on the air relative velocity to differ from the estimated dynamic pressure which is based on the earth relative velocity. This difference in turn results in an error in the estimated axial aerodynamic

force that is used in estimating thrust. In the case of the cross wind the estimator errors are essentially the same as in the no wind case, because the cross wind has negligible effect on the dynamic pressure. The head and tail winds, however, increase the maximum thrust error from the 0.41% no wind magnitude to magnitudes of 0.65% and 0.57% respectively.

(3) In the no wind, variable-thrust profile case, thrust fluctuations do not change the estimation errors appreciably from the values given for the no wind, constant-thrust case. Also, the no wind, 10% thrust gradient case gives about the same estimation errors. Only the combination of a head wind and the 10% thrust gradient produces an appreciable change in maximum thrust estimation error from 0.41% for the no wind, constant-thrust case to 0.73% and a corresponding change in maximum estimated mass error from 0.035% to 0.17%.

(4) When 5% errors were introduced in C_A and P in two separate simulation runs, both runs yielded the maximum error in estimated mass of 0.23% for all cases studied. This error is not negligible nor is the maximum thrust error of 0.55% obtained for these two cases. However, it is pointed out in Section 7.8, that the terminal dynamic pressure errors for these two cases are within acceptable bounds.

(5) The maximum error in estimated thrust and estimated mass for all the cases studied are 0.73% and 0.23%, respectively. The significance of these errors is dependent on the magnitude of the off-nominal conditions to which the predictive steering is adapting. These errors should have little effect, for example, on the predictive steering system's ability to adapt to a 10% off-nominal gradient in thrust.

Simulations of the predictive steering system's performance for various conditions in Chapter 7 reveal that although small errors in the estimated vacuum thrust will not appreciably affect the terminal dynamic pressure, they can cause significant excursions in $q\alpha$. The simulation results show that these $q\alpha$ excursion can result from either constant or fluctuating errors in estimated thrust. Simulation plots in Figures 4-4 to 4-14, which show how the errors in estimated thrust and estimated mass can vary with time, may be useful for comparison with plots of $q\alpha$ vs time for the same cases in Chapter 7. Although the vacuum thrust, not the atmospheric thrust is provided as an input to predictive steering, these plots include the estimated atmospheric thrust as well, for comparison.

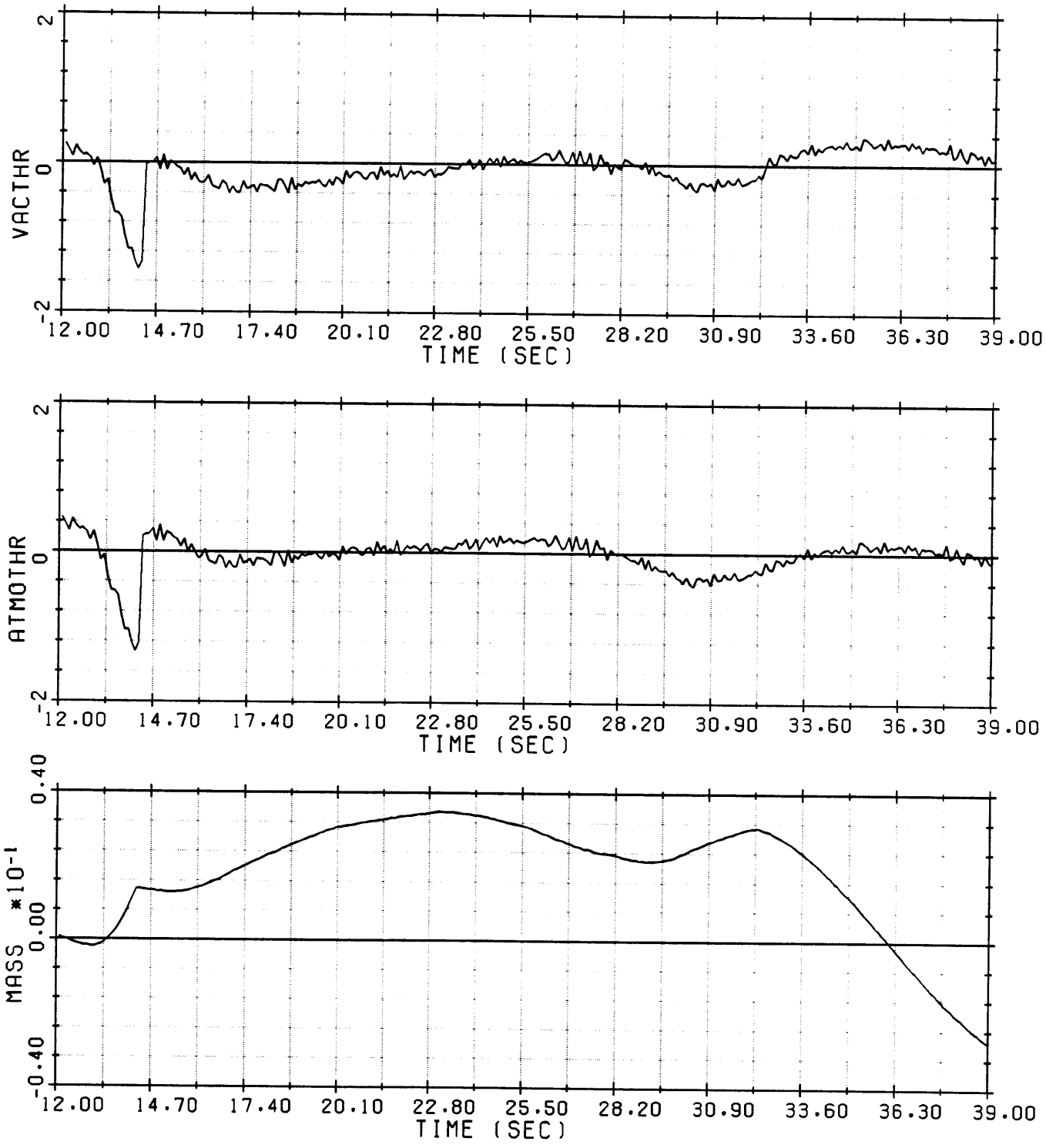

Figure 4-4. Simulation Run #1.

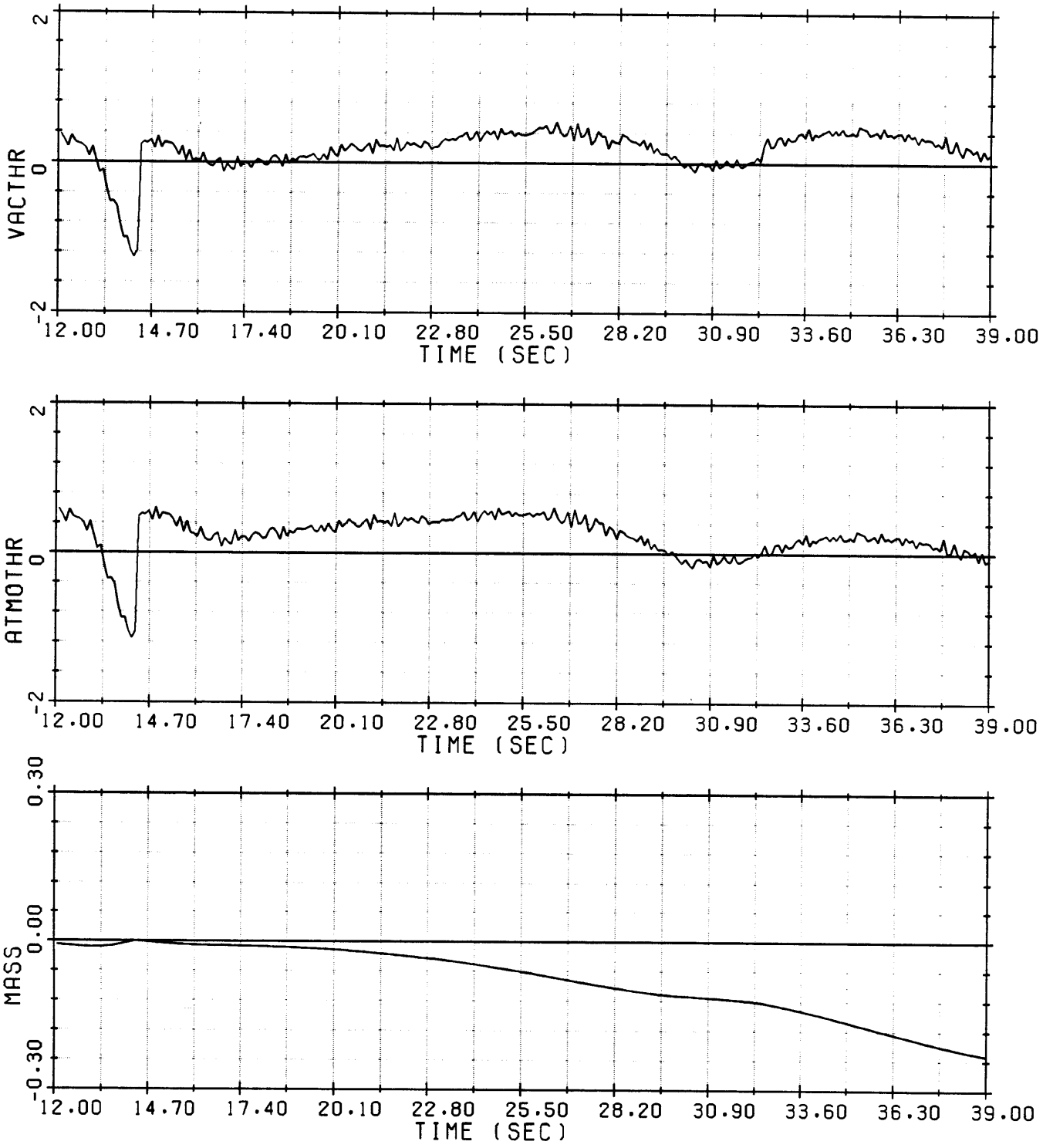

Figure 4-5. Simulation Run #2.

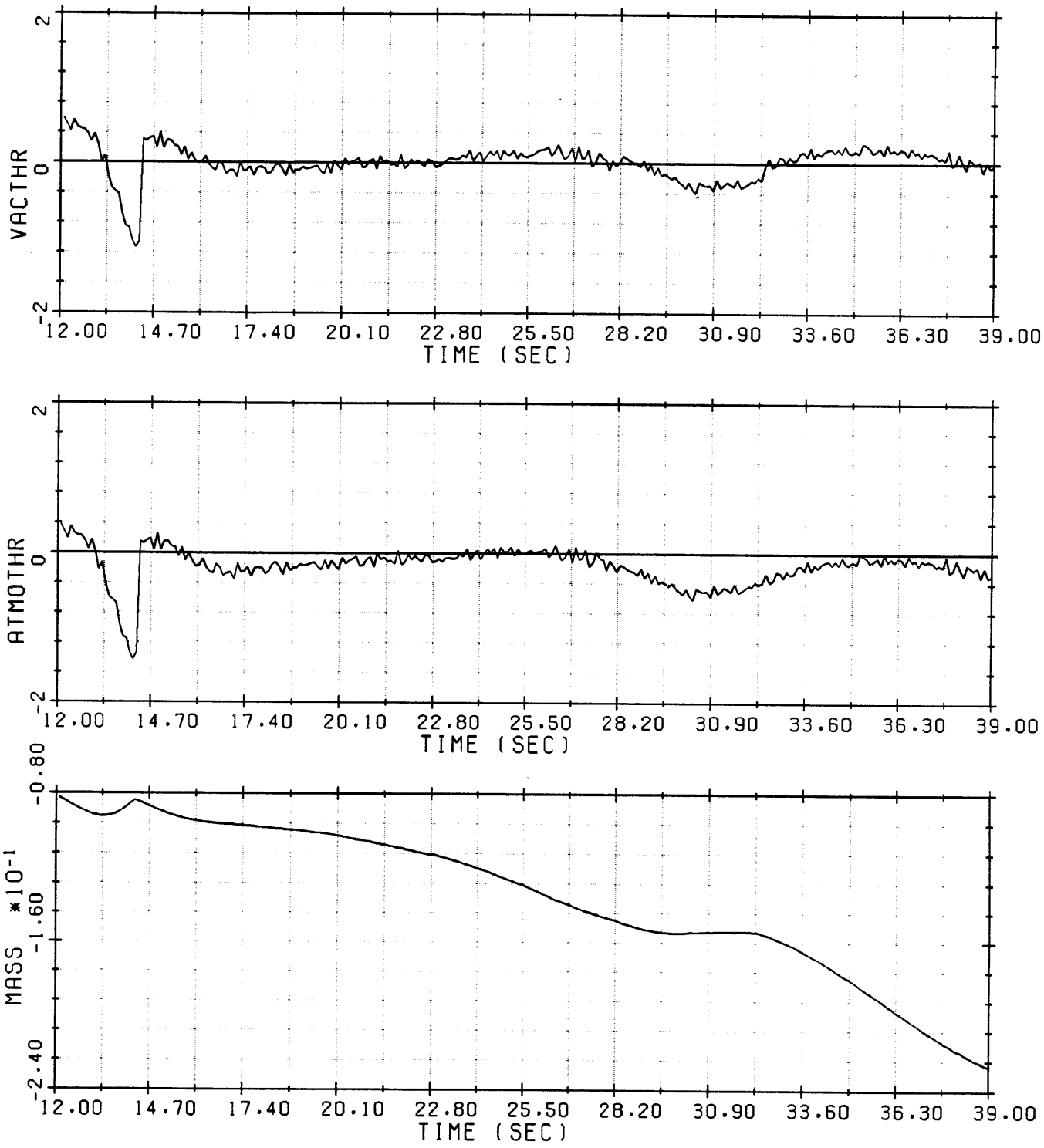

Figure 4-6. Simulation Run #3.

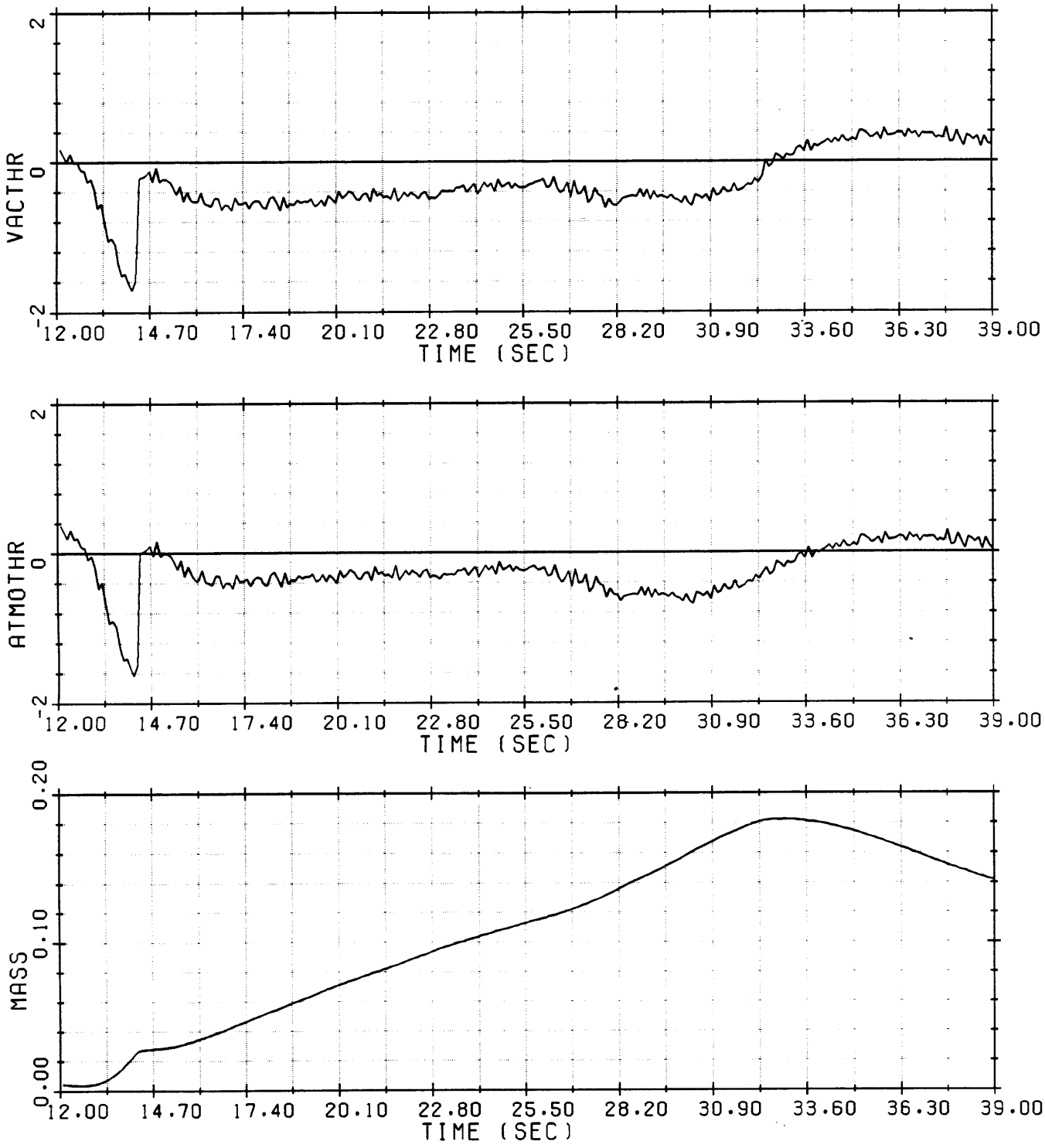

Figure 4-7. Simulation Run #4.

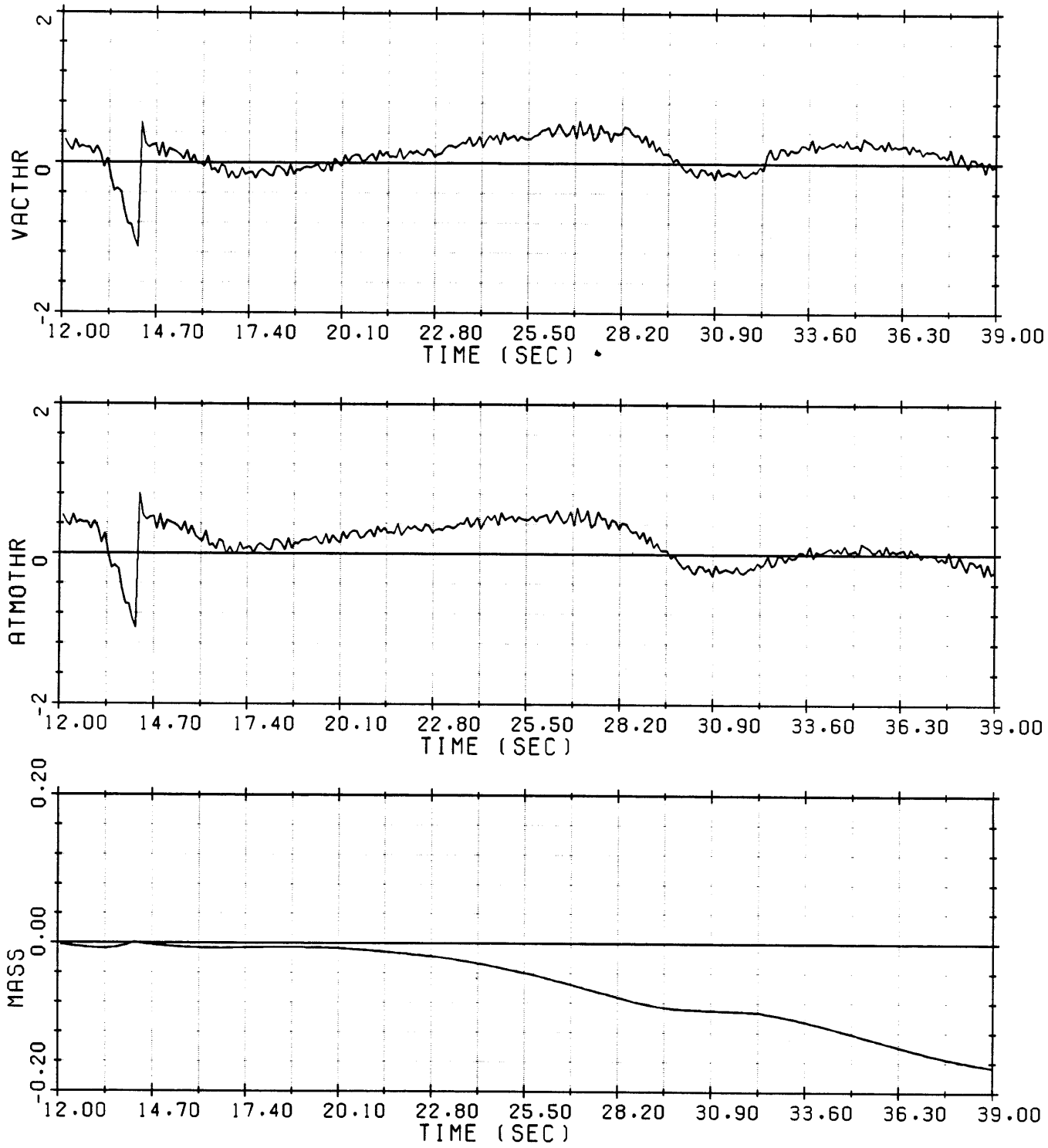

Figure 4-8. Simulation Run #5.

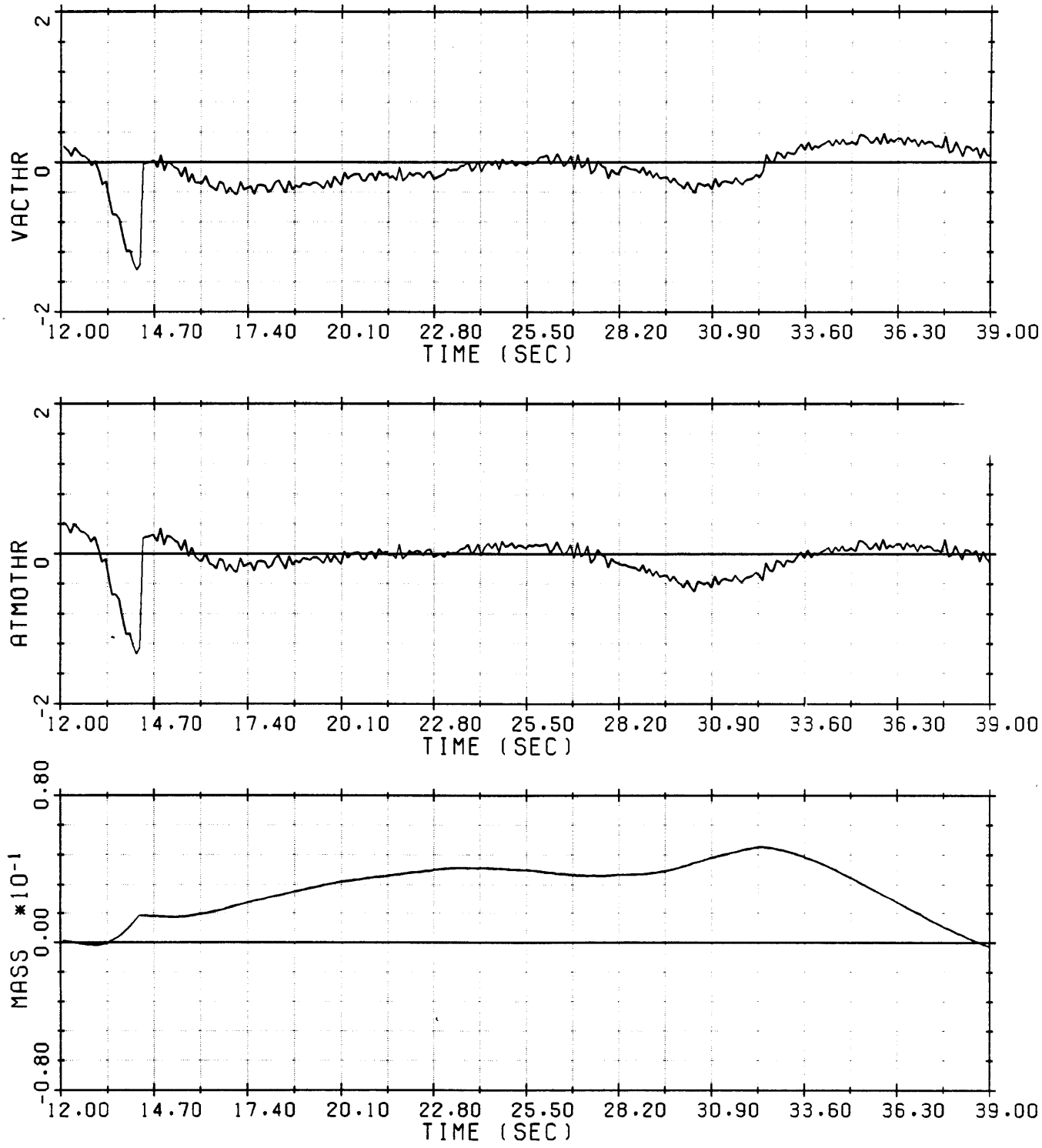

Figure 4-9. Simulation Run #6.

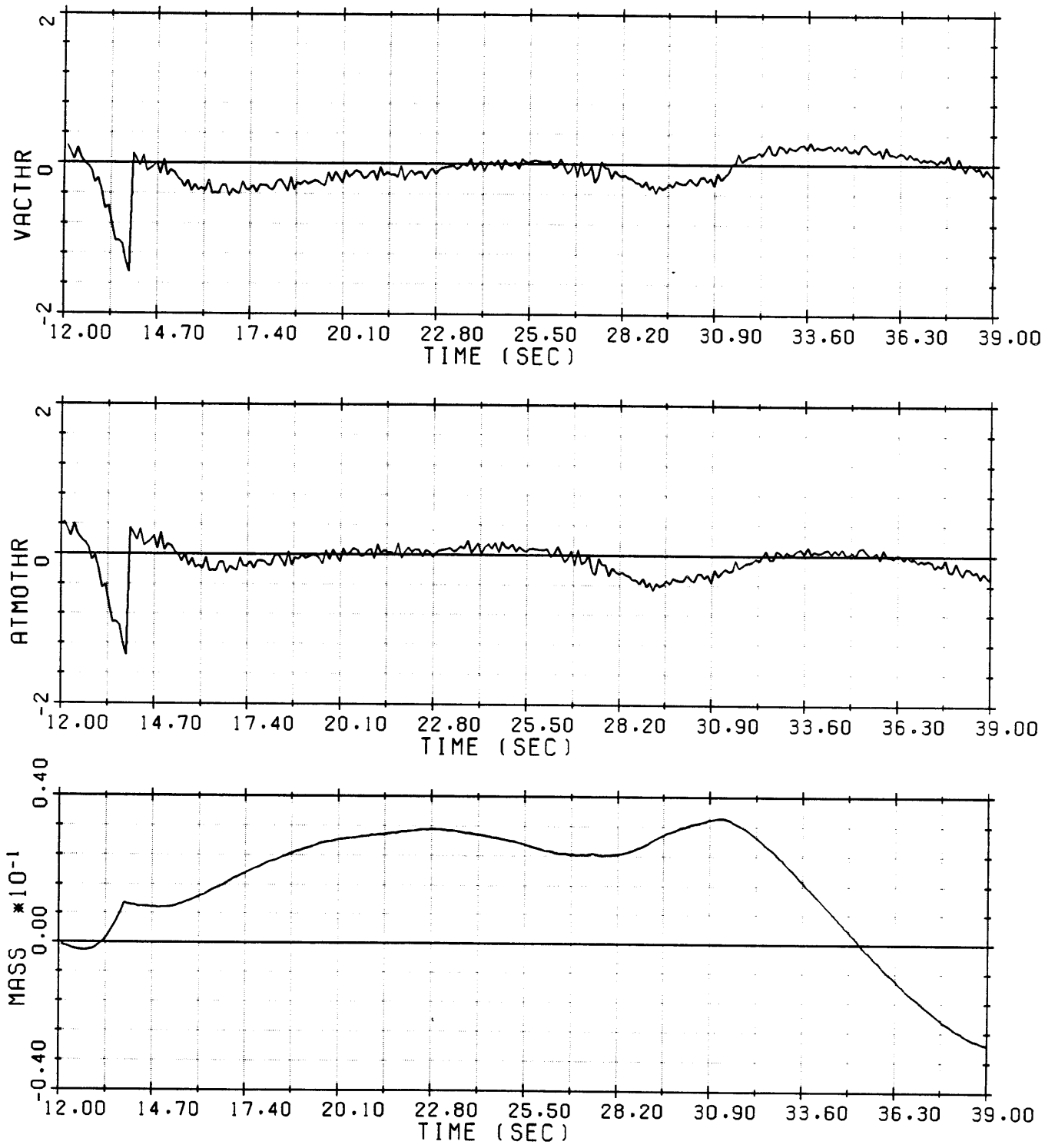

Figure 4-10. Simulation Run #7.

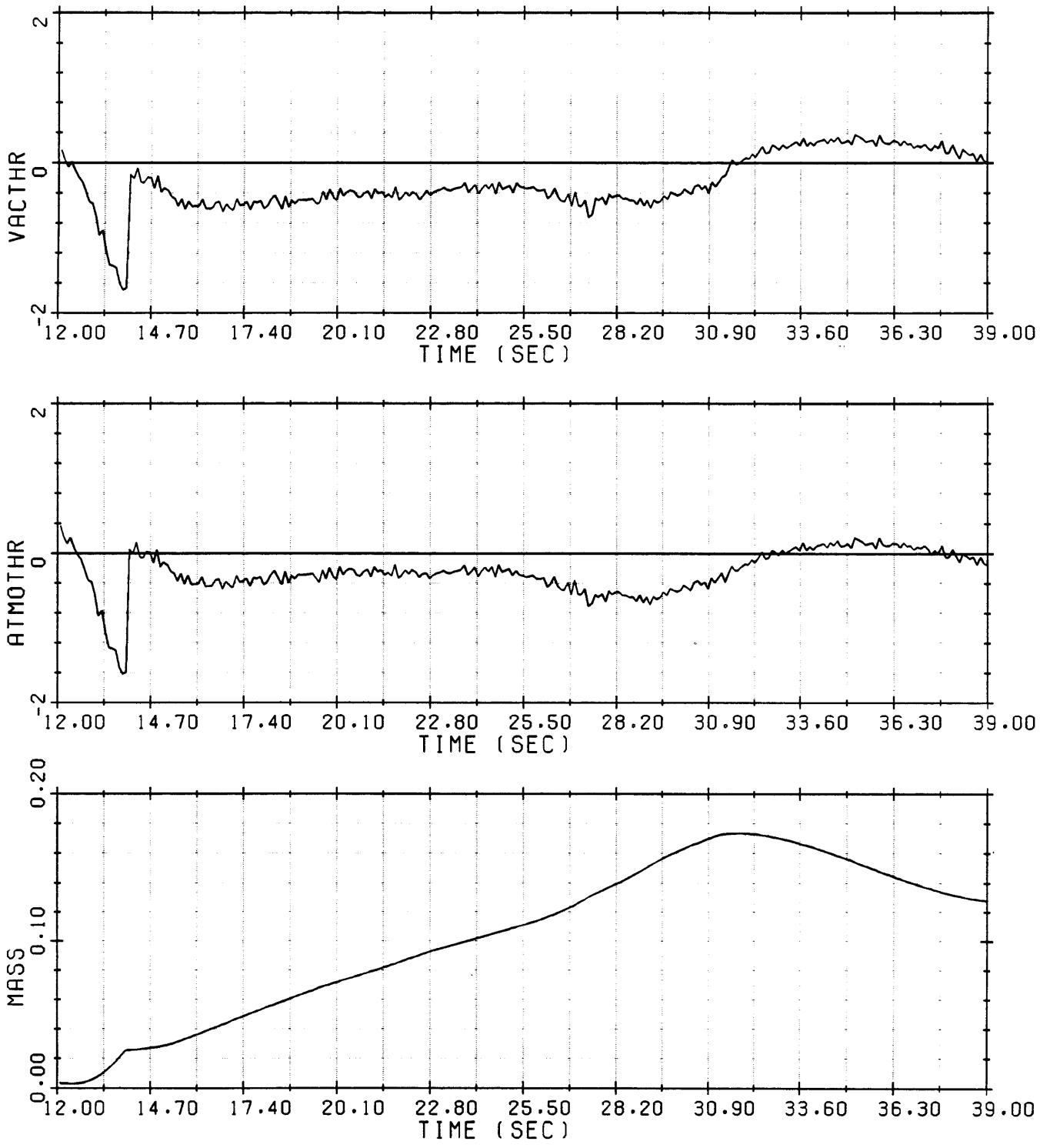

Figure 4-11. Simulation Run #8.

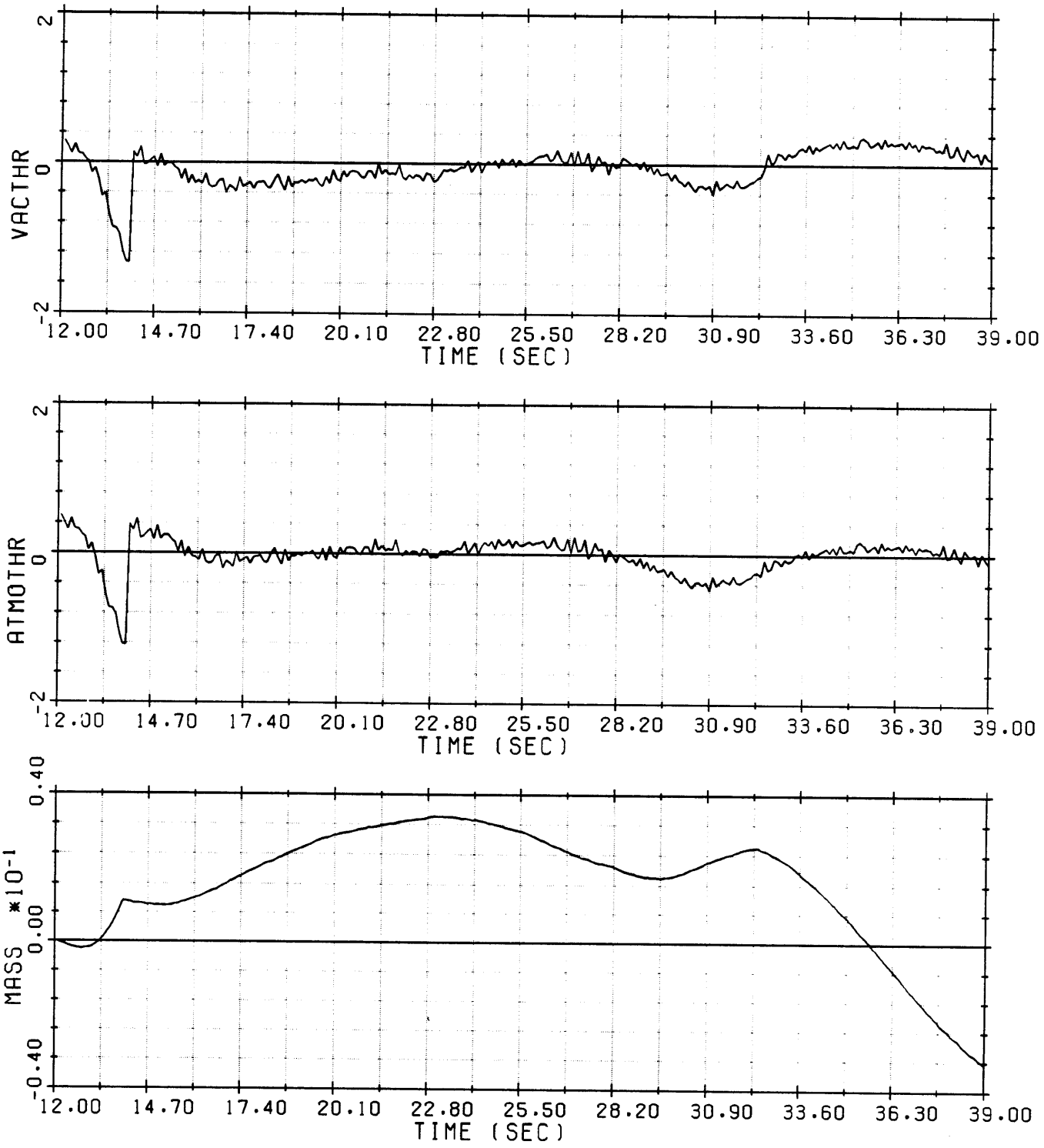

Figure 4-12. Simulation Run #9.

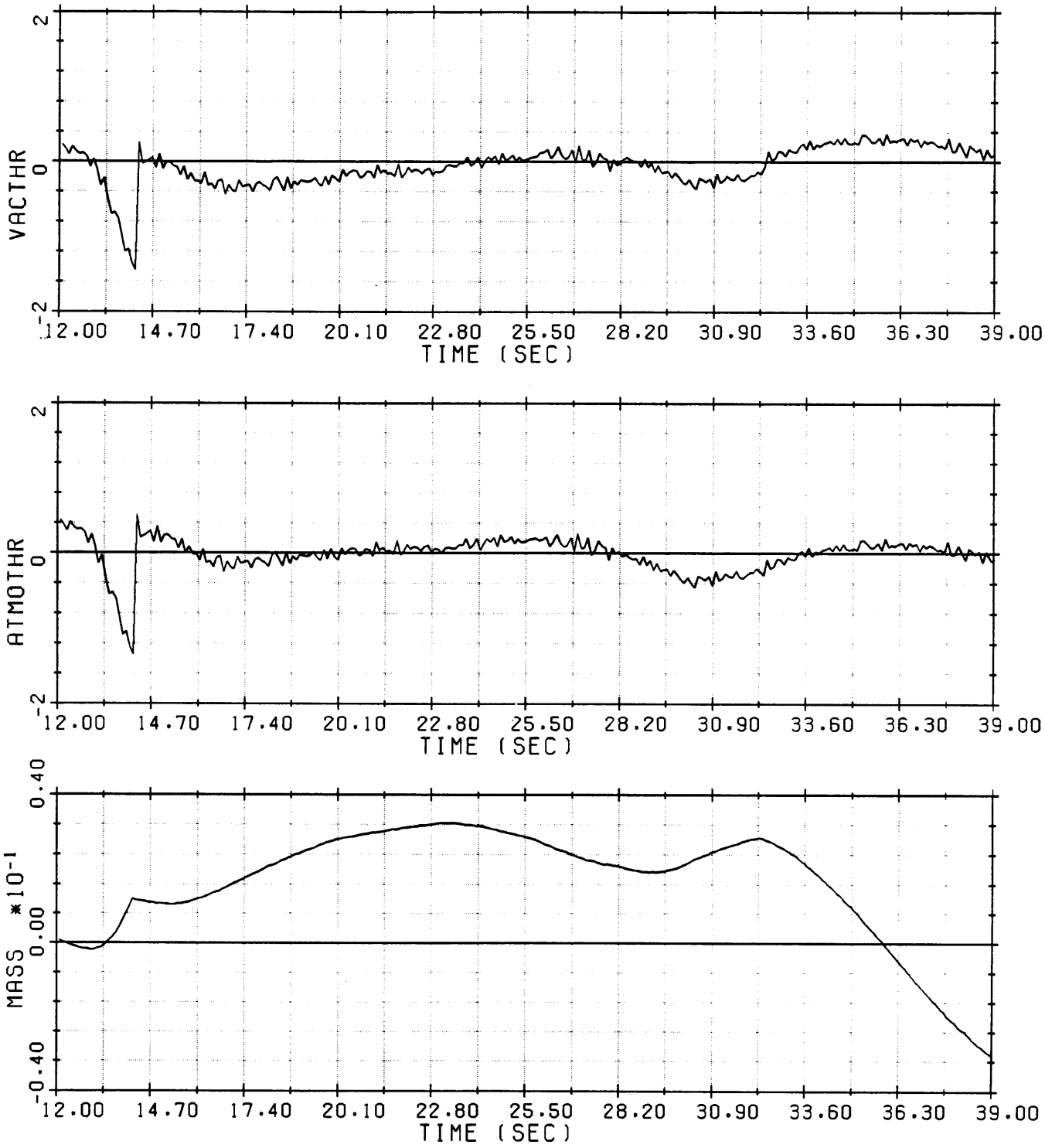

Figure 4-13. Simulation Run #10.

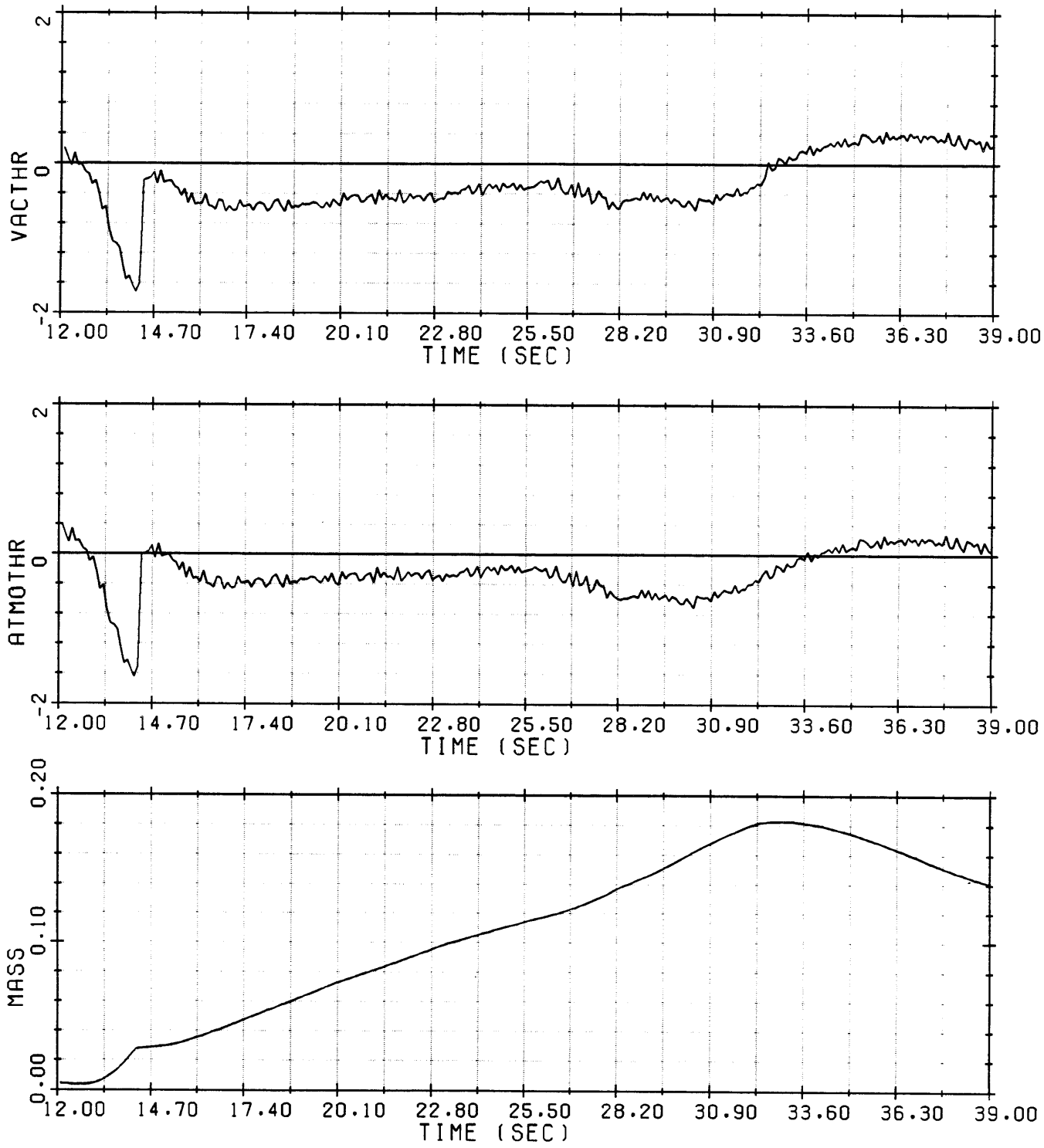

Figure 4-14. Simulation Run #11.

CHAPTER 5

SELECTION OF A FIXED FUNCTIONALIZED STEERING METHOD: THEORY AND SIMULATION RESULTS

5.1 Introduction

The purpose of this chapter is to evaluate two fixed functionalized velocity direction steering methods, an exponential and a logarithmic method, and select one method for use in comparisons with the predictive steering concept. A fixed functionalized velocity direction steering method is one in which the vehicle flight path angle, γ, is commanded to follow a pre-determined flight path angle curve is expressed as a function of time (or velocity). For this study, the curve is fitted to an ideal zero angle of attack reference trajectory beginning at the point at which the launch maneuver ends. The advantage of these steering methods is that they are simple and require few inflight computations. However, if a wide variety of mission objectives, vehicle payloads, and launch conditions must be accommodated, the use of such a prelaunch functionalization can require extensive prelaunch computations to determine and functionalize the desired trajectory and/or extensive inflight memory capabilities to store all alternative trajectory functionalizations. The functionalization is complicated even further if an attempt is made to accommodate unanticipated flight conditions by representing a family of trajectories that covers all possible variations of flight conditions. The variations in flight conditions could be in the form of unexpected winds and unexpected thrust variations due to temperature gradients.

5.2 Exponential Steering Basic Relationship

It should be noted that the problems encountered in functionalizing a zero angle of attack trajectory of a symmetrical launch vehicle are essentially the same for flight path angle steering as for the commonly used net acceleration vector steering, since the velocity and acceleration direction are nearly the same on a zero angle of attack trajectory of a symmetrical vehicle.

The behavior of the flight path angle along a zero angle of attack trajectory can be well approximated by an exponential function of time. This function is presently used in net acceleration direction steering and is equally suited to the flight path angle steering approach of this thesis.

The exponential functionalization of commanded flight path angle versus time is

$$\gamma_c = \gamma_{cmdf} + (\gamma_{c_{kick}} - \gamma_{cmdf})\, e^{-k_s(t - t_{kick})} \qquad (5.1)$$

where

γ_c = Commanded flight path angle at time t from launch

γ_{cmdf} = Final commanded flight path angle (constant)

$\gamma_{c_{kick}}$ = Commanded launch angle (constant)

k_s = Exponential constant

t_{kick} = Launch maneuver duration (constant)

t = Time from launch

To demonstrate that an exponential functionalization can provide a good approximation of the flight path angle along a zero angle of attack trajectory, $\left|\dot{\gamma}\right|$ is plotted on a log scale versus time for this trajectory. From Eq. (5.1) it can be shown that

$$\log_{10}\left|\dot{\gamma}\right| = \log_{10} e \left\{\log_e k_s(\gamma_{c_{kick}} - \gamma_{cmdf}) - k_s(t - t_{kick})\right\} \qquad (5.2)$$

From this relationship, it is seen that if the exponential function is a good approximation, $\log_{10}|\dot{\gamma}|$ versus t must follow a straight line. Figure 5-1 shows that $\log_{10}|\dot{\gamma}|$ versus t, plotted for an idealized zero angle of attack trajectory for three different thrust levels, is indeed closely approximated by a straight line. The following approach to fitting an exponential function to a zero angle of attack profile of flight path angle is based on fitting the $\dot{\gamma}$ of the exponential function to two points on the zero angle of attack trajectory as shown in Figure 5-2.

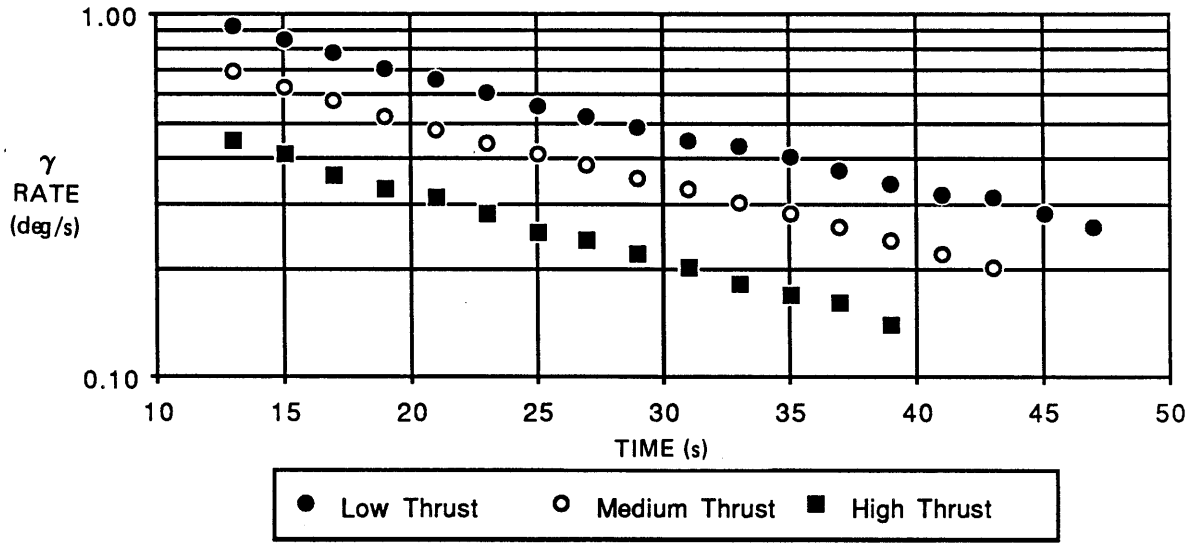

Figure 5-1. Zero angle of attack trajectory γ rate profile.

5.2.1 Prelaunch Computations

The values used to compute the constants in Eq. (5.1) are determined before launch and are obtained from reference runs that follow a zero angle of attack trajectory after the launch maneuver and arrive at the staging dynamic pressure of 1200 psf. The desired end condition is met by adjusting the targeted flight path angle at the end of the launch maneuver through several iterations until the desired end conditions are met.

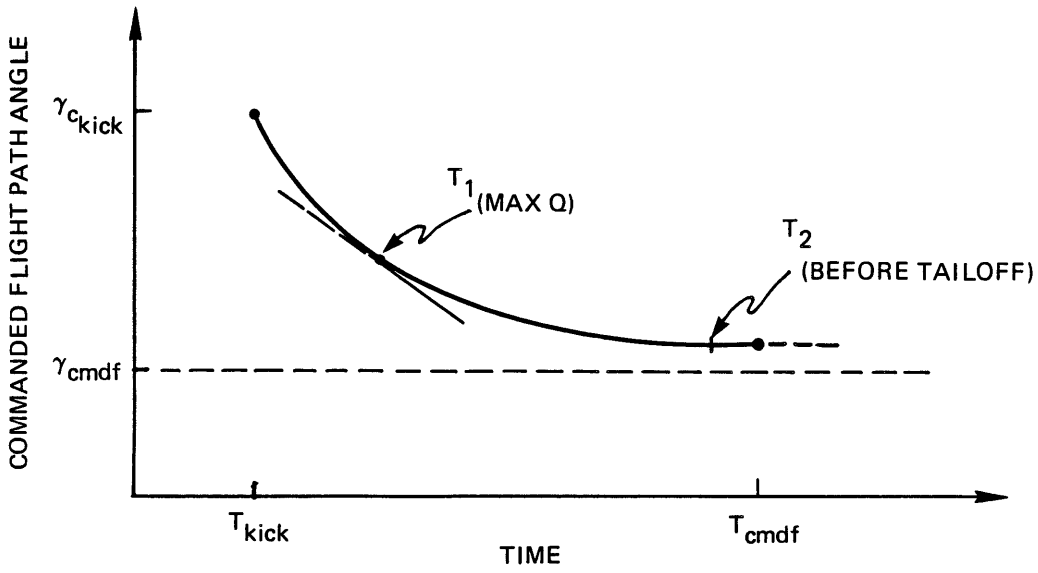

Figure 5-2. Exponential functionalization of the commanded flight path angle.

The exponential constant, k_s, and the final commanded flight path angle, γ_{cmdf}, are computed by fitting the exponential curve to the reference zero angle of attack trajectory at two specified times: t_1 seconds from launch and t_2 seconds from launch. The times selected for the curve fit are the time, t_1, at which maximum dynamic pressure occurs and the time, t_2, immediately preceding tailoff. The solution for k_s and γ_{cmdf} is facilitated by equating the expression for $\dot{\gamma}_c$ obtained by differentiating Eq. (5.1) with the equation for $\dot{\gamma}$ obtained by assuming that $\dot{\gamma}$ is produced by gravity acceleration only. (This is a valid assumption for the zero angle of attack or "gravity turn" trajectory). The equations are written for both t_1 and t_2.

The expressions for $\dot{\gamma}$ at t_1 and t_2 computed from gravity acceleration are the following:

$$\dot{\gamma}_1 = -g \cos \gamma_1 / V_{e_1} \tag{5.3}$$

$$\dot{\gamma}_2 = -g \cos \gamma_2 / V_{e_2} \tag{5.4}$$

where V_{e_1} and V_{e_2} are the respective values of earth relative velocity at t_1 and t_2.

The second set of expressions for γ at t_1 and t_2 obtained by differentiating Eq. (5.1) (and assuming that $\dot{\gamma} = \dot{\gamma}_c$) is as follows:

$$\dot{\gamma}_1 = -k_s(\gamma_{c_{kick}} - \gamma_{cmdf})\, e^{-k_s t_1} \tag{5.5}$$

$$\dot{\gamma}_2 = -k_s(\gamma_{c_{kick}} - \gamma_{cmdf})\, e^{-k_s t_2} \tag{5.6}$$

Equating the two expressions for γ_1 (Eq.'s (5.3) and (5.5)) and the two expressions for γ_2 (Eq.'s (5.4) and (5.6))

$$\dot{\gamma}_1 = \frac{-g \cos \gamma_1}{V_{e_1}} = -k_s(\gamma_{c_{kick}} - \gamma_{cmdf})\, e^{-k_s(t_1 - t_{kick})} \tag{5.7}$$

$$\dot{\gamma}_2 = \frac{-g \cos_2 \gamma_2}{V_{e_2}} = -k_s(\gamma_{c_{kick}} - \gamma_{cmdf})\, e^{-k_s(t_2 - t_{kick})} \tag{5.8}$$

Finally, taking the ratio of Eq.'s (5.7) and (5.8)

$$\frac{\dot{\gamma}_2}{\dot{\gamma}_1} = \frac{-g \cos \gamma_2 / V_{e_2}}{-g \cos \gamma_1 / V_{e_1}} =$$

$$\frac{-k_s(\gamma_{c_{kick}} - \gamma_{cmdf})\, e^{-k_s(t_2 - t_{kick})}}{-k_s(\gamma_{c_{kick}} - \gamma_{cmdf})\, e^{-k_s(t_1 - t_{kick})}} \tag{5.9}$$

Therefore,

$$e^{-k_s(t_2 - t_1)} = \frac{V_{e_1} \cos \gamma_2}{V_{e_2} \cos \gamma_1} \tag{5.10}$$

or

$$e^{k_s(t_2 - t_1)} = \frac{V_{e_2} \cos \gamma_1}{V_{e_1} \cos \gamma_2} \tag{5.11}$$

Solving Eq. (5.11) for k_s,

$$k_s = \frac{1}{(t_2 - t_1)} \log_e \frac{V_{e_2} \cos \gamma_1}{V_{e_1} \cos \gamma_2} \tag{5.12}$$

The expression for γ_{cmdf} can be obtained by solving Eq. (5.7),

$$\gamma_{cmdf} = \gamma_{c_{kick}} - \frac{g \cos \gamma_1}{V_{e_1} k_s} e^{k_s(t_1 - t_{kick})} \tag{5.13}$$

where k_s is the value given by Eq. (5.12)

5.2.2 Postlaunch Computations

γ_c is computed every steering cycle from Eq. (5.1).

5.3 Logarithmic Steering Basic Relationship

In the course of investigating flight path angle steering, it was discovered that a logarithmic function of time can also be used to represent the flight path angle that must be produced to achieve a zero angle of attack trajectory. This steering functionalization appears to be competitive with the exponential functionalization.

In logarithmic steering γ_c is functionalized as follows as a linear function of the logarithm of time from launch.

$$\gamma_c = \gamma_{c_{kick}} - M \log(t/ t_{kick}) \qquad (5.14)$$

where the logarithm can either be to the base 10 or base e.

This functionalization is a good approximation of the flight path angle on a zero angle of attack trajectory if the plot of γ versus $\log(t/t_{kick})$ is approximately a straight line. This is the case in the three plots of γ versus t/t_{kick} on a log scale for low, medium and high thrust levels in Figure 5-3, based on the same γ versus time profiles used to determine the plots of Figure 5-1.

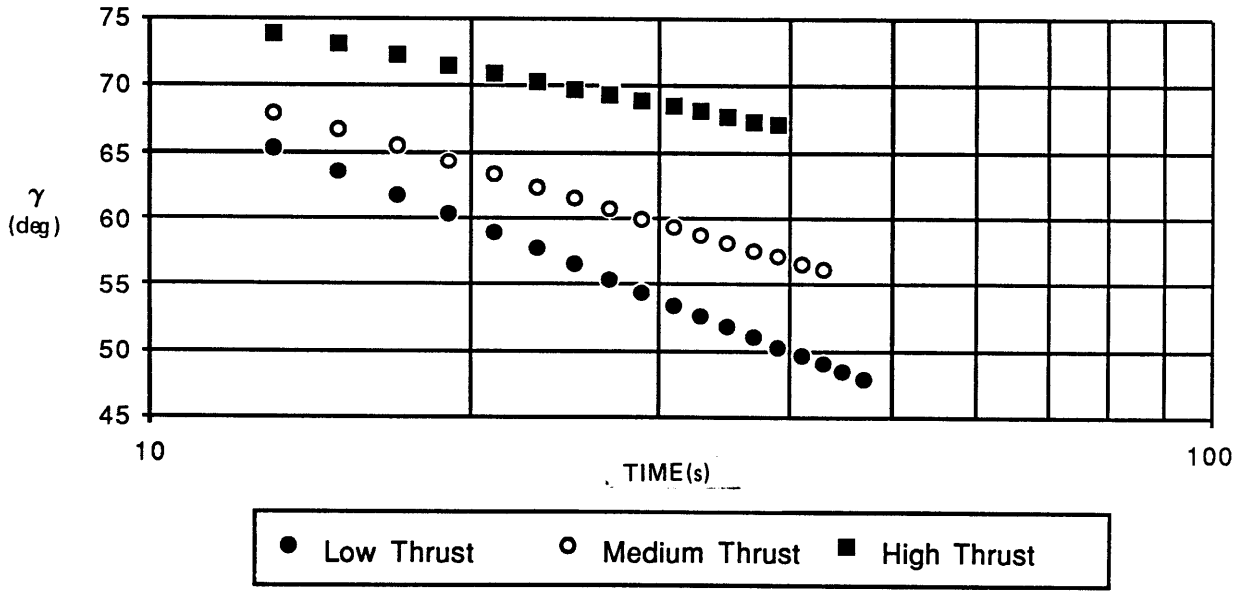

Figure 5-3. Zero angle of attack trajectory γ profile.

5.3.1 Prelaunch Computations

The slope M of the logarithmic functionalization of commanded γ shown in Figure 5-4 is computed as follows from initial and final values of γ and t on the reference trajectory.

$$M = (\gamma_{c_{kick}} - \gamma_{c_{final}})/[\log(t_{final}/t_{kick})] \quad (5.15)$$

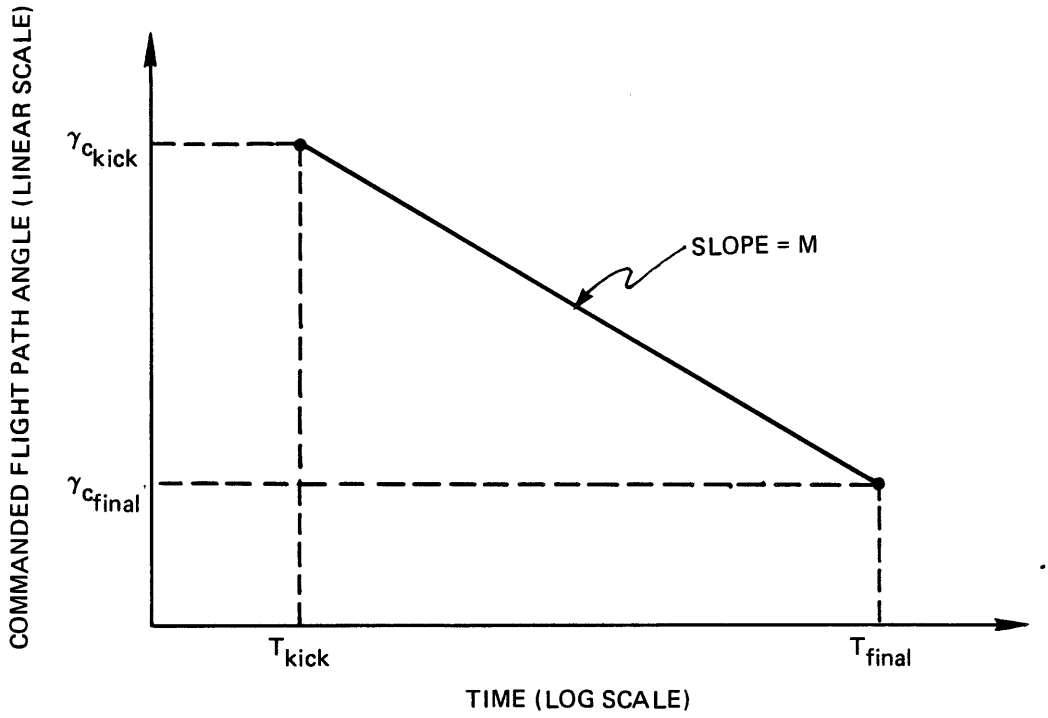

Figure 5-4. Logarithmic functionalization of the commanded flight path angle.

5.3.2 Postlaunch Computations

γ_C is computed from Eq. (5.14) every steering cycle.

5.4 Selection of Steering Functionalizations

To evaluate the steering command functionalizations and to select one for comparison with the predictive steering method, a variety of runs under different wind conditions were performed. The steering functionalizations are evaluated on their ability to meet the desired dynamic pressure end conditions, follow the zero angle of attack trajectory, and avoid excessive loads during the trajectory.

5.4.1 Zero Wind Conditions

The performances of the steering methods under zero wind conditions are summarized in Table 5-1. Plotted results from these runs are shown in Figures 5-5 and 5-6. For the sake of thoroughness many variables are plotted in these figures. However, the chief variables of interest are γ, q and the product $q\alpha$. Figure 5-5 shows a nominal no wind run using exponential steering. Figure 5-6 shows a nominal no wind run using logarithmic steering.

Table 5-1. Comparison of exponential and logarithmic steering performance under nominal conditions.

Steering Method	Max. $Q\alpha$	(Time of Occurrence)	Q_{err}
Exponential	484	(14.29)	6.23
Logarithmic	647	(22.38)	-1.20

The results indicate that the logarithmic steering functionalization method better meets desired end conditions. The $q\alpha$ values along the trajectory however, are slightly higher than for the exponential steering method as shown in Figure 5-6.

The capabilities of the two steering methods to functionalize and follow a desired zero angle of attack γ profile are shown by the plots in Figures 5-7 and 5-8. These plots are based on three flight path angle variables: (1) the functionalized command, γ_c, (2) the zero angle of attack reference, γ_{ref} (which the functionalization is based), and (3) the steering system response for a nominal zero-wind trajectory, γ. Plots of $\gamma_c - \gamma_{ref}$ in Figure 5-7 indicate the functionalization capabilities of the two methods. Plots of $\gamma - \gamma_{ref}$ in Figure 5-8 indicate how closely the steering system follows the zero angle of attack trajectory. Comparing these two figures it is seen that the following may be concluded for both pairs of plots. The exponential method better follows the desired γ profile until maximum q, (approximately 31 secs from launch). After maximum q the logarithmic steering more closely follows the γ profile.

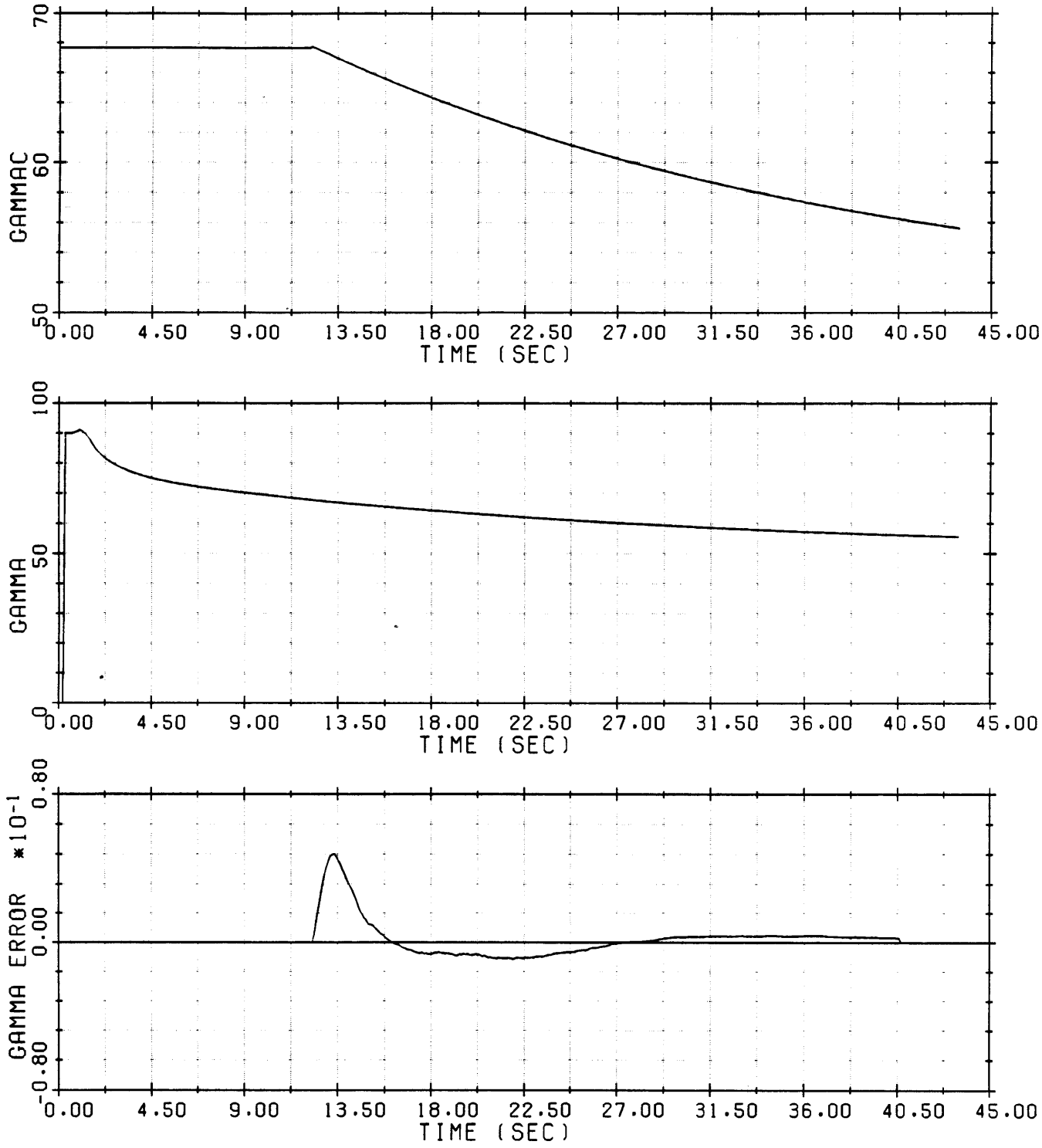

Figure 5-5. Exponential steering performance under nominal conditions.

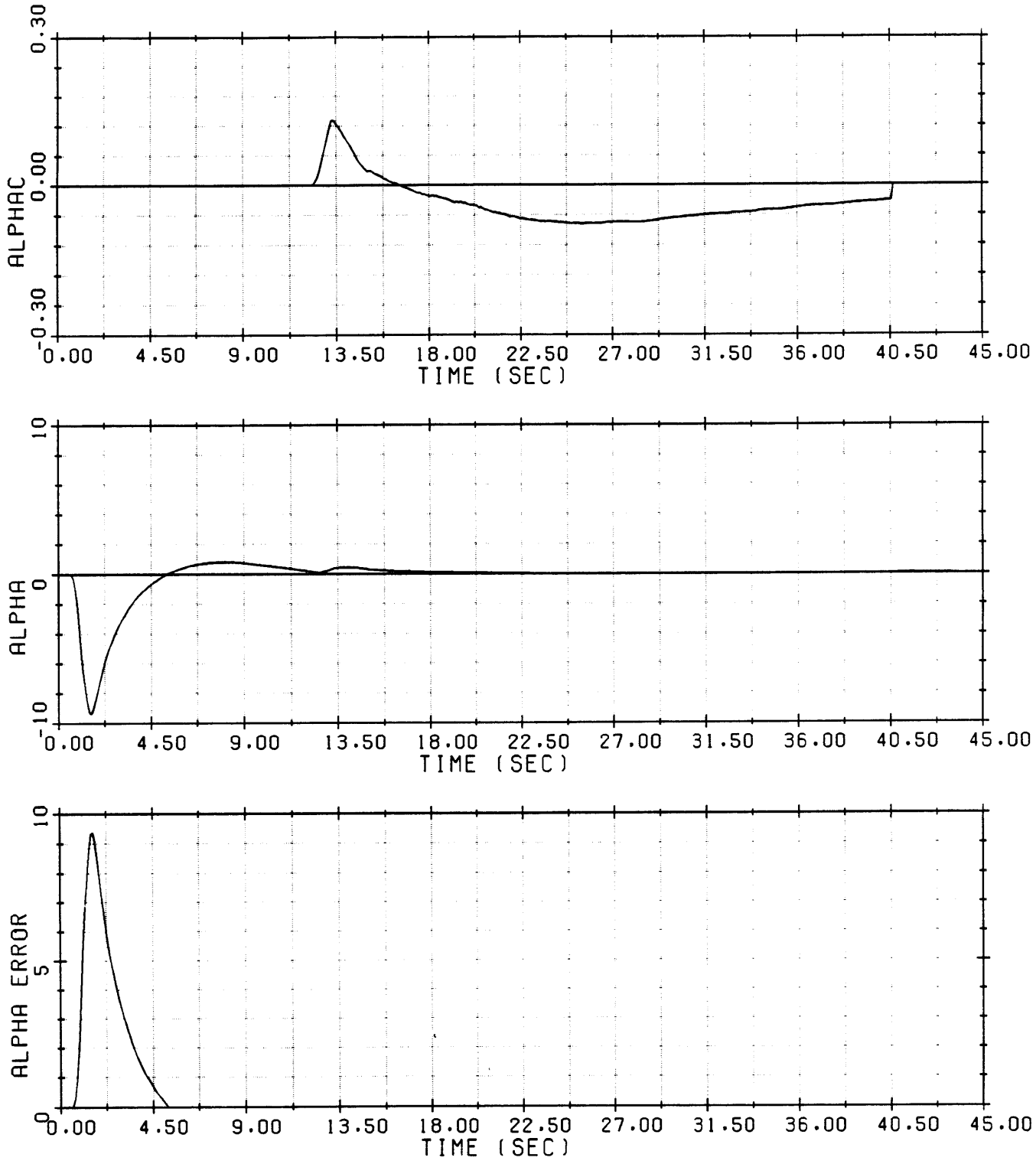

Figure 5-5. Exponential steering performance under nominal conditions. (Cont.)

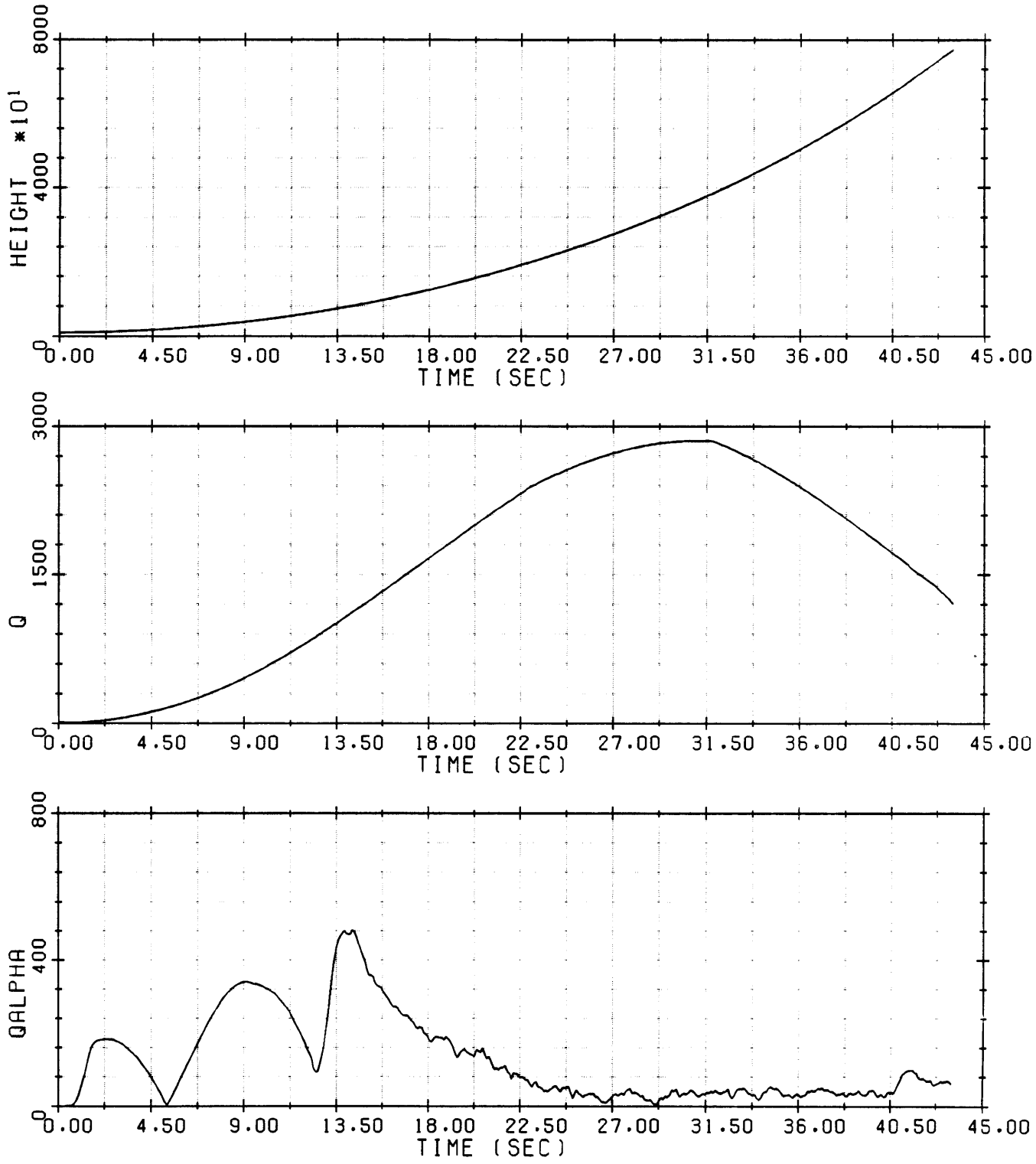

Figure 5-5. Exponential steering performance under nominal conditions. (Cont.)

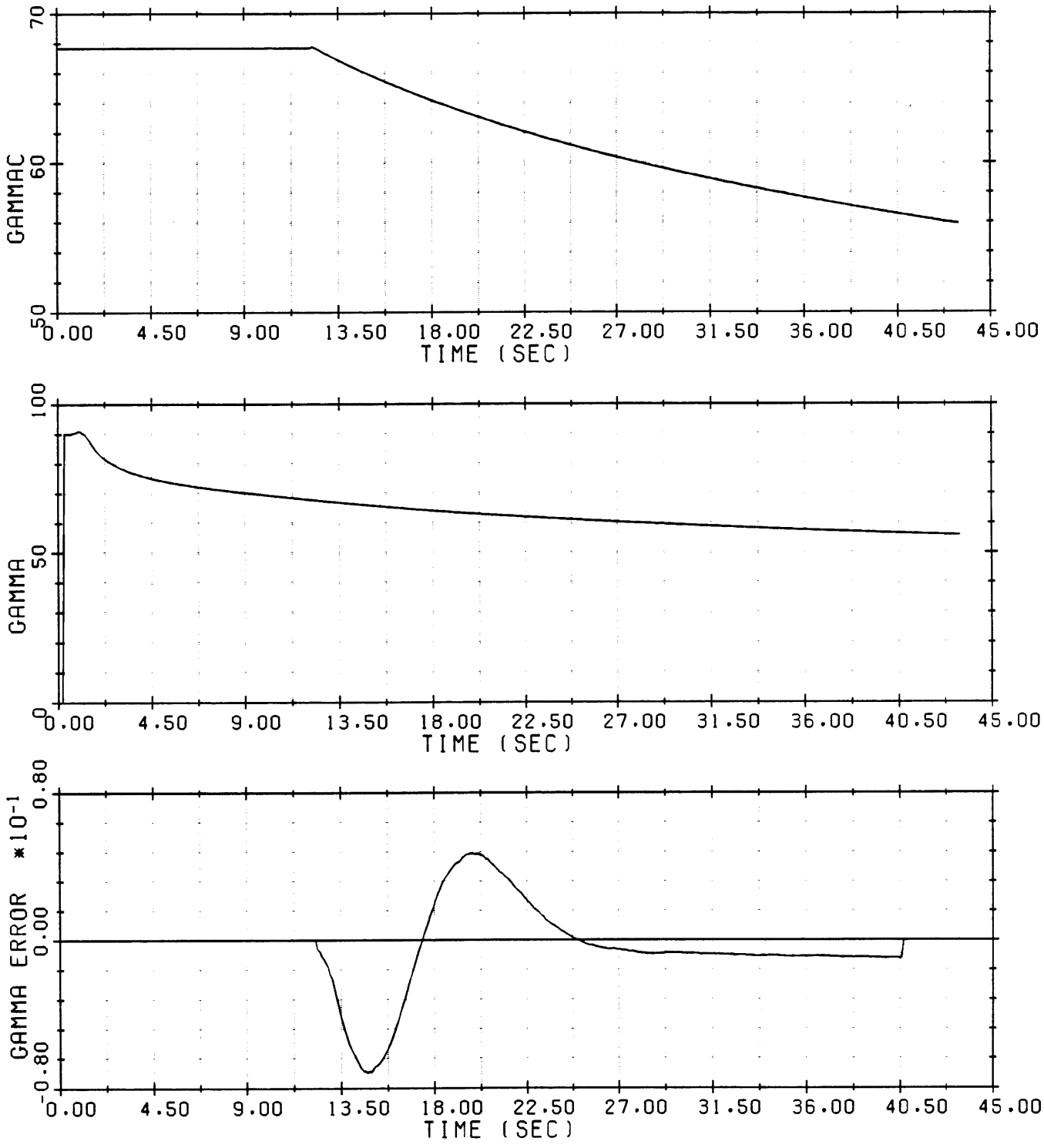

Figure 5-6. Logarithmic steering performance under nominal conditions.

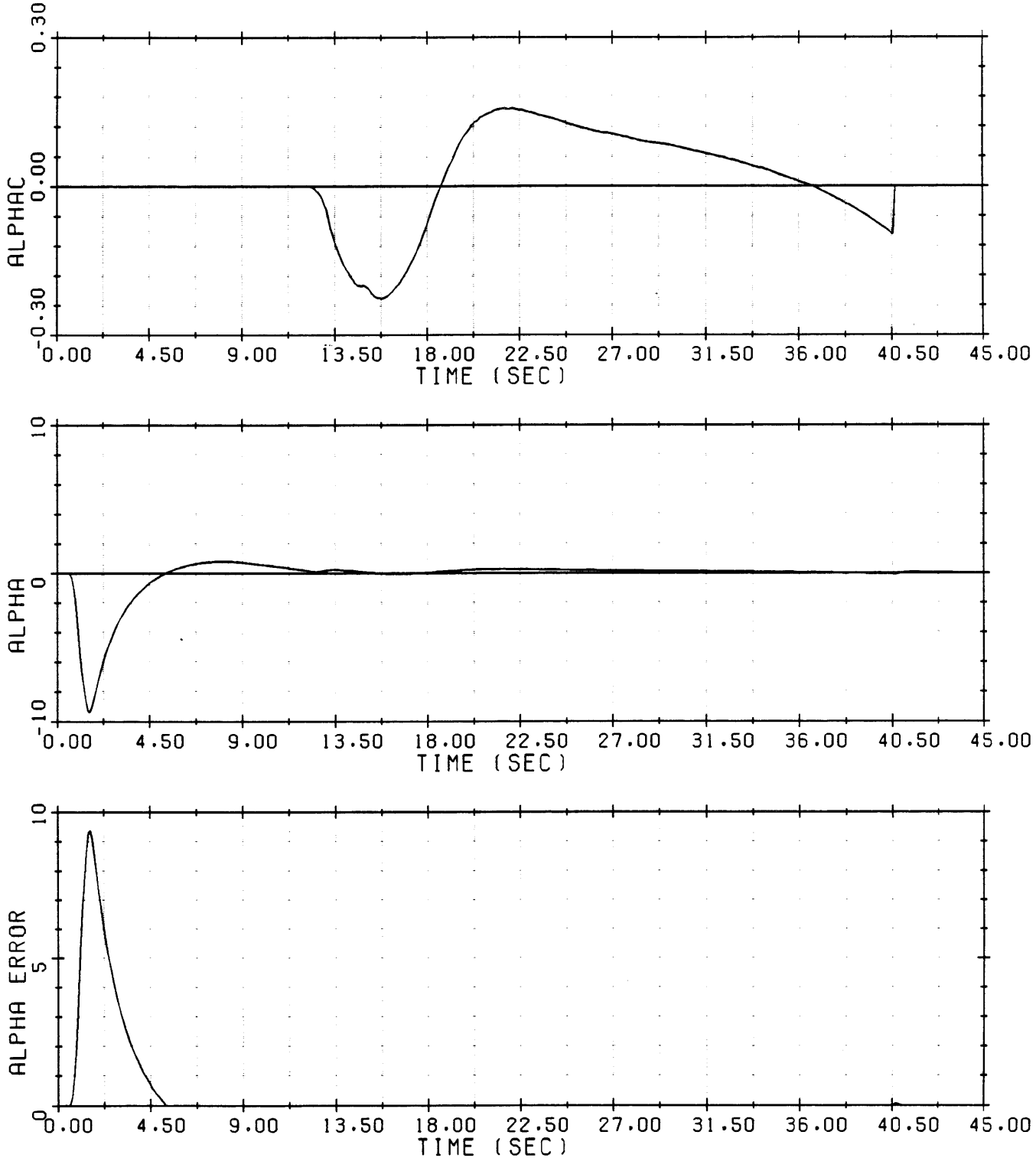

Figure 5-6. Logarithmic steering performance under nominal conditions. (Cont.)

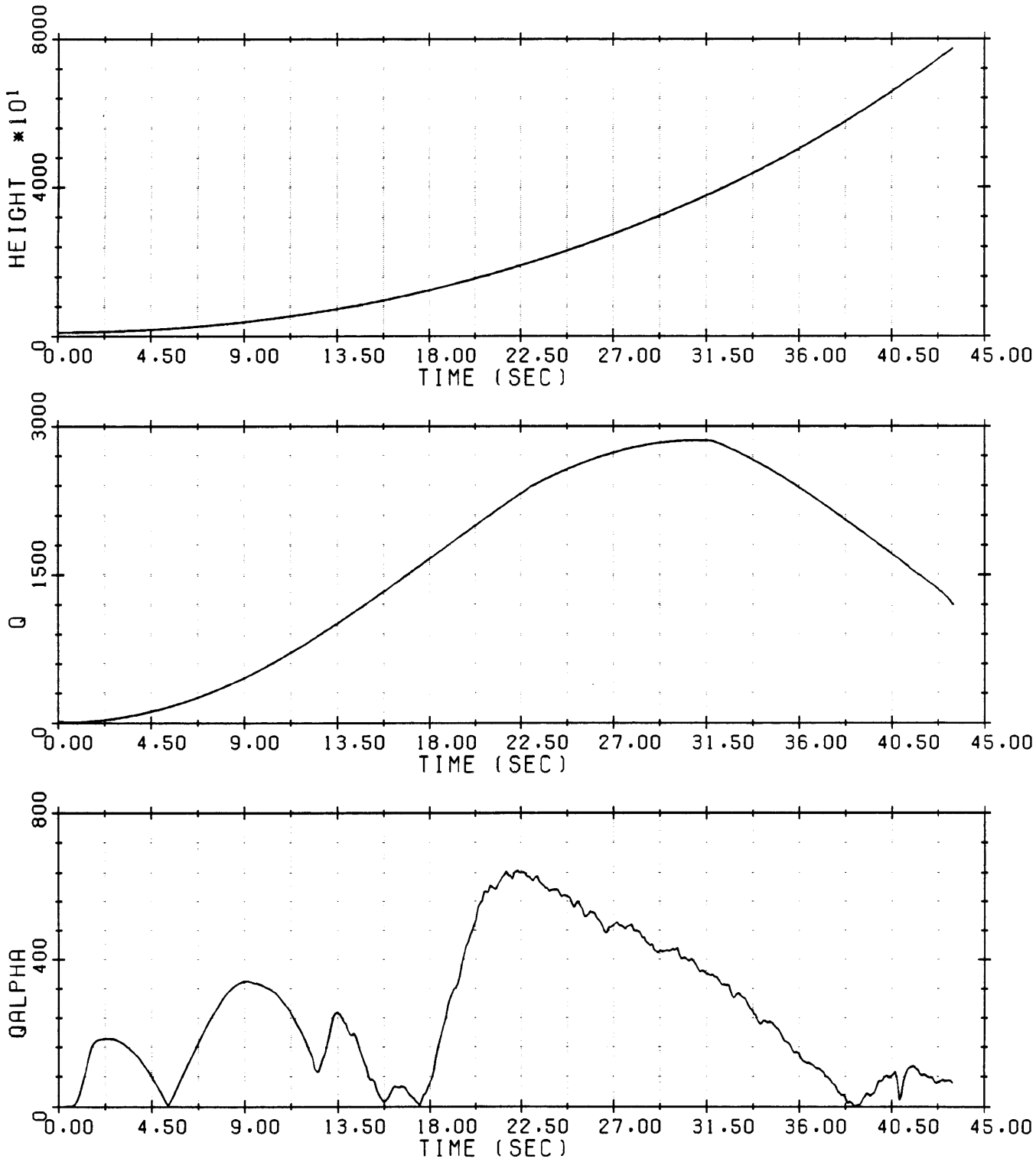

Figure 5-6. Logarithmic steering performance under nominal conditions. (Cont.)

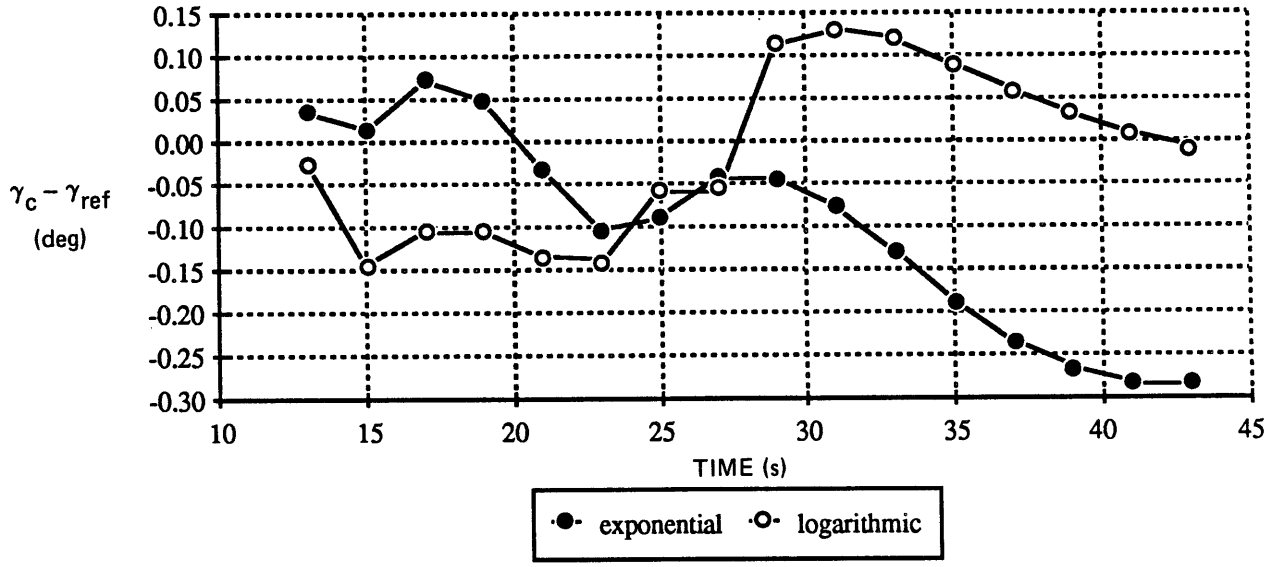

Figure 5-7. Comparison of ability to follow zero angle of attack trajectory with exponential and logarithmic γ_c.

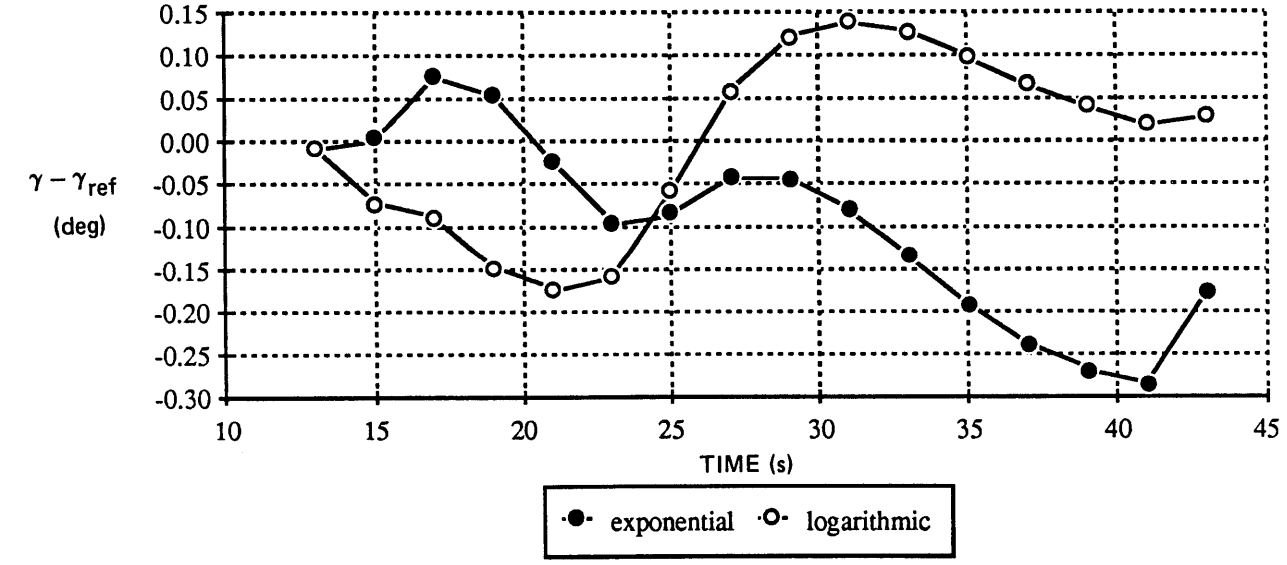

Figure 5-8. Comparison of ability to follow zero angle of attack trajectory with exponential and logarithmic γ.

5.4.2 Off-Nominal Conditions

The results of off-nominal runs are summarized in Table 5-2.

Table 5-2. Summary of exponential vs logarithmic steering comparisons.

Launch χ	Winds	STEERING METHOD					
		Exponential			Logarithmic		
		Max. $Q\alpha$ and	(Time of Occurrence)	Q_{err}	Max. $Q\alpha$ and	(Time of Occurrence)	Q_{err}
90°	No	484	(14.29)	6.23	647	(22.38)	-1.20
	Tail	4792	(30.88)	15.62	4391	(30.87)	-2.42
	Head	4770	(30.91)	-3.66	5022	(30.91)	-1.69
	XWind	2667	(28.99)	21.35	2699	(28.99)	13.17
62°	No	538	(14.29)	6.12	606	(22.38)	3.79
	Tail	4827	(30.89)	14.90	4442	(30.89)	3.20
	Head	4768	(30.92)	-3.55	4990	(30.93)	4.06
	XWind	2678	(29.02)	21.18	2701	(29.03)	18.92
118°	No	462	(14.42)	108.34	905	(20.70)	82.00
	Tail	4643	(31.45)	117.51	4261	(31.43)	81.03
	Head	4958	(31.47)	99.42	5246	(31.42)	82.81
	XWind	2717	(29.54)	125.59	2780	(29.52)	99.02

5.5 Conclusions

Although the logarithmic steering seems to provide slightly better overall performance than the exponential steering, no general conclusion can be made about the relative merits of these functionalizations. These two functionalizations are so close in representing the zero angle of attack flight path angle, that small changes in the method of fitting the functions could change their relative performance. For example, either or both functions could have been fitted using a least squares approach, with possibly different results. Also, the exponential function might have been fitted based on $\dot{\gamma}$ rather than γ behavior. However, since the logarithmic fitting did produce slightly better results it was decided to use the logarithmic function to represent prelaunch-functionalized steering in comparisons with predictive steering.

CHAPTER 6

PREDICTIVE STEERING: STABILITY ANALYSIS

6.1 System Model for Stability Analysis

Figure 6-1 represents the linear system model that will be simplified for stability analysis purposes. The system model has the following features:

(1) There are two sampling periods: T = 0.01 s for the control loop and T_s = 0.1 s for the steering loop.

(2) The nozzle actuator is approximated by a quadratic transfer function,

$$G_{act} = \frac{\omega_n^2}{s^2 + 2\zeta\omega_n s + \omega_n^2}$$

where

$$\omega_n = 62.8 \text{ rad/s}$$

$$\zeta = 0.5$$

(3) The vehicle is approximated as a rigid body.

(4) The rate estimator employs a complementary filter having a break frequency of 4 rad/sec to combine two signals: a derived rate signal based on measured attitude change (for

low frequencies) with an estimated angular rate change obtained from measured engine deflection and IMU-measured ΔV components (for high frequencies).

(5) The angle of attack estimator also employs a complementary filter having a frequency of 4 rad/sec. In this estimator the low frequency signal is based on measurements of engine deflection and ΔV. The high frequency signal is based on measured attitude change over each control cycle.

(6) The rate feedback gain K_{fb} of the control system is set at 0.25 sec for the entire boost phase.

(7) The control gain K_c is adjusted to produce a high-frequency gain margin of 6 dB at the times t = 12.0 s, 24.0 s, 31.1 s, and 42.5 s on the nominal trajectory. The logarithms of K_c are stored versus the nominal mass values at these times. The log of the gain at any particular point is based on estimated mass at that point, and is computed by linear interpolation between tabulated values. The gain is then computed from the antilog of the log gain.

(8) The digital integration gain, K_α, in the control system is constant over the entire trajectory. A value of $K_\alpha = 0.5$ sec^{-1} is employed in the following analysis and simulation studies.

(9) A variable gain K'_{st} in the steering loop compensates for variations in vehicle parameters and vehicle velocity so that the dynamics of the steering loop are approximately the same over the entire boost trajectory. (See Section 3.5 and Appendix D).

(10) The other steering loop gains K_{st} and K_{int} are constant over the entire trajectory. A value of 0.5 was selected for both constants.

(11) The effects of 10 ms control sampling with a computational delay of 5 ms are represented in a frequency response program used to compute

(a) The open-loop transfer function of the control loop, broken at the input to the nozzle actuator, with no steering,

(b) The closed-control-loop transfer function between the commanded angle of attack (α_c) and the estimated angle of attack (α) and

(c) The closed-control-loop transfer function between commanded angle of attack and flight path angle (γ).

(12) The results of (11) are used in combination with approximate steering loop transfer functions in the next two sections to perform stability analyses of

(a) The control loop with the steering loop added in parallel with the feedback of estimated angle of attack (Section 6.2) and

(b) The steering loop, with the effects of the closed control loop included (Section 6.3).

6.2 Approximate Analysis of Steering-Control Interaction

From a control standpoint the steering loop is in parallel with the α-control loop and modifies the open-loop transfer function of the control system in a manner that will be examined below.

In order to simplify the analysis the steering loop will be assumed to have the same sampling period as the control system. It will be shown that the important effects of the steering loop on the control system are in a frequency range where

(1) the sampled variables γ, α, ω, and δ_c can be treated as continuous,

(2) the lags of the zero order holds can be neglected

(3) $\omega \simeq \dot{\alpha}$, and

(4) the relationship $\dot{\gamma} \simeq \frac{1}{K_{st}} \alpha$ derived in Appendix D, is

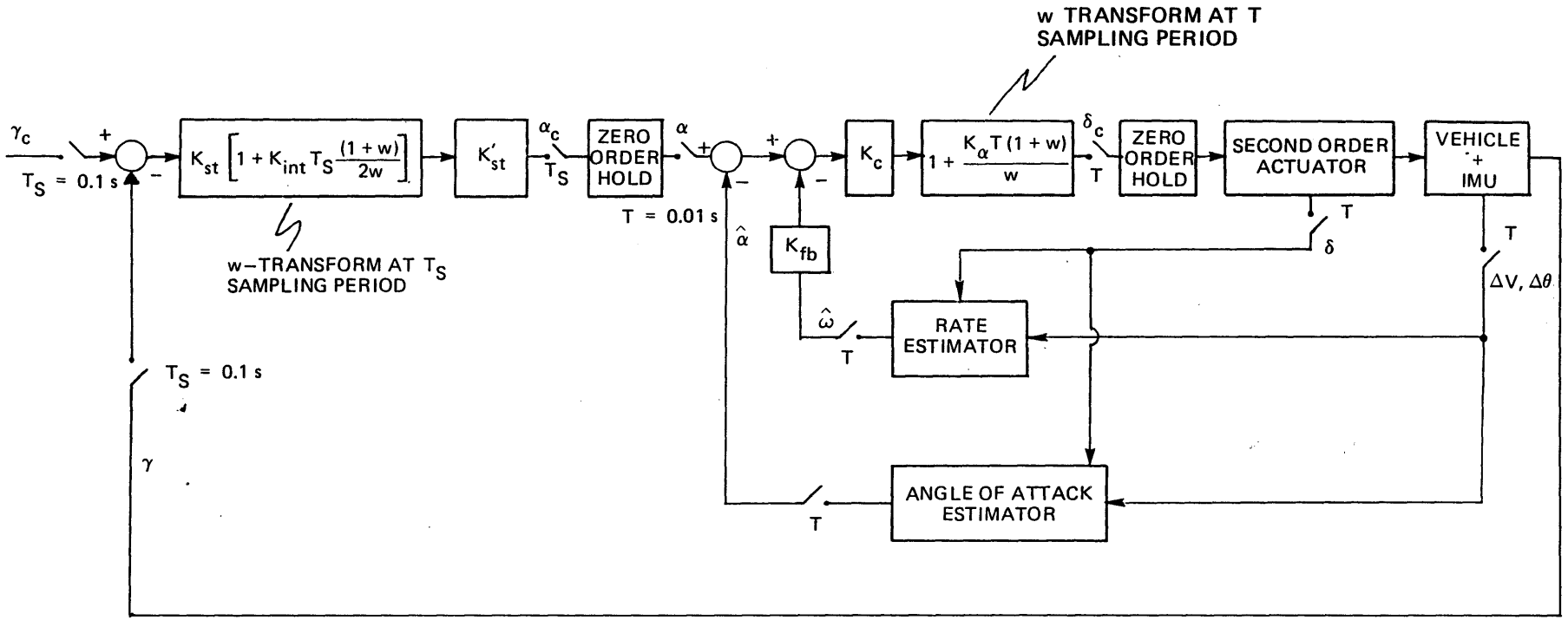

Figure 6-1. Simplified system model for stability analysis purposes.

employed. Employing these assumptions the system model simplifies to the block diagram of Figure 6-2 which in turn can be represented as in Figure 6-3.

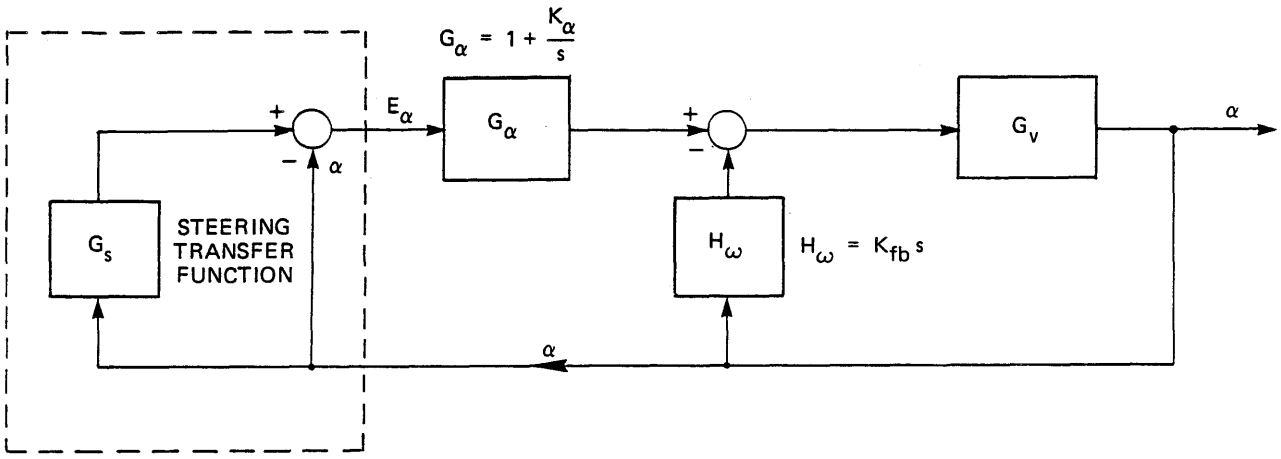

Figure 6-2. Functional block diagram of control-steering loop.

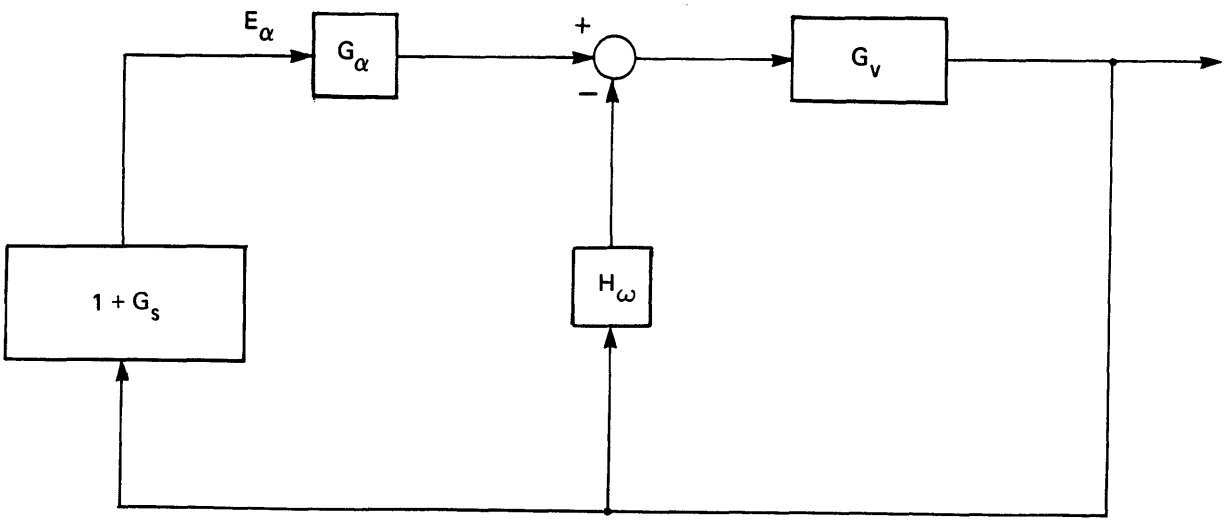

Figure 6-3. Reduced functional block diagram of control-steering loop.

It can be shown that the sinusoidal signal transmission from α to γ then to α_c through the steering loop reduces with frequency and becomes negligible in comparison to the α feedback at frequencies above 6 rad/sec. In the frequency range below 6 rad/sec, where the steering loop does interract with the control system, both the steering and control systems can be approximated by continuous-signal transfer functions.

$$G_s = K_{st} K'_{st} \left(1 + \frac{K_{int}}{s}\right) \frac{\alpha(s)}{\alpha_c(s)} \frac{\gamma(s)}{\alpha(s)} \tag{6.1}$$

where

$$\frac{\gamma(s)}{\alpha(s)} \simeq \frac{1}{s K'_{st}}$$

so that

$$G_s = \frac{K_{st}}{s}\left(1 + \frac{K_{int}}{s}\right)\left(\frac{\alpha(s)}{\alpha_c(s)}\right) \tag{6.2}$$

Within the control system the proportional plus integral control of α can be approximated by

$$G_\alpha = 1 + \frac{K_\alpha}{s} \tag{6.3}$$

and the transfer function between attitude and the rate feedback signal can be approximated by

$$H_\omega = K_{fb}\, s \tag{6.4}$$

Defining the remaining forward-path transfer function in the rate feedback loop of the control system as G_v, the transfer functions of the steering and control loops are related as shown in Figure 6-2.

The effects of the steering loop can be analyzed in terms of the ratio of the control system open loop transfer function, including the steering loop in parallel, to the control system open-loop function without the effect of steering (i.e with $G_s = 0$). The parallel combination the steering and α feedback loops is represented by a single block in Figure 6-3. Examining this figure it is seen that the open loop transfer function of the control system with steering included is

$$G_1 = G_v[H_\omega + (1 + G_s)\, G_\alpha] \tag{6.5}$$

and without steering is

$$G_2 = G_v[H_\omega + G_\alpha] \tag{6.6}$$

The effect of the steering loop on the control system's open-loop transfer function may be expressed in terms of the ratio of G_1 to G_2

$$\frac{G_1}{G_2} = \frac{G_v[H_\omega + (1 + G_s)\, G_\alpha]}{G_v[H_\omega + G_\alpha]} \tag{6.7}$$

which simplifies to

$$\frac{G_1}{G_2} = 1 + \frac{G_s\, G_\alpha}{(H_\omega + G_\alpha)} \tag{6.8}$$

The magnitude and phase properties of the ratio G_1/G_2 are displayed in Table 6-1, where it is seen that the value of this ratio becomes essentially unity, indicating negligible steering effects, at frequencies above 6 rad/sec. The effects of steering on the control

Table 6-1. Effect of the steering loop on the control system's frequency response.

Frequency	Phase (deg)	G_1/G_2 Δ Mag. (dB)	G_1/G_2 Δ Phase (deg)
0.2189	-245.48	13.82	-152.28
0.3240	-235.28	6.68	-134.46
0.4565	-224.40	1.12	-106.95
0.5833	-215.83	-1.36	-80.95
0.9066	-199.84	-2.27	-43.07
1.5921	-179.75	-1.68	-18.73
2.3565	-165.88	-1.24	-9.81
3.7173	-149.98	-0.76	-3.96
6.3154	-134.56	-0.35	-1.10
12.9948	-125.97	-0.10	-0.15

system's open-loop function are approximated in the Nichols Chart of Figure 6-4, where the magnitude vs. phase for the case where steering* is not included are modified by the factor G_1/G_2. This Nichols plot was made for the critical point of maximum dynamic pressure, q, on the vehicle boost trajectory. At this point the gain and phase margins of the control system are at the minimum values. The Nichols Chart plots with and without steering effects conform to a design objective of

Minimum gain margin = 6 dB (for high and low-frequency crossovers of -180°)

Minimum phase margin = 30°

The steering gains were chosen conservatively to have only a small effect on the control system's open loop characteristics. It will be shown in subsequent chapters that the predictive steering can produce significant improvements over fixed function steering, even with conservative selections of steering loop gains.

* Effects of control sampling are included in the Nichols Chart plot without steering.

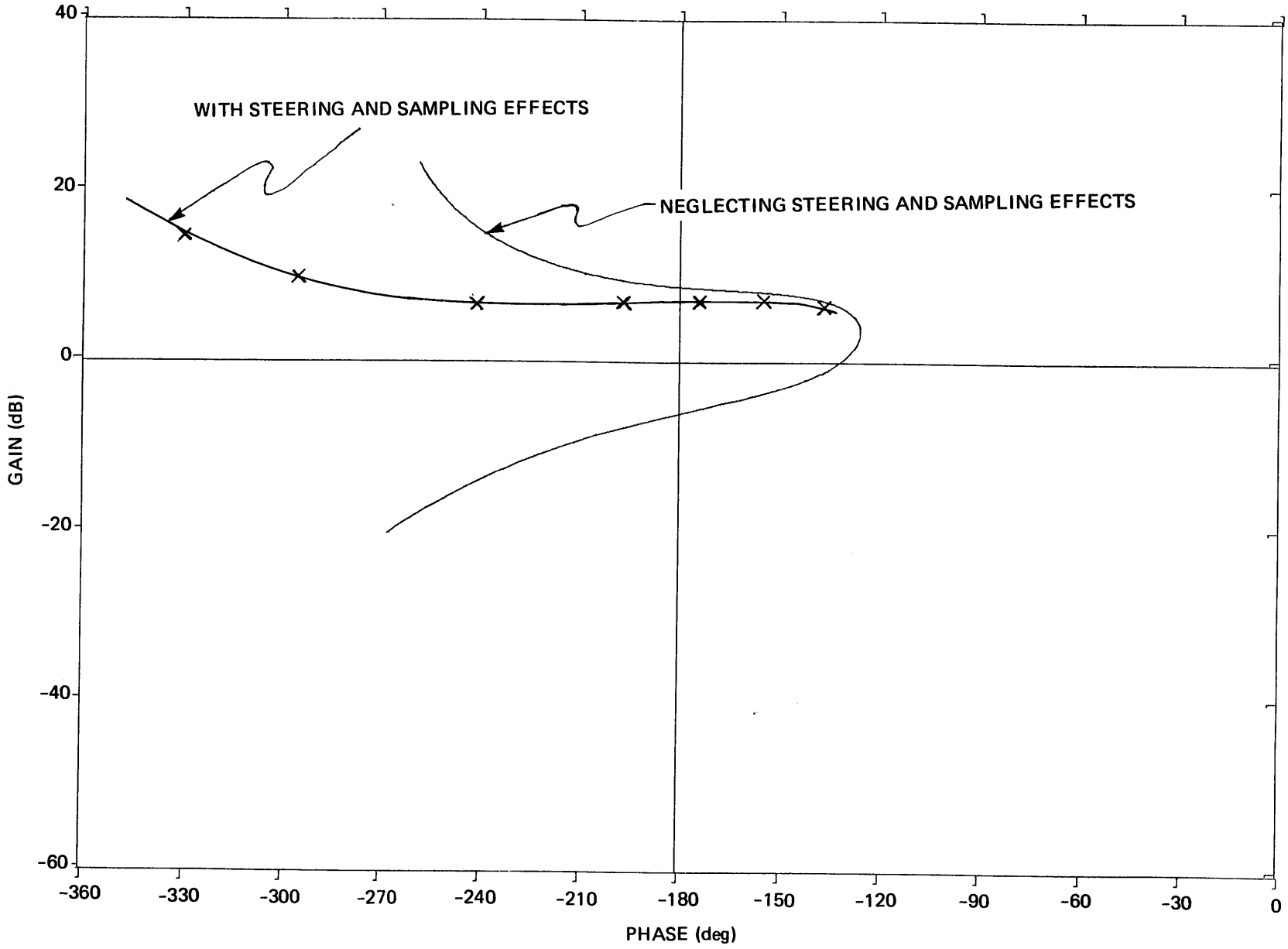

Figure 6-4. Open-loop control system Nichols chart.

The foregoing analysis is of course only approximate since the sampling period of the steering loop is T_s = 0.1s, not the 0.01s period of the control system. However, the following step by step analysis shows that neglecting the effects of the different sampling period of the steering loop is a good approximation:

(1) In the frequency range below 6 rad/s where effects of steering are not negligible the control system is well approximated by a continuous-signal transfer function with essentially the same frequency response as the discrete system.

(2) Assume that the relationship between the flight path angle γ and the commanded angle of attack α_c can be approximated by the continuous-signal transfer function,

$$G_\gamma(s) = \frac{\gamma(s)}{\alpha_c(s)} \tag{6.9}$$

The discrete transfer function $G^*_\gamma(s)$ for the steering loop is then obtained combining $G^*_\gamma(s)$ with a transfer function to represent the zero order hold and then using the sampling theorem to obtain the relationship

$$G^*_\gamma(s) \simeq \frac{1}{T_s} \sum_{-\infty}^{\infty} F_{ZOH}(s + jnw_s)\, G_\gamma(s + jnw_s) \tag{6.10}$$

where

$$F_{ZOH}(s) = \frac{1 - e^{-sT_s}}{s}$$

and

$$\omega_s = \frac{2\pi}{T_s} = \frac{2\pi}{0.1} = 62.8 \text{ rad/s}$$

This transfer function can be shown to be well approximated in frequencies below 6 rad/s by using only the n=0 term of the series, obtaining

$$G_\gamma^*(s) = \frac{1 - e^{-sT_s}}{s\,T_s}\, G_\gamma(s) \tag{6.11}$$

Also in the frequency range below 6 rad/s the zero order hold factor can be approximated by

$$\frac{1 - e^{-sT_s}}{s\,T_s} \simeq e^{-sT_s/2} \tag{6.12}$$

with the result that

$$G_\gamma^*(s) \simeq e^{-sT_s/2}\, G_\gamma(s) \tag{6.13}$$

(3) If the steering loop were continuous, its integral plus proportional operation would be represented by the function

$$G_s(s) = K_{st}\left[1 + \frac{K_{int}}{s}\right] \tag{6.14}$$

In the discrete implementation of this loop this function is replaced by either the z transform

$$G_s(z) = K_{st}\left[1 + \frac{K_{int}\,T_s}{1 - z^{-1}}\right] \tag{6.15}$$

or the equivalent w-transform, shown in Figure 6-1,

$$G(w) = K_{st}\left[1 + K_{int}\, T_s \frac{1 + w}{2w}\right] \tag{6.16}$$

The w-transform is particularly useful because of the following relationship between imaginary values of s and w:

$$w = \tan \frac{s\, T}{2} \tag{6.17}$$

For small sT/2 values this can be approximated as $w \simeq sT/2$. Letting $w = sT/2$ in $G_s(w)$ the approximate pulse transform $G_s^*(s)$ is obtained:

$$G_s^*(s) \simeq K_{st}\left[1 + \frac{K_{int}\left(1 + \frac{s\, T_s}{2}\right)}{s}\right] \tag{6.18}$$

(4) The overall steering loop transfer function is then approximately represented by the product of the transfer functions described by Eq.s (6.13) and (6.18), giving

$$G_{s1}^*(s) \simeq K_{st}'\, K_{st}\, G_\gamma(s)\; e^{-sT_s/2}\left[1 + \frac{K_{int}\left(1 + \frac{s\, T_s}{2}\right)}{s}\right] \tag{6.19}$$

This function representing the effects of steering loop sampling must be compared with another function neglecting the effects of sampling:

$$G_{s2}^*(s) = K_{st}'\, K_{st}\, G_\gamma(s)\left[1 + \frac{K_{int}}{s}\right] \tag{6.20}$$

The effects of sampling are revealed by the magnitude and phase properties of the ratio

$$R_s(s) = \frac{G^*_{s1}(s)}{G^*_{s2}(s)} = e^{-sT_s/2} \left[\frac{1 + \frac{K_{int}\,(1 + \frac{s\,T_s}{2})}{s}}{1 + \frac{K_{int}}{s}} \right]$$

or

$$R_s(s) = \frac{e^{-sT_s/2} \left[1 + \frac{K_{int}\,T_s}{2} + \frac{K_{int}}{s} \right]}{\left[1 + \frac{K_{int}}{s} \right]} \qquad (6.21)$$

Letting $K_{int} = 0.5$ and $T_s = 0.1$,

$$1 + \frac{K_{int}\,T_s}{2} = 1.025$$

which is close to unity. Assuming that this term is unity,

$$R_s(s) \simeq e^{-sT_s/2} \qquad (6.22)$$

(5) It may be concluded from Eq. (6.22) that the continuous-signal steering-loop transfer function of Eq. (6.1) can be multiplied by $e^{-sT_s/2}$ to approximate the effects of sampling:

$$G_s = \frac{K_{st}}{s}\left(1 + \frac{K_{int}}{s}\right)\left(\frac{\alpha(s)}{\alpha_c(s)}\right)\left[e^{-sT_s/2}\right] \qquad (6.23)$$

Using this modified expression for G_s it was found that the open loop function of the control system with steering sampling effects included changed very little from the continuous-signal function. At the frequency w = 2.3565, close to the low-frequency crossover of 180°, the gain was changed by only -0.2 dB and the phase angle was changed by only +1 degree. Slightly smaller changes occurred at the maximum frequency of interest, 6 rad/sec.

6.3 Steering Loop Stability Analysis

Following the line of reasoning in the step by step analysis of steering sampling effects in Section 6.2, the steering loop can be approximated by the combination of discrete and continuous-signal transfer functions of Figure 6-5. Using the transfer function between α_c and γ based on the control sampling frequency, the product of this function times $K_{st}\,K'_{st}$ is plotted in the Nichols Chart of Figure 6-6. The added effects of the other elements of the steering loop of Figure 6-5 are shown by the points marked "x" in Figure 6-6. The overall steering loop plot of Figure 6-6 shows a large high-frequency gain margin of 20 dB and a large phase margin of 60°.

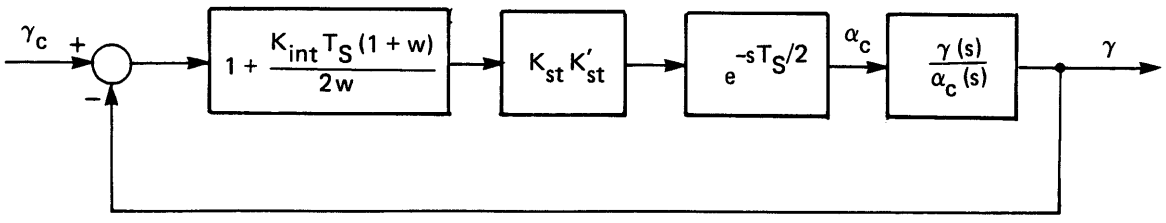

Figure 6-5. Steering loop block diagram.

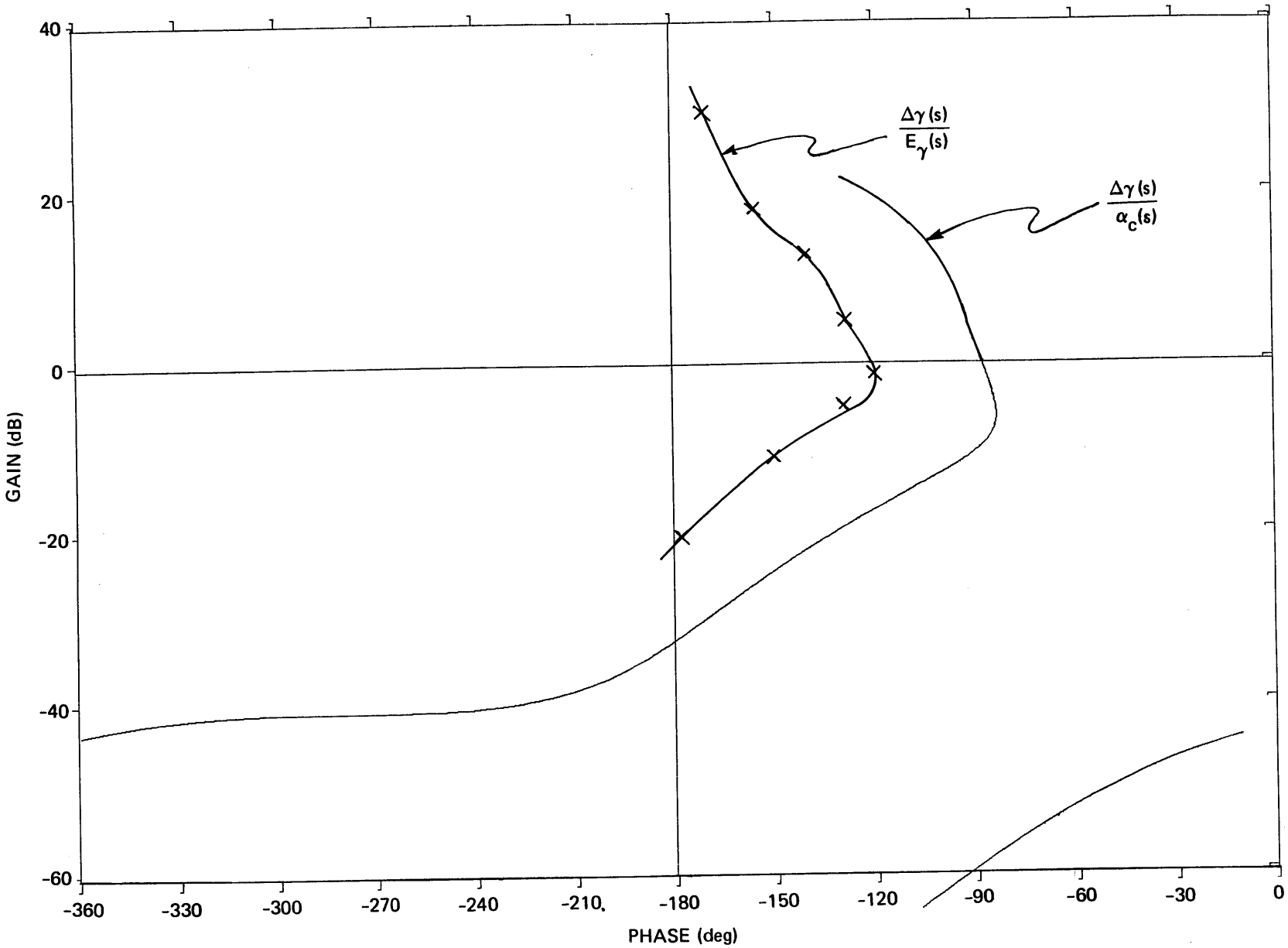

Figure 6-6. Nichols chart. Plots of $\frac{\Delta\gamma}{\alpha_c}$ and $\frac{\Delta\gamma}{E_\gamma}$.

6.4 Effects of Predictive Updates of the Steering Command

Figure 6-7 shows how it is possible to approximate the dynamic effects of predictive steering updates of the commanded flight path angle γ_c by an additional feedback path in the steering loop in parallel with flight path angle feedback. The use of zero order hold to supply $\Delta\gamma_c$ in Figure 6-7 is an approximation of the various schemes presented in this thesis which compute γ_c not only at predictive steering updates but also at steering cycles between these updates. This additional feedback path represents the correction to γ_c, at the predictive steering update time, required to compensate for the deviation in altitude, H, from the nominal value. The sensitivity of γ_c to changes in H is computed by the predictive steering in the process of determining γ_c. This sensitivity is represented in Figure 6-7 by the gain K_H. The variables $\Delta\gamma_c$, $\dot{\Delta\gamma}$, ΔH, in this figure represent variations from nominal values. The altitude variation ΔH is obtained by integrating

$$\dot{\Delta H} = [V \cos\gamma]\, \Delta\gamma \tag{6.24}$$

which was derived by differentiating the basic relationship,

$$\dot{H} = V \sin\gamma \tag{6.25}$$

neglecting the effects of γ on V.

It can be shown that the effects of the γ_c-loop sampling period of N_{steer} steering cycles can be approximated by adding a delay factor of $e^{-s(N_{steer}\, T_S/2)}$ to a continuous-signal γ_c feedback as shown in Figure 6-8. This factor has a delay time of

$$\frac{N_{steer}\, T_S}{2} = 1.25 \text{ s} \tag{6.26}$$

for the N_{steer} value of 25 that has been chosen for stability analysis.

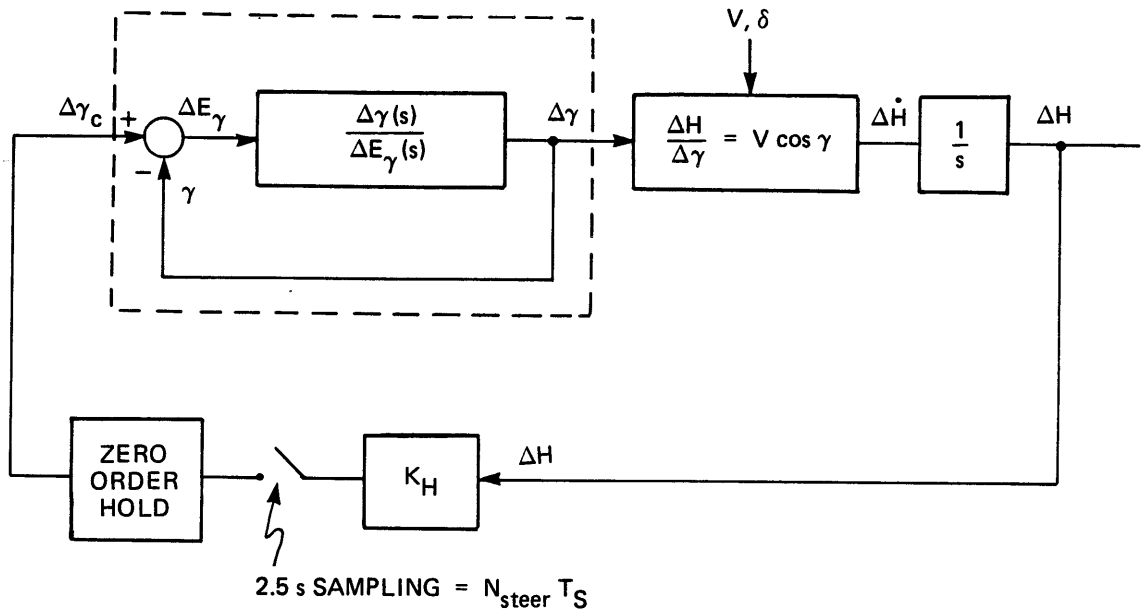

Figure 6-7. Steering loop including 2.5 s sampling effects.

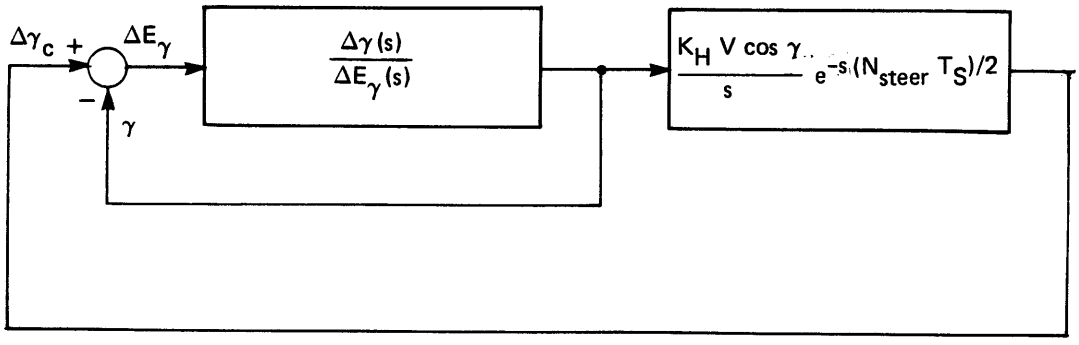

Figure 6-8. Continuous representation of Figure 6-7.

$$\frac{\Delta\gamma(s)}{E_\gamma(s)} \quad F(s) \tag{6.27}$$

where

$$F(s) = 1 + \frac{K_H V \cos\gamma}{s} \; e^{-sN_{steer}T_S/2} \tag{6.28}$$

From Eq. (6-28) it is seen that the $\Delta\gamma_c$ feedback represented by the second term of F(s) introduces a destabilizing phase lag into the open-loop function. Since this phase lag is determined to a great extent by the gain factor $K_H V\cos\gamma$, the way in which this factor varies along the trajectory is of primary interest.

Values of $K_H V\cos\gamma$ are presented in Table 6-2 for various points along the nominal, no-wind trajectory resulting from predictive steering. It is seen that $K_H V\cos\gamma$ increases rapidly as t_{go} approaches zero. Fortunately, it is not necessary to continue steering to the point of engine burnout. In fact, it was decided to command a zero angle of attack for $t_{go} < 3$ secs so as to insure that the angle of attack is close to zero at staging. Therefore, the last tabulated value of $K_H V\cos\gamma$ for $t_{go} = 3.1$ sec is the largest value of concern. Using this value, the magnitude and phase of the factor F(s), with and without the sampling delay, $\frac{N_{steer}\ T_S}{2} = 1.25$ are as presented in Table 6-3. This table shows that the selected sampling period for the predictive steering has negligible effect on F(s).

Table 6-2. $K_H V\cos\gamma$ vs time and t_{go}.

Time	t_{go}	$1/t_{go}$	$K_H \times 10^{-5}$ (rad/ft)	V	γ	$K_H V \cos\gamma$
12.10	30.6	0.03	1.87	936.60	67.68	0.0066
22.10	20.6	0.05	2.50	1836.70	62.57	0.0212
32.10	10.6	0.09	4.00	3091.30	58.74	0.0642
37.10	5.6	0.18	6.54	3888.90	57.33	0.1373
39.60	3.1	0.32	10.47	4348.60	56.69	0.2500

Table 6-3. Effects of added γ_c feedback.

Frequency	F (s)			
	With Sampling Delay		Without Sampling Delay	
	Δ Mag. (dB)	Δ Phase (deg)	Δ Mag. (dB)	Δ Phase (deg)
0.2034	0.47	-30.17	1.63	-34.00
0.3011	-0.59	-26.98	0.82	-24.50
0.5036	-1.23	-14.69	0.31	-15.24
1.0	-1.20	-2.63	0.09	-7.81
2.9788	0.22	2.12	0.01	-2.63

It should be recognized that while the worst-case point in the trajectory for the added effects of γ_c feedback is at t_{go} = 3.1s, the worst-case point in the trajectory for the combined steering and control system without γ_c feedback is at maximum dynamic pressure, close to t_{go} = 32.1 in Table 6-2. At the latter point the value of $K_H V \cos\gamma$ is only 0.064, which yields very little change in the open-loop steering characteristics resulting from the added factor F(s). Therefore, in order to demonstrate that there can be no significant change in stability resulting from the effects of γ_c feedback, it was decided to combine the two worst cases: the $\frac{\Delta\gamma(s)}{E_\gamma(s)}$ function for maximum dynamic pressure and the F(s) for t_{go} = 3.1 s. The results of this overly pessimistic combination, are shown in the Nichols Chart plotted in Figure 6-9. It can be seen that the design objectives of 6 dB gain margin and 30 degree phase margin are easily met.

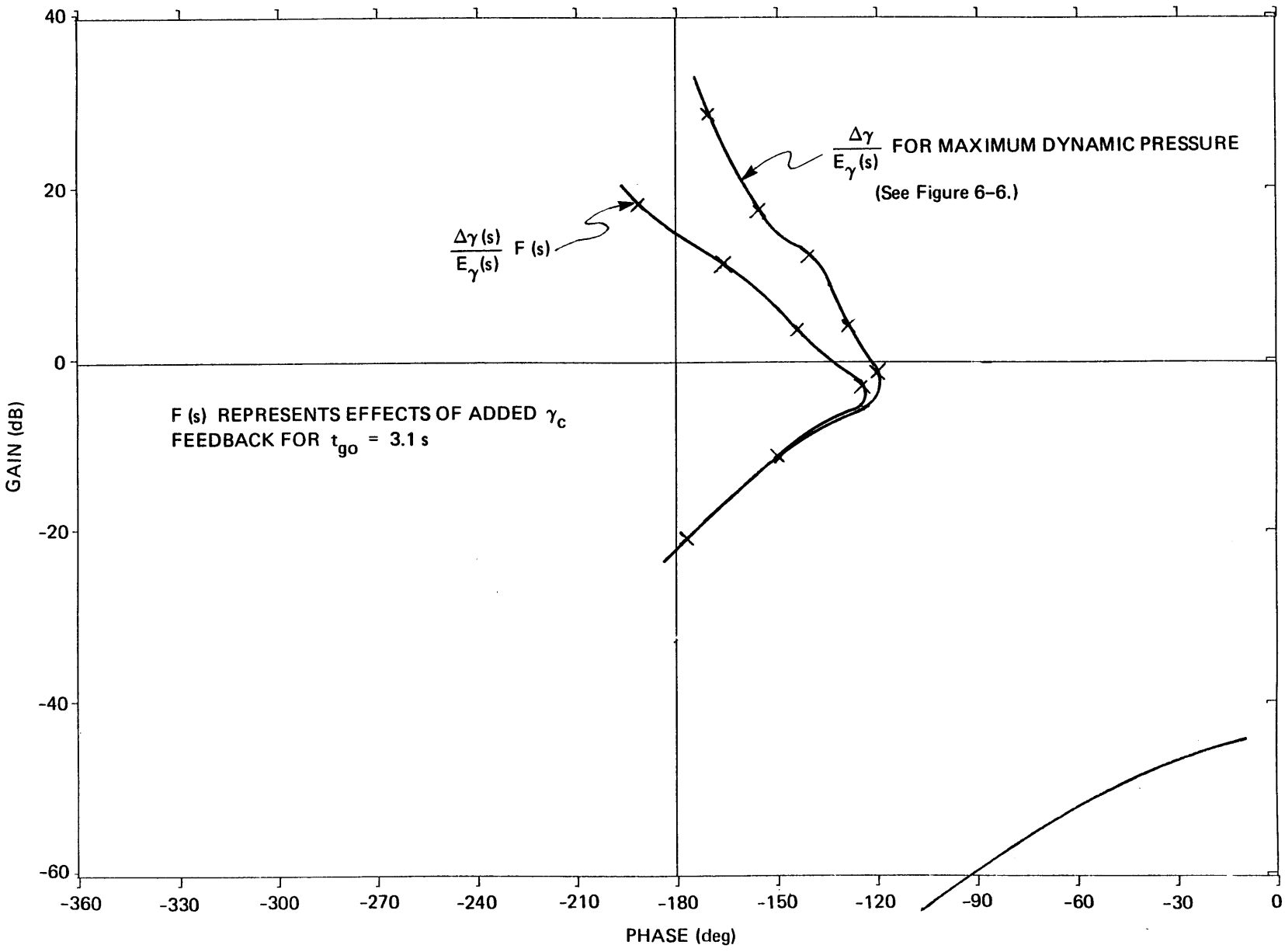

Figure 6-9. Nichols chart showing effect of predictive steering updates.

CHAPTER 7

PREDICTIVE STEERING: SIMULATION RESULTS

This chapter presents the results of simulations used to evaluate the performance of the predictive steering method. The logarithmic steering method discussed in Chapter 5 is used as a comparison. To thoroughly evaluate these steering methods a variety of off-nominal flight conditions in thrust, launch angle, and winds are considered.

As specified previously, the objective of the steering method is to achieve a staging dynamic pressure of 1200 psf and maintain a low $q\alpha$ profile during the entire trajectory. It was arbitrarily decided to select a design limit of 12,000 deg lb/ft^2 for the maximum value of $q\alpha$. All runs, except where noted, are made with $q\alpha_c$ being limited to 10,000 deg lb/ft^2.

The quantities tabulated for the simulation runs are the following: maximum $q\alpha$, time in the trajectory at which maximum $q\alpha$ occurred, and the difference, Q_{err}, between the desired and the attained dynamic pressure at staging.

For comparitive purposes some previously presented results are repeated in the tables in this chapter. For example, results from Chapter 5 are repeated so that a direct comparison can be made between predictive and logarithmic steering methods.

7.1 Comparison of Integration Methods

A comparison was made of performance characteristics of possible integration methods used for predictive steering simulation as described

in Section 3.3. Three different integration methods were investigated: Runge-Kutta, rectangular (modified Euler) and simplified rectangular (Euler). The goal was to select the integration method that would achieve sufficient accuracy without requiring excessive computation time. The Runge-Kutta integration is the most accurate method, but incurs a penalty of computer time usage since it requires four iterations as opposed to one for the other two methods.

The three integration methods are described below in terms of the integration of

$$\frac{dy}{dx} = f(x,y) \tag{7.1}$$

with a step size in x of h.

7.1.1 Runge-Kutta Method

The Runge-Kutta method provides fourth order accuracy and has the form

$$y_{n+1} = y_n + \frac{1}{6}(b_1 + 2b_2 + 2b_3 + b_4) \tag{7.2}$$

where

$$b_1 = h\, f(x_n, y_n)$$

$$b_2 = h\, f(x_n + h, y_n + \tfrac{1}{2}b_1)$$

$$b_3 = h\, f(x_n + h, y_n + \tfrac{1}{2}b_2)$$

$$b_4 = h\, f(x_n + h, y_n + b_3)$$

y_n = current value of y,

y_{n+1} = value of y at end of integration step,

7.1.2 Rectangular Method (modified Euler)

The rectangular, or modified Euler method provides second order accuracy and is less accurate than the above method. The rectangular method has the form

$$y_{n+1} = y_n + \frac{h}{2}\left(f(x_n,y_n) + f(x_{n+1},z_{n+1})\right) \qquad (7.3)$$

where

$$z_{n+1} = y_n + h\, f(x_n,y_n)$$

7.1.3 Simplified Rectangular (Euler) Method

The simplified rectangular, or Euler method provides only first order accuracy but requires the least computation time. This integration method has the form

$$y_{n+1} = y_n + h\, f(x_n,y_n) \qquad (7.4)$$

The three integration methods were compared by using them to implement the predictive steering method for different step sizes at two different points along a nominal, no-wind trajectory and observing the tradeoffs between accuracy and computation effort. The trajectory points observed were at 12 seconds,which is at the end of the launch maneuver, and at 32 seconds, which is at maximum dynamic pressure. The results for the 12 second point are shown in Table 7-1 and the 32 second point are shown in Table 7-2.

Table 7-1. Comparison of three different integration methods using the initial conditions at T = 12.00 s.

Integration Time Interval (s)	Difference between burnout and desired dynamic pressure (PSF)		
	Runge-Kutta	Rectangular	Simplified
0.1	0.0	-0.32	-22.66
0.5	-1.88	-3.64	-111.6
1.0	-4.25	-8.11	-215.1
2.0	-8.80	-17.84	-397.5

Table 7-2. Comparison of three different integration methods using the initial conditions at T = 32.00 s.

Integration Time Interval (s)	Difference between burnout and desired dynamic pressure (PSF)		
	Runge-Kutta	Rectangular	Simplified
0.1	0.0	-0.02	-20.08
0.5	-0.34	-0.51	-98.83
1.0	-0.81	-1.29	-193.2
2.0	-1.75	-3.28	-365.9

Comparing Tables 7-1 and 7-2 it is seen that the accuracy of the predictive steering integration improves with time during the atmospheric boost phase. Since the relatively large errors shown in Table 7-1 can be corrected later in the boost phase when prediction errors are lower, such as shown in Table 7-2, this latter table provides a better indication of the performance of the integration methods. The dynamic pressure error of 1.29 psf resulting from the rectangular integration with a 1 second integration interval is probably adequate for predictive steering. However, in order to show the effects of aspects other than integration errors on performance it was decided to use the high accuracy Runge-Kutta method with 0.1 sec integration step in comparitive simulation runs.

7.2 Selection of Predictive Steering Parameter Values

The values of N_{steer} and $COUNT_{delay}$ discussed in Chapter 3 will be selected in this section. These parameters were selected based on performance for both nominal as well as two severe flight condition cases. The conditions used are (a) 118° launch, constant thrust with a head wind (b) 10% thrust gradient from beginning to end of boost phase with a head wind and 90° launch. The following simulation runs do not have the altitude deviation compensation and the parceling out of predictive steering commands which are considered subsequently in this chapter.

7.2.1 Selection of N_{steer} Value

The effects on performance of using different N_{steer} values of 12, 25, 50, and 100 are shown in Table 7-3.

Table 7-3. N_{steer} studies.

N_{steer}	Flight Conditions	Max. Qα and (Time of Occurrence)		Q_{err}
12	A	4,403	(34.49)	-10.46
	B	7,830	(34.66)	-4.94
	C	10,287	(30.95)	-0.42
25	A	6,843	(35.69)	-10.80
	B	9,727	(35.71)	-5.32
	C	12,808	(25.75)	5.16
50	A	8,033	(38.23)	-9.73
	B	12,182	(38.39)	-5.19
	C	13,255	(23.38)	18.18
75	A	4,919	(28.16)	-9.13
	B	7,756	(28.50)	-2.05
	C	11,807	(20.82)	28.58
100	A	1,541	(23.08)	-0.06
	B	5,917	(14.03)	10.75
	C	13,443	(23.37)	49.25

Flight Condition
A: 90° Launch, Nominal Thrust, No Wind
B: 118° Launch, Nominal Thrust, Head Wind
C: 90° Launch, 10% Thrust Gradient, Head Wind

As can be seen from the above results flight condition B provides the most severe test of update frequency effects. Based on these results a value of N_{steer}= 25 was selected since it performs well in all conditions yet requires fewer updates than N_{steer} = 12. For flight

condition C the error in dynamic pressure at staging increases drastically beyond N_{steer}= 25. For N_{steer} values of 12 and 25 this error is -0.42 and 5.16 psf, respectively. Then for N_{steer} > 25 the error takes on values of 18.18, 28.58 and 49.25 psf, respectively. Based on these results a value of N_{steer} = 25 was selected since it performs well in all conditions yet requires fewer updates than N_{steer} = 12.

It must also be noticed that the maximum $q\alpha$ increases from N_{steer} = 12 to 25 and then decreases from N_{steer} = 25 to 100.

Closer inspection of the results in Table 7-3 shows that the maximum $q\alpha$ value exceeds the design limit of 12,000 deg lb/ft^2 for the case where N_{steer} = 25 and there is a 10% thrust gradient. Additional simulation runs are presented in Tables 7-4a and 7-4b which show how the maximum $q\alpha$ is reduced by (a) reducing the high-altitude limit on $q\alpha_c$ from 10,000 to 5,000 deg lb/ft^2 and (b) reducing the thrust gradient to 5%.

Table 7-4a. Effects of $Q\alpha$ limits for 10% thrust gradient.

$Q\alpha$ Limits	Wind Direction	Max. $Q\alpha$ and (Time of Occurrence)		Q_{err}
10 k	Tail	13,260	(33.40)	-3.26
	Head	12,800	(25.75)	5.16
10 k for H $\leq$ 25 k	Tail	8,655	(33.39)	-0.70
5 k for H > 25 k	Head	11,080	(25.48)	52.03

Examining these tables it is seen that reducing the high altitude limit on $q\alpha_c$ reduces the maximum value of $q\alpha$ but also increases the error in dynamic pressure at staging in some cases. Tables 7-4b shows that there is no $q\alpha$ problem when the thrust gradient is 5%.

Table 7-4b. Effects of Qα limits for 5% thrust gradient.

Qα Limits	Wind Direction	Max. Qα and (Time of Occurrence)		Q_{err}
10 k	Tail	5,096	(38.07)	-8.22
	Head	7,315	(27.87)	1.77
10 k for H ≤ 25 k 5 k for H > 25 k	Tail	5,096	(38.07)	-8.22
	Head	6,797	(27.87)	12.79

It was decided not to reduce the high altitude limit on $q\alpha_c$ because of its adverse effects on the dynamic pressure error and because the parceling out of the steering command described later in this chapter reduces the maximum qα below the design limit for the extreme case of the 10% thrust gradient.

7.2.2 Selection of $COUNT_{delay}$ Value

The effects on predictive steering performances of using different $COUNT_{delay}$ values of 0, 2, and 4 are shown in Table 7-5. N_{steer} is kept at the value selected above of $N_{steer} = 25$.

$COUNT_{delay}$ does not seem to have much effect on performance. It was decided to use $COUNT_{delay} = 2$ in evaluating the capabilities of predictive steering. This value of $COUNT_{delay}$ seems adequate for the throughput capabilities of present computers.

7.3 Selection of Steering Command Update Option

In this section the options are investigated of utilizing the corrections in commanded flight path angle generated periodically by predictive simulations by (1) abruptly introducing the full values of the correction at the update time (2) or parceling out the correction between predictive update times. The effects of these update methods are compared in Table 7-6.

Table 7-5. $COUNT_{delay}$ studies.

$Count_{delay}$	Flight Conditions	Max. $Q\alpha$ and (Time of Occurrence)		Q_{err}
0	A	6,842	(35.69)	-10.80
0	B	12,808	(25.75)	5.16
2	A	6,433	(35.89)	-10.90
2	B	12,998	(25.92)	5.50
4	A	6,556	(36.09)	-10.56
4	B	13,110	(26.10)	6.62

Flight Condition
A. 90° Launch, Nominal Thrust, No Wind
B. 90° Launch, 10% Thrust Gradient, Head Wind

Table 7-6. γ_c update option studies.

Update Option	Flight Conditions	Max. $Q\alpha$ and (Time of Occurrence)		Q_{err}
1	A	6,433	(35.89)	-10.90
1	B	9,593	(35.91)	-5.33
1	C	12,998	(25.92)	5.50
2	A	3,730	(37.65)	-9.76
2	B	5,864	(15.23)	-4.03
2	C	10,210	(34.06)	9.40

Flight Condition
A. 90° Launch, Nominal Thrust, No Wind
B. 118° Launch, Nominal Thrust, Head Wind
C. 90° Launch, 10% Thrust Gradient, Head Wind

Option 2 meets end conditions better than Option 1 and results in a significant reduction in the maximum dynamic pressure encountered because the changes in γ_c are smoothed out causing less severe changes in α_c. Therefore, Option 2 was selected for all subsequent simulation runs.

7.4 Compensations for Altitude Deviations

In this section the possibility is investigated of correcting the gamma command every steering cycle for the vehicle's deviations in altitude from the desired trajectory. As an initial test the following computations were added to the predictive steering performed at 12 and 31 seconds: The current altitude was perturbed by ΔH_{trial} and 1) the predicted flight path angle γ_{simA} is used and the vehicle is simulated till burnout 2) γ_{simA} is compensated by $K_H \Delta H_{trial}$ (where K_H is based on Eq. (3.3)) and the vehicle is simulated till burnout. The results are listed in Table 7-7 .

Table 7-7. Height compensation studies I.

γ Value Used for Prediction	Q_{err}	
	T = 12 s	T = 32 s
$\gamma_{sim\ A}$	-6.57	-5.56
Adjusted $\gamma_{sim\ A}$	-0.71	0.38
% Improvement	89%	93%

In this table it is seen that compensating for altitude increases the end condition accuracy by 89% at 12 seconds and by 93% at 31 sec.

The altitude compensation option was implemented in the vehicle simulation as described in section 3.3.3 and was evaluated. The results are listed in Table 7-8.

Table 7-8. Height compensation studies II.

Height Compensation	Flight Conditions	Max. $Q\alpha$ and (Time of Occurrence)		Q_{err}
No	A	3,730	(37.65)	-9.76
No	B	5,864	(15.23)	-4.03
No	C	10,210	(34.06)	9.40
Yes	A	4,371	(37.58)	-10.29
Yes	B	5,886	(15.22)	-4.07
Yes	C	10,259	(33.95)	9.69

Flight Conditions

A. 90° Launch, Nominal Thrust, No Wind
B. 118° Launch, Nominal Thrust, Head Wind
C. 90° Launch, 10% Thrust Gradient, Head Wind

Table 7-8 shows that the altitude compensation algorithm does not improve the performance of the vehicle when actually incorporated into the predictive steering. The reason that these results contradict the initial tests performed above could be attributed to the fact that the vehicle trajectory is continually perturbed from its reference trajectory and it is difficult for the vehicle to keep up with these changes. It was therefore decided not to employ altitude compensation in subsequent simulations of the predictive steering.

7.5 Nominal Predictive Steering Performance

Using the parameters and features selected above, a predictive steering simulation was made, producing the plots shown in Figure 7-1. The plot of $q\alpha$ is particularly significant because of the large excursions in $q\alpha$ that occur throughout the boost phase. These excursions are much larger and more numerous than those seen in the simulation plot for logarithmic steering presented in Figure 5-6. The primary cause of the $q\alpha$ excursions was found to be small errors in the estimated values of thrust.

7.6 Sensitivity of Predictive Steering to Thrust Estimation Errors

Three simulation runs were made to demonstrate how the $q\alpha$ excursions are limited to errors in estimated thrust. First, in Figure 7-2 the actual values of thrust and mass were used in lieu of estimated values in a repeat of the nominal simulation runs shown in Figure 7-1. The $q\alpha$ excursions for this case are much smaller than those in Figure 7-1, and they diminish toward the end of the boost phase. The fact that the use of actual thrust and mass values significantly reduced the persistent $q\alpha$ excursions demonstrates that these excursions are caused to a major extent by errors in either the estimated mass or the estimated thrust, or both. Since the maximum error in mass was only 0.035 percent in the original nominal run, it was concluded that the errors in estimated thrust that ranged up to several tenths of a percent in the latter portion of boost were the more probable cause of the $q\alpha$ excursions. Therefore, a second simulation of the nominal case was made using (1) actual mass throughout the run, (2) actual thrust for $t \leq 24.7$ seconds and (3) the estimated thrust values from the original nominal simulation for $t > 24.7$ seconds. The plots from this run are shown in Figure 7-3, where it is seen that the $q\alpha$ excursions for $t > 24.7$ sec, where original thrust estimations were used, are very similar to those shown in Figures 7-1. It should be further noted that the oscillations in α corresponding to successive $q\alpha$ excursions seemed to be roughly correlated to changes in the polarity of the error in the estimated vacuum thrust, which occurred roughly every two predictive steering cycles in this particular case. However, it was theorized that even a constant bias in estimated thrust might be able to produce $q\alpha$ excursions, and third simulation run was made to demonstrate this possiblity. In this run, based on the same environment as Figure 7-1, the predictive steering employed (1) actual mass values and (2) actual thrust values for $t \leq 14$ seconds and (3) thrust values that were one percent higher than the actual values for $t > 14$ seconds. The plot for this run is presented in Figure 7-4. It is seen that substantial excursions in $q\alpha$ occur throughout the boost phase.

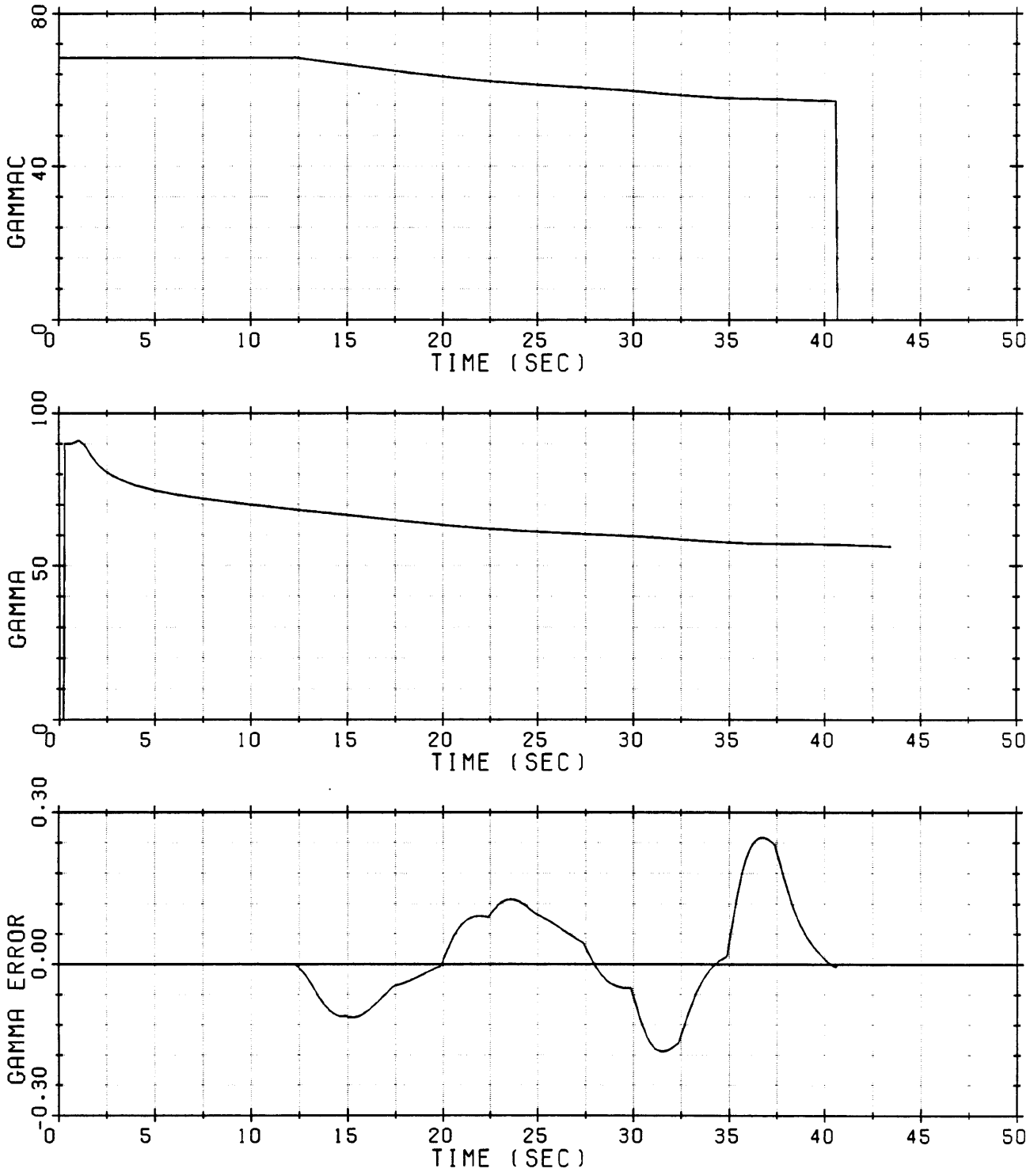

Figure 7-1. Predictive steering performance under nominal conditions using estimated values of thrust and mass.

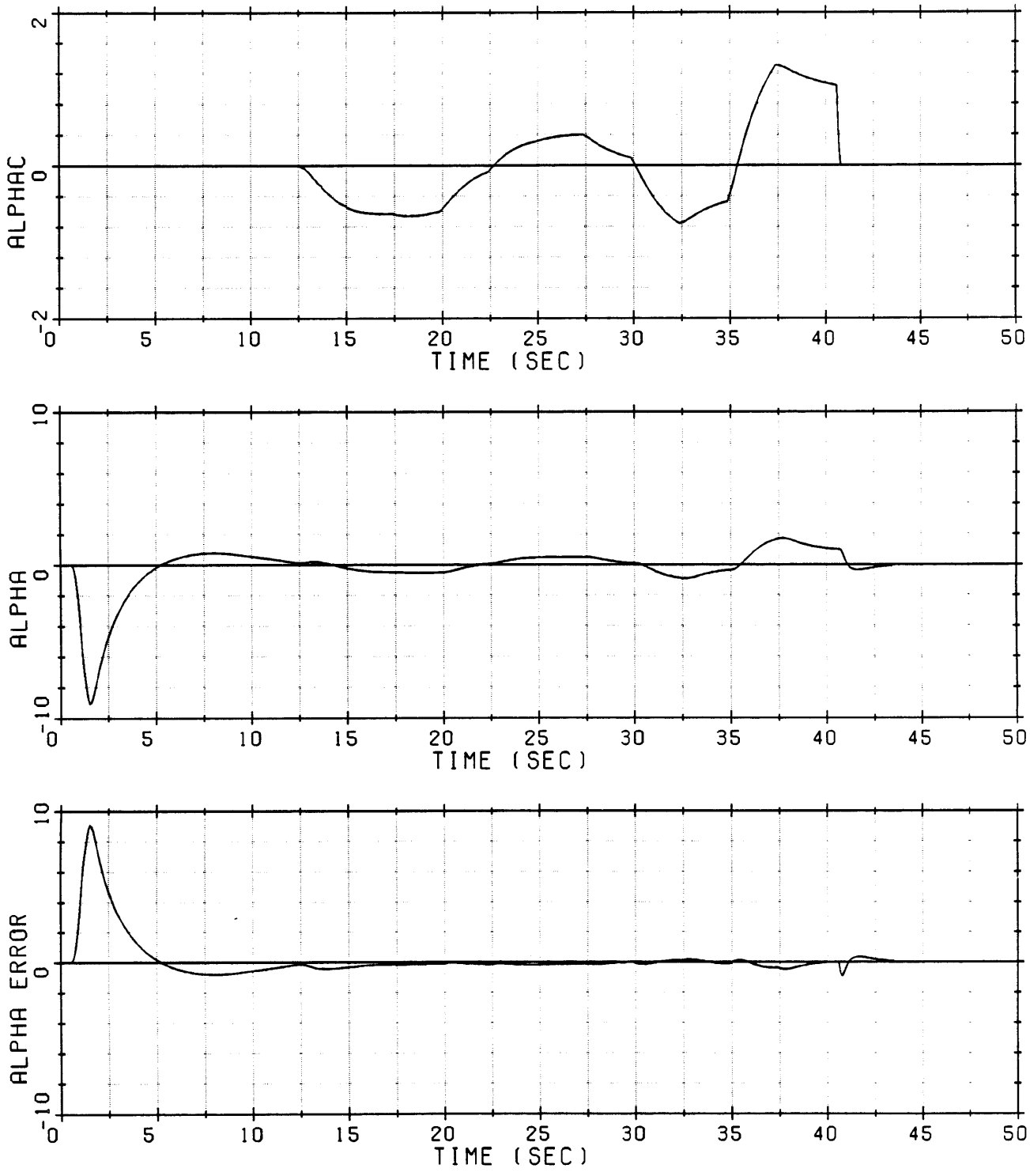

Figure 7-1. Predictive steering performance under nominal conditions using estimated values of thrust and mass. (Cont.)

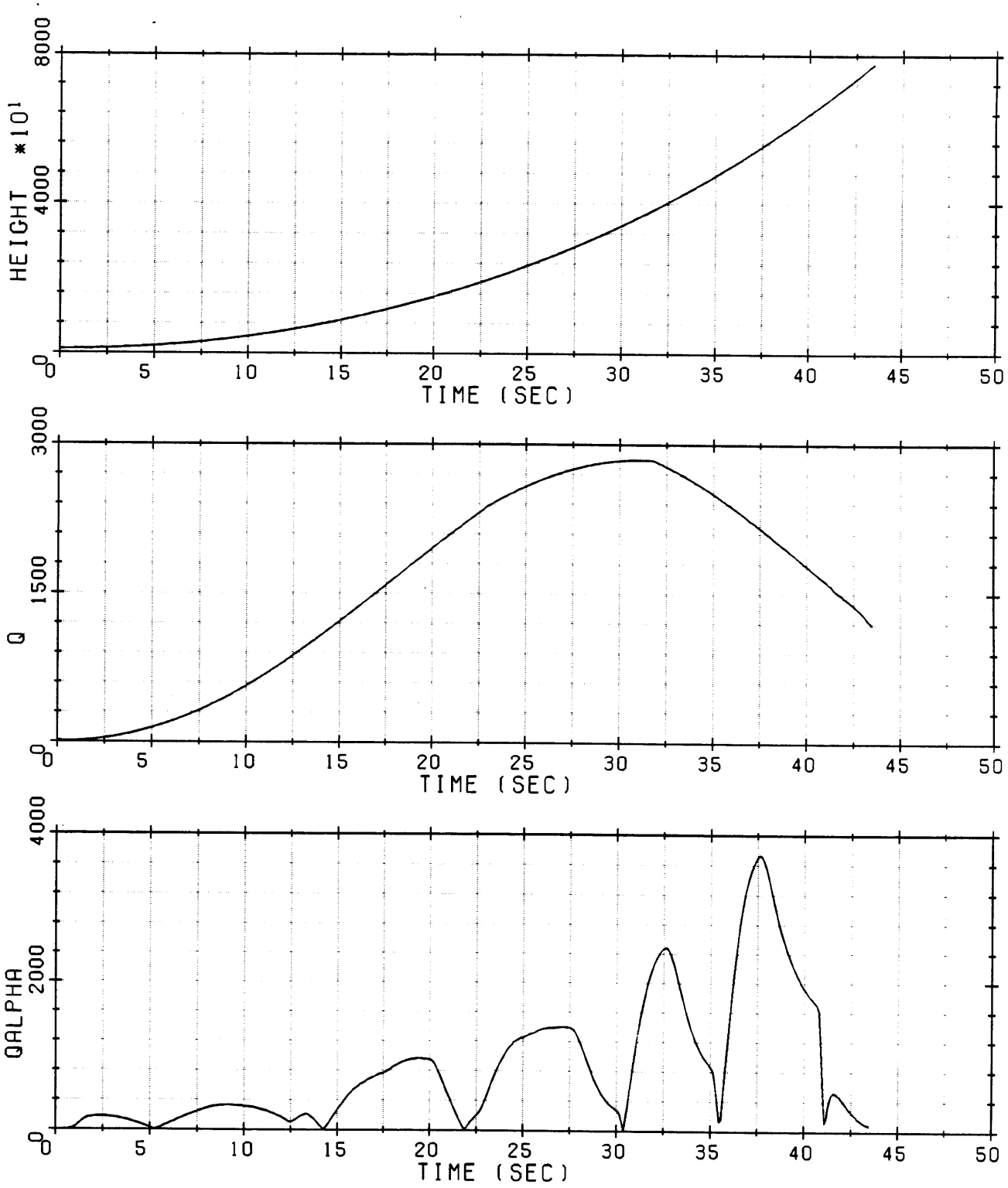

Figure 7-1. Predictive steering performance under nominal conditions using estimated values of thrust and mass. (Cont.)

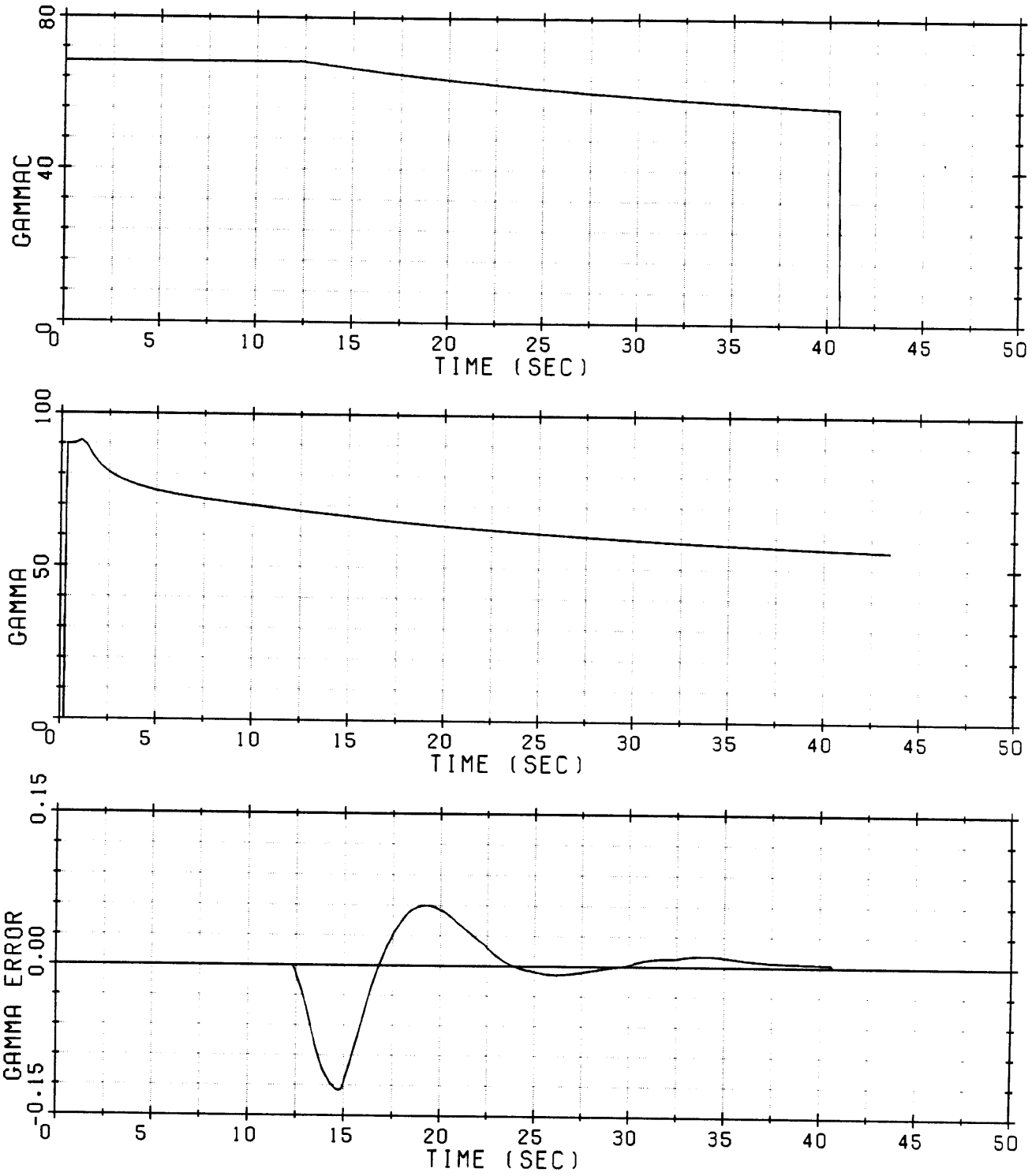

Figure 7-2. Predictive steering performance under nominal conditions using actual values of thrust and mass.

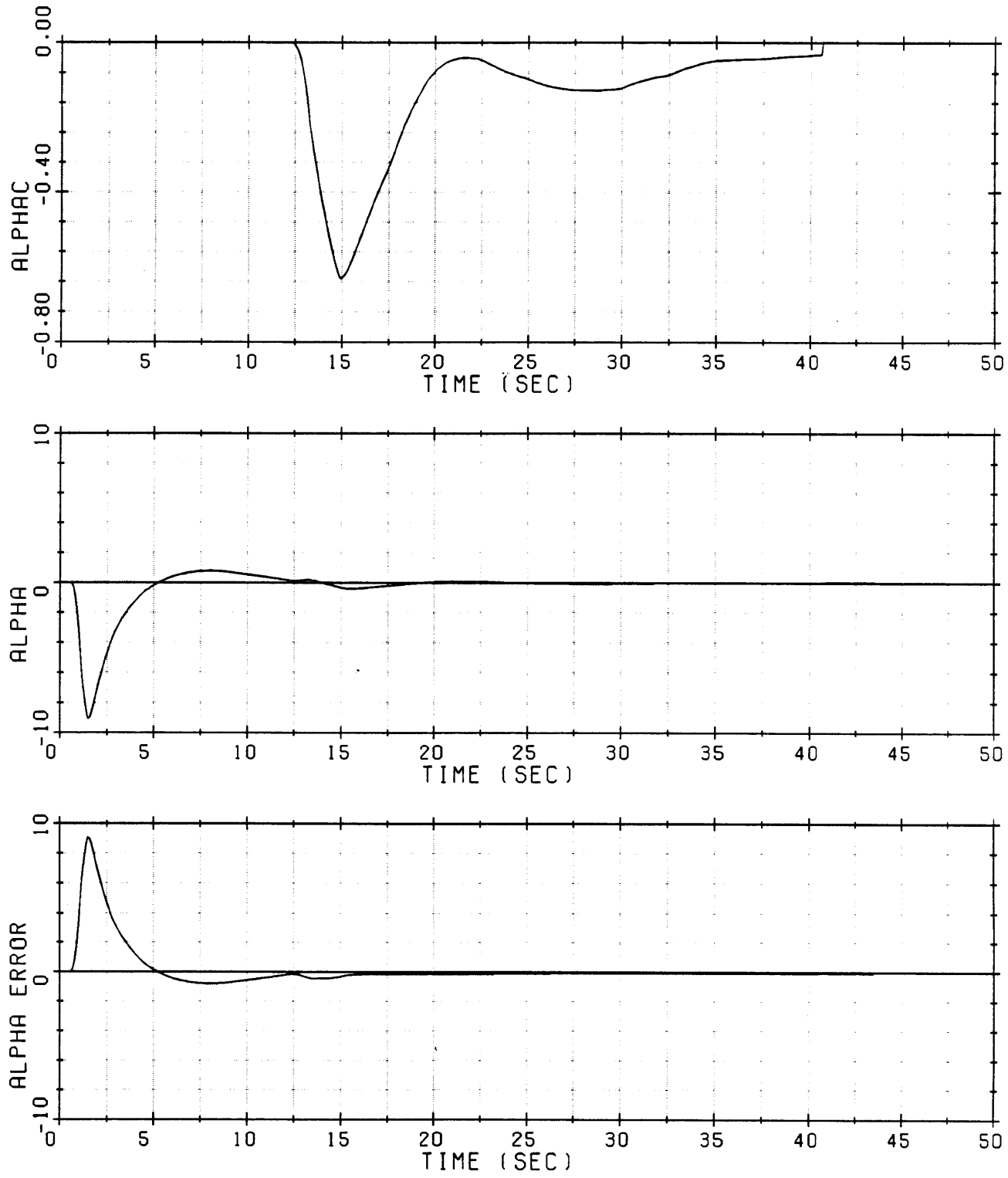

Figure 7-2. Predictive steering performance under nominal conditions using actual values of thrust and mass. (Cont.)

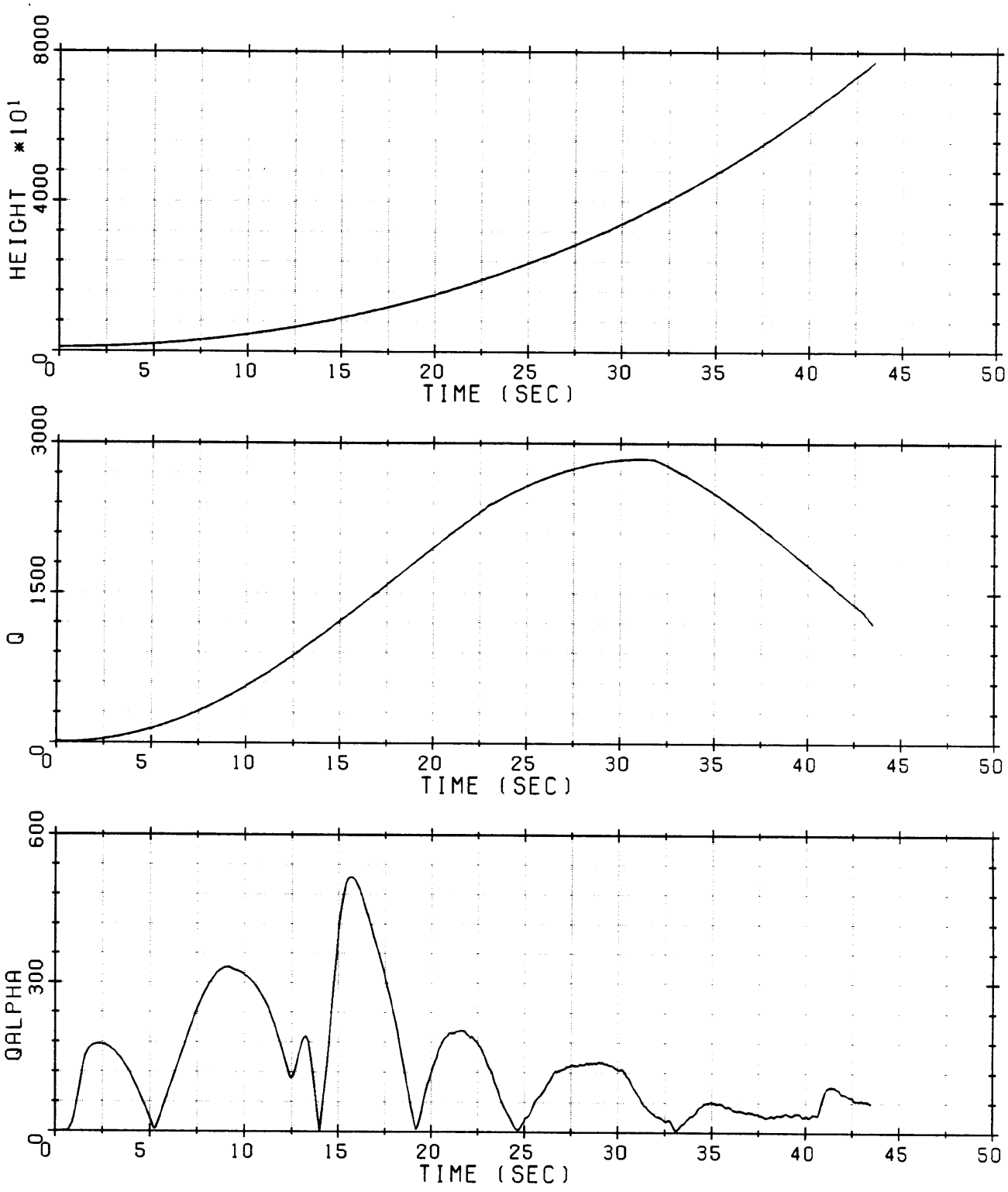

Figure 7-2. Predictive steering performance under nominal conditions using actual values of thrust and mass. (Cont.)

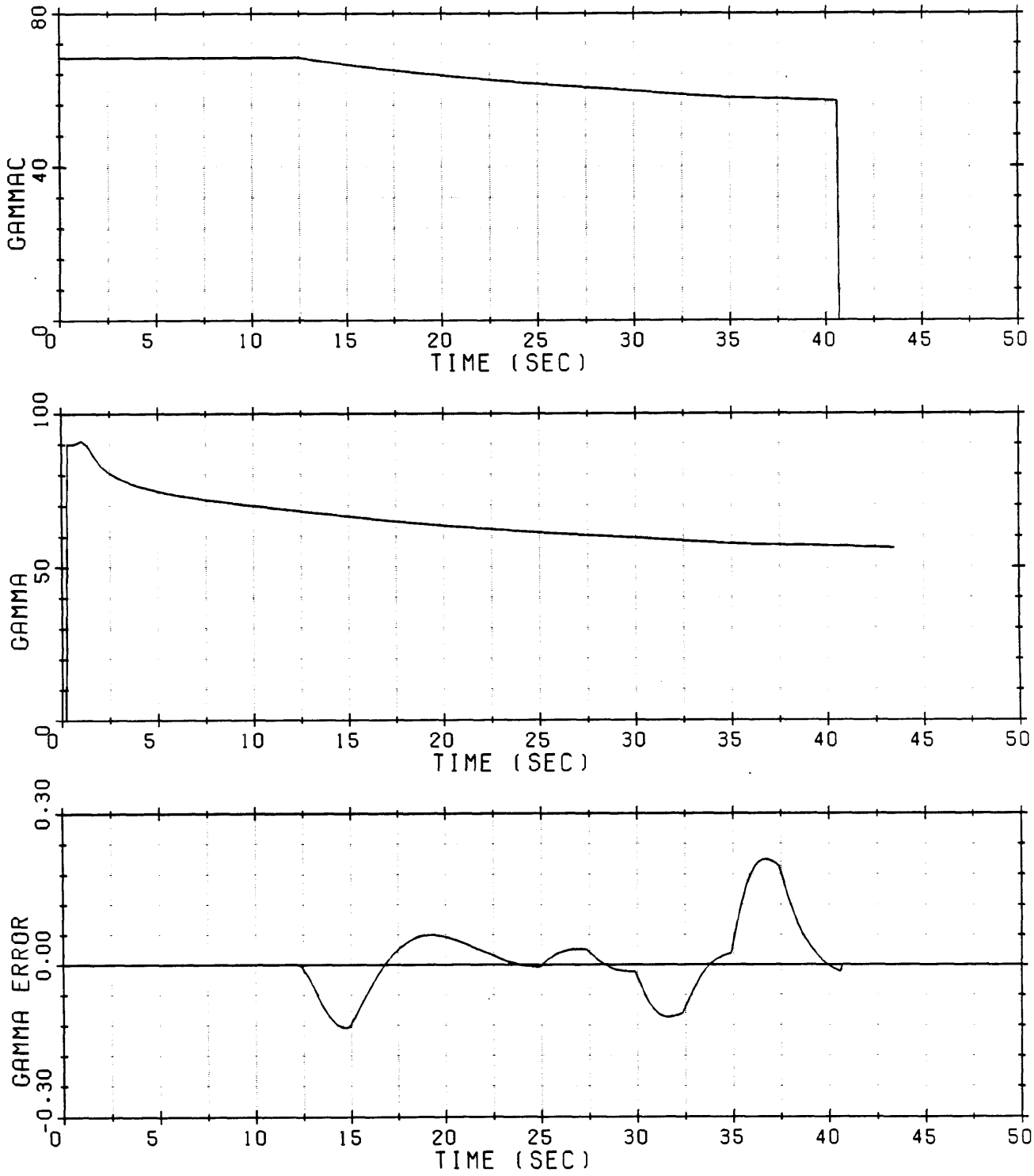

Figure 7-3. Predictive steering performance under nominal conditions using zero estimate errors for $t \leq 24.7$ s and same thrust estimate error as Figure 7-1 for $t > 24.7$ s.

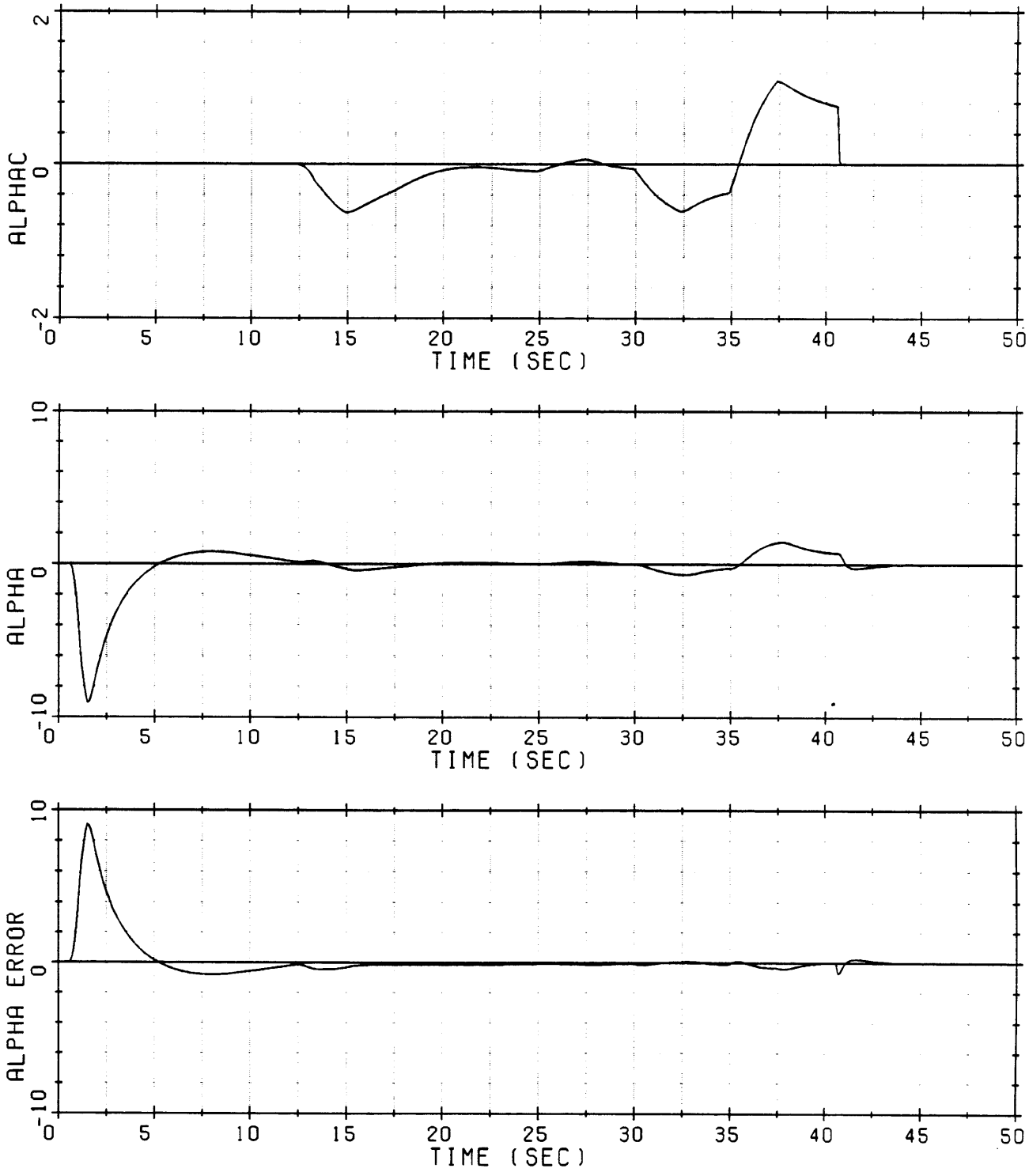

Figure 7-3. Predictive steering performance under nominal conditions using zero estimate errors for $t \leq 24.7$ s and same thrust estimate error as Figure 7-1 for $t > 24.7$ s. (Cont.)

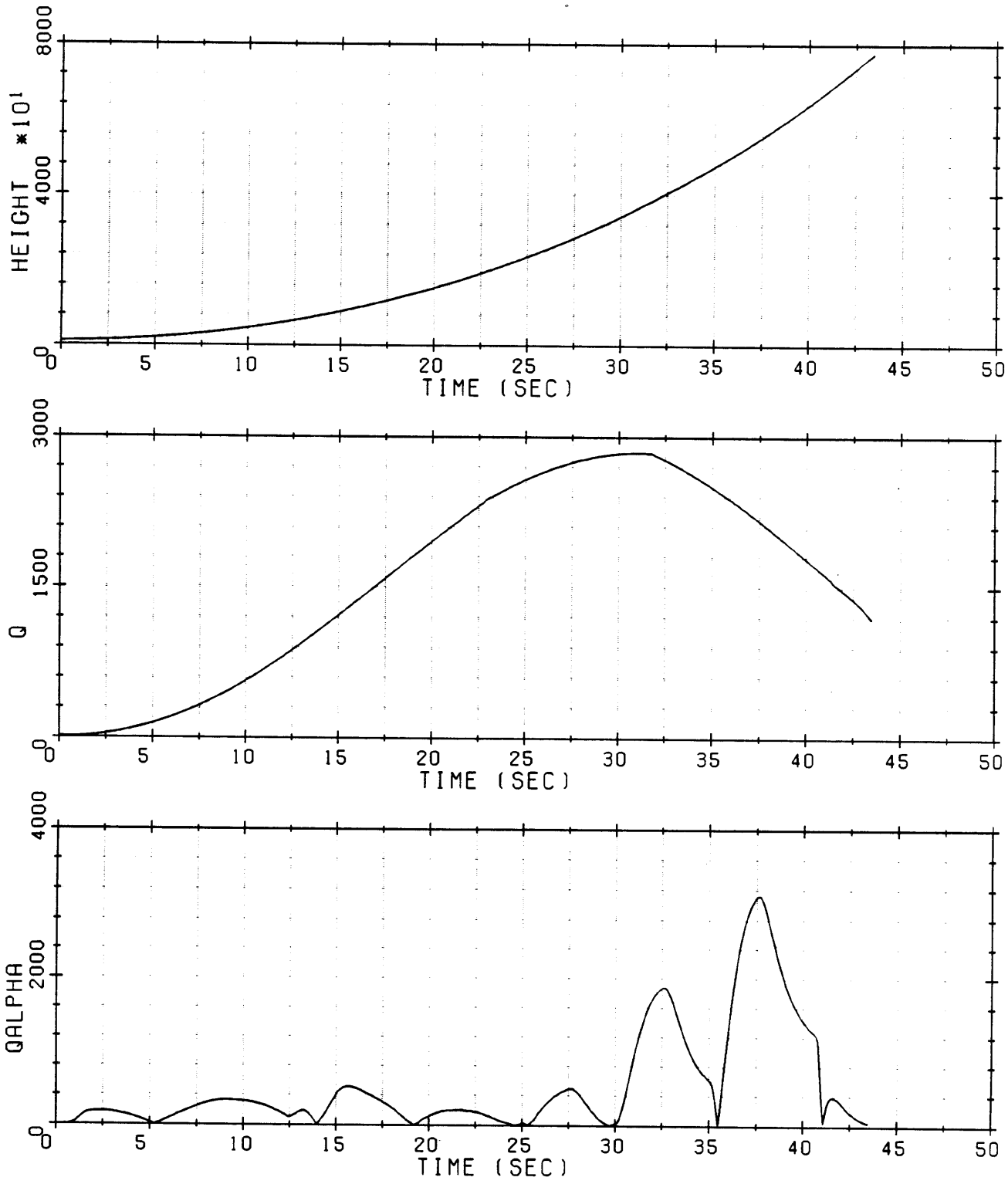

Figure 7-3. Predictive steering performance under nominal conditions using zero estimate errors for $t \leq 24.7$ s and same thrust estimate error as Figure 7-1 for $t > 24.7$ s. (Cont.)

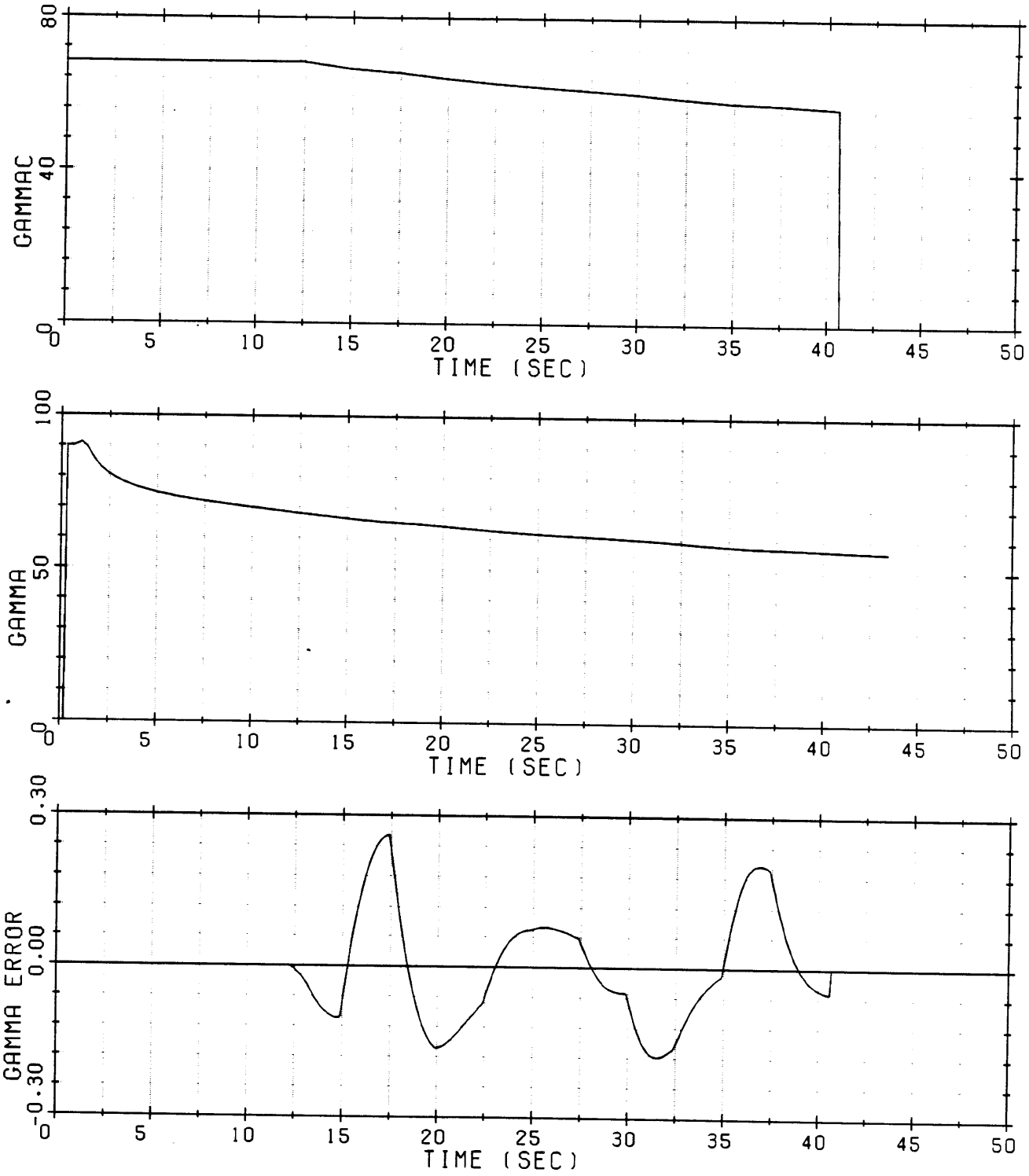

Figure 7-4. Predictive steering performance under nominal conditions using a constant error of 1% in estimated thrust for $T > 14$ s and zero error for $T \leq 14$ s.

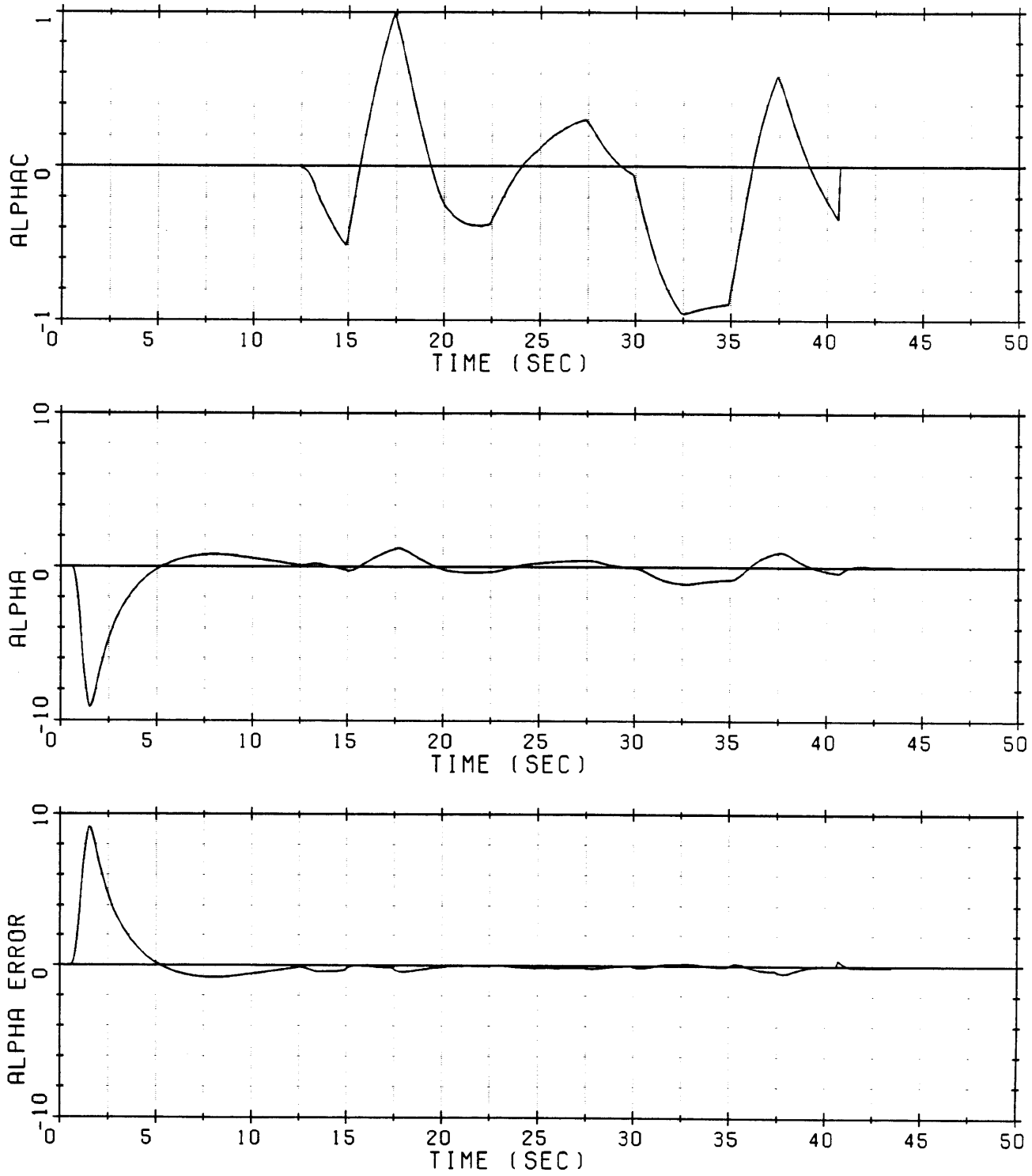

Figure 7-4. Predictive steering performance under nominal conditions using a constant error of 1% in estimated thrust for $T > 14$ s and zero error for $T \leq 14$ s. (Cont.)

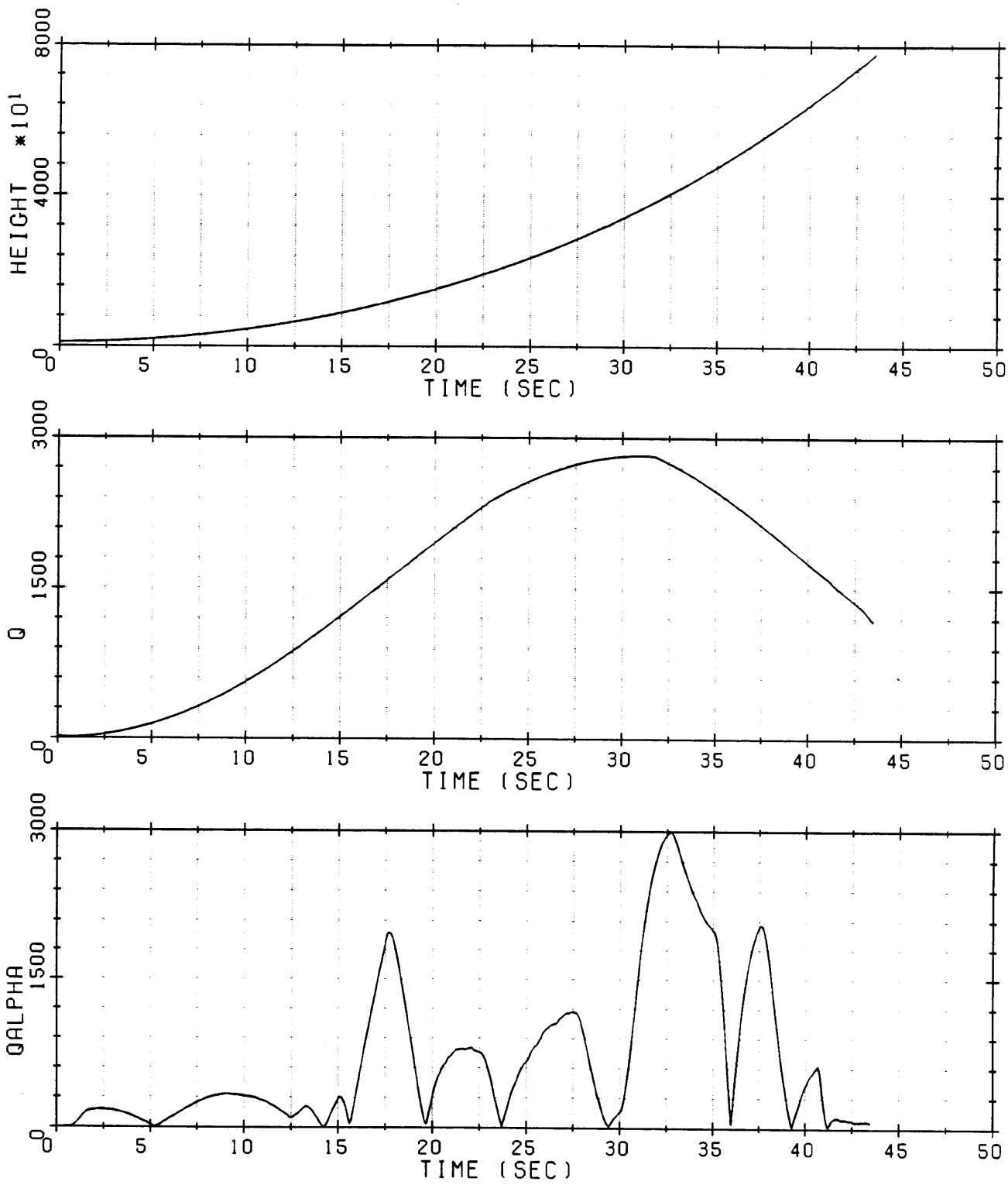

Figure 7-4. Predictive steering performance under nominal conditions using a constant error of 1% in estimated thrust for $T > 14$ s and zero error for $T \leq 14$ s. (Cont.)

It appears to be possible to modify the predictive steering to reduce its sensitivity to thrust estimation errors, and it appears to be possible to improve the thrust-mass estimator design to reduce these errors. These revisions, which are suggested for future study in Chapter 8 of this thesis would all reduce the undesirable excursions in $q\alpha$.

7.7 Combination of Parceling Out Gamma and Reducing the Frequency of Predictive Updates

Just as the parceling out of the commanded gamma was found to decrease the maximum $q\alpha$ in Section 7.3, so also was the increasing of the predictive steering update time found to decrease the maximum $q\alpha$ without the parceling of gamma in Section 7.2.1 . It was therefore decided to investigate whether an increase in the update time in combination with the parceling out of gamma would further reduce the maximum $q\alpha$. Accordingly, the predictive steering based on parceling out gamma was simulated for an increased N_{steer} = 100 for comparison with the results obtained with the same steering for N_{steer} = 25. This simulated comparison was made for two cases: (1) nominal constant thrust with a head wind and (2) 10% thrust gradient with no wind. The results are discussed below.

(1) Constant Thrust, Head Wind Case

Plots obtained with N_{steer} values of 25 and 100 for the constant thrust, head wind case are presented in Figures 7-5 and 7-6, respectively. These plots show that the maximum $q\alpha$ is reduced from 5020 to 4062 deg lb/ft^2 by increasing the update time. This reduction was obtained at the expense of a slight change in terminal dynamic pressure error from -3.78 to 9.82 psf.

(2) 10% Thrust Gradient Case

Plots obtained with N_{steer} values of 25 and 100 for the 10% thrust gradient case are presented in Figures 7-7 and 7-8, respectively. These plots show a decrease in maximum $q\alpha$ from

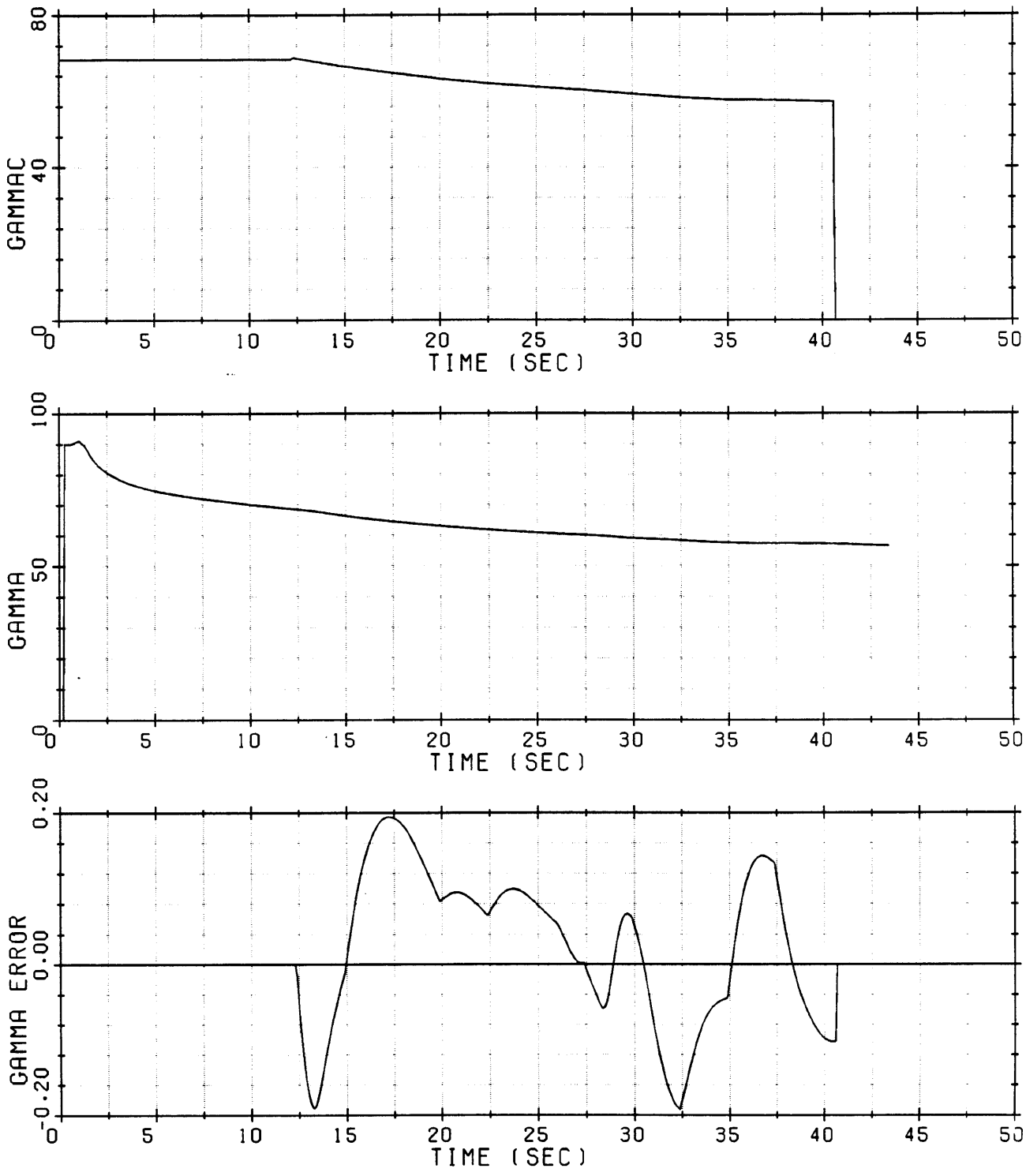

Figure 7-5. Predictive steering performance under a head wind with $N_{steer} = 25$.

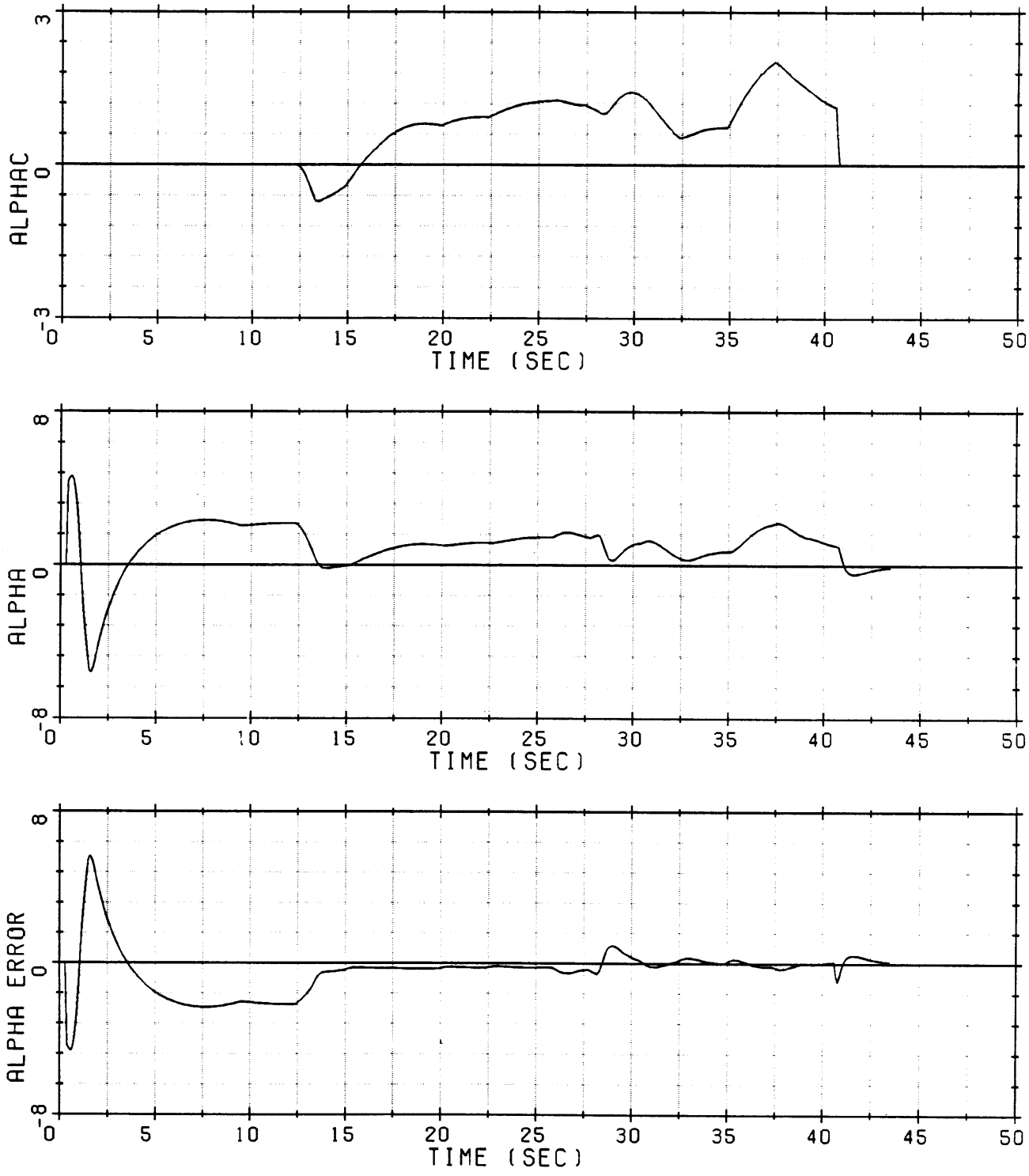

Figure 7-5. Predictive steering performance under a head wind with N_{steer} = 25. (Cont.)

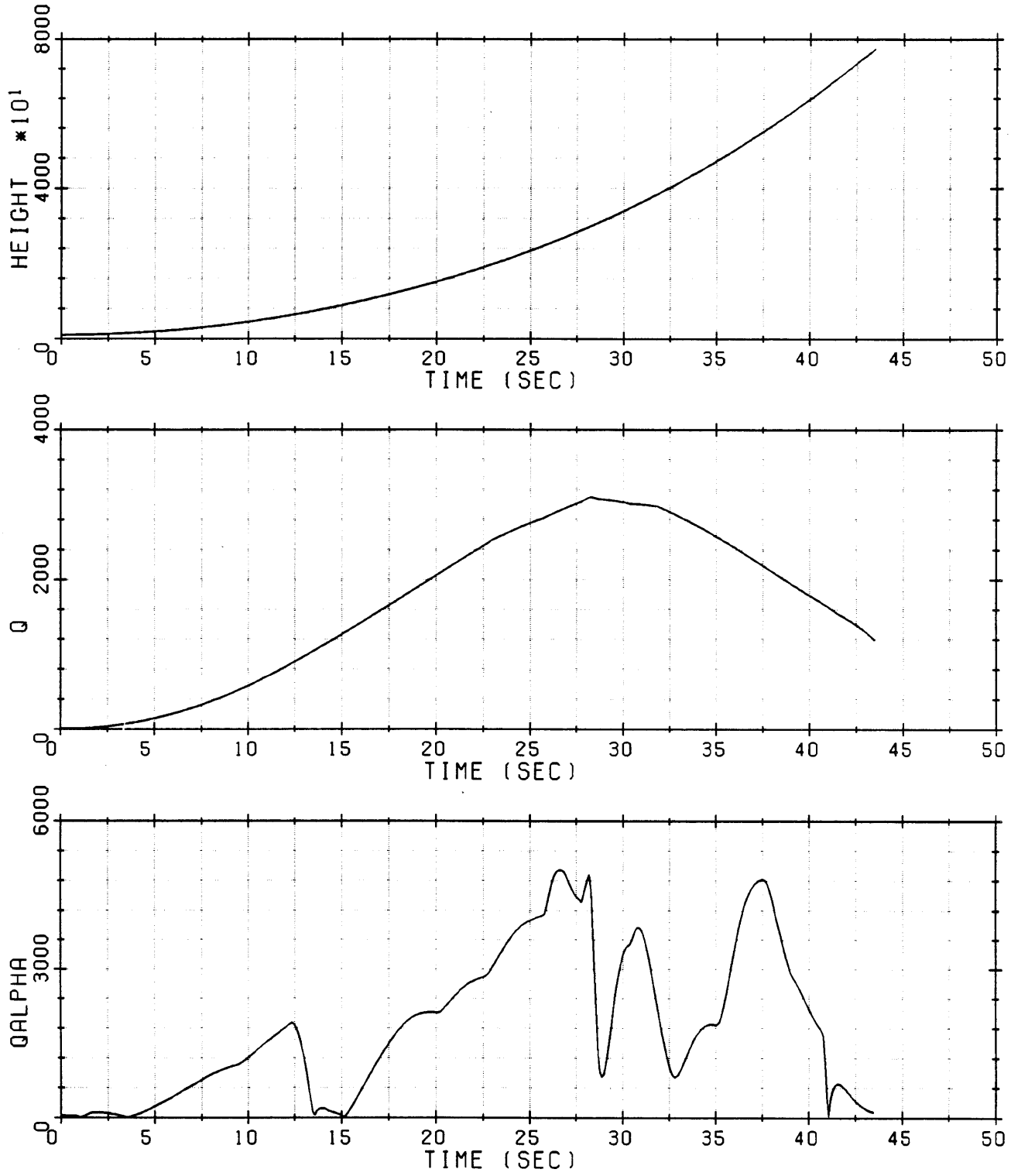

Figure 7-5. Predictive steering performance under a head wind with N_{steer} = 25. (Cont.)

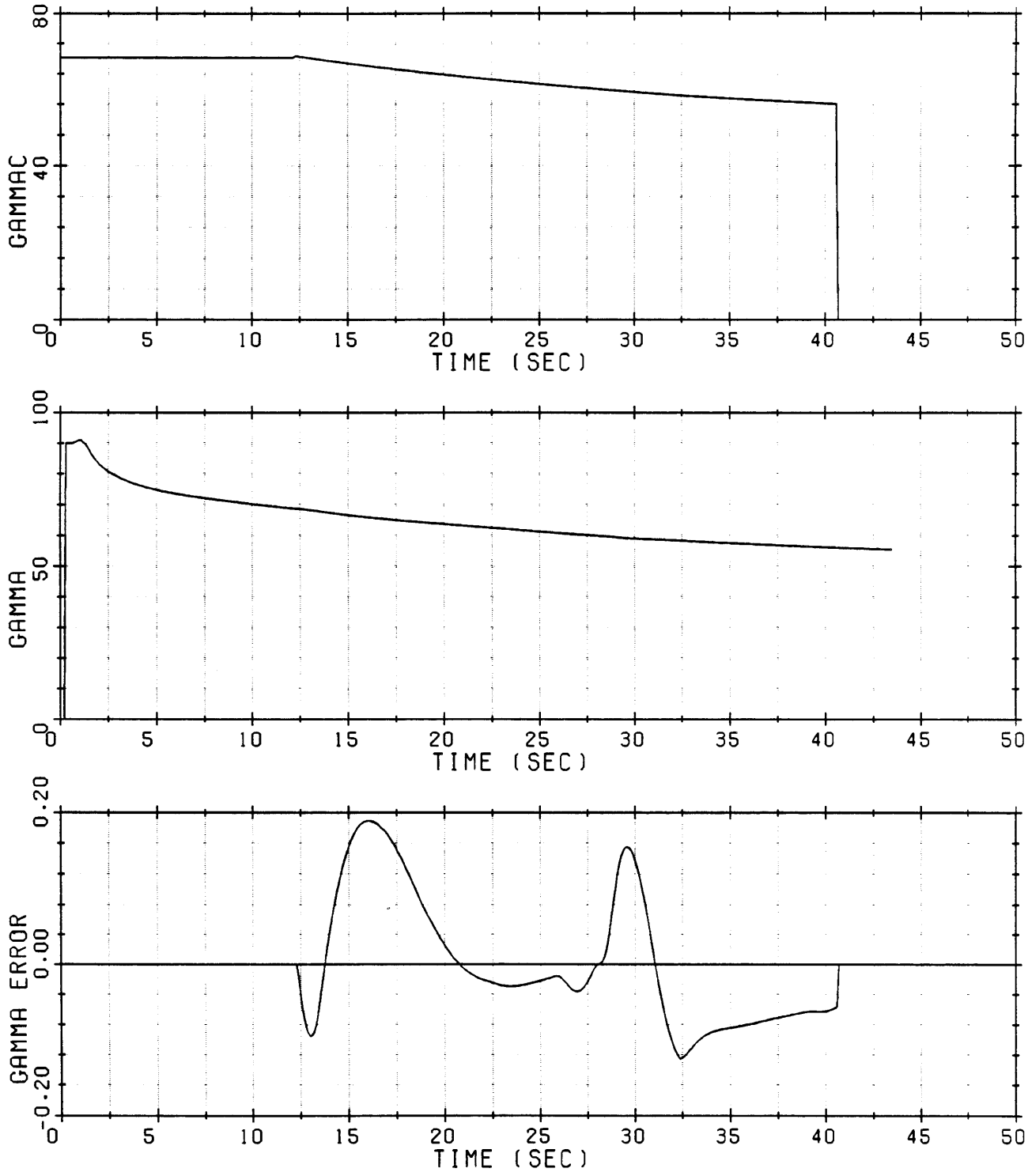

Figure 7-6. Predictive steering performance under a head wind with N_{steer} = 100.

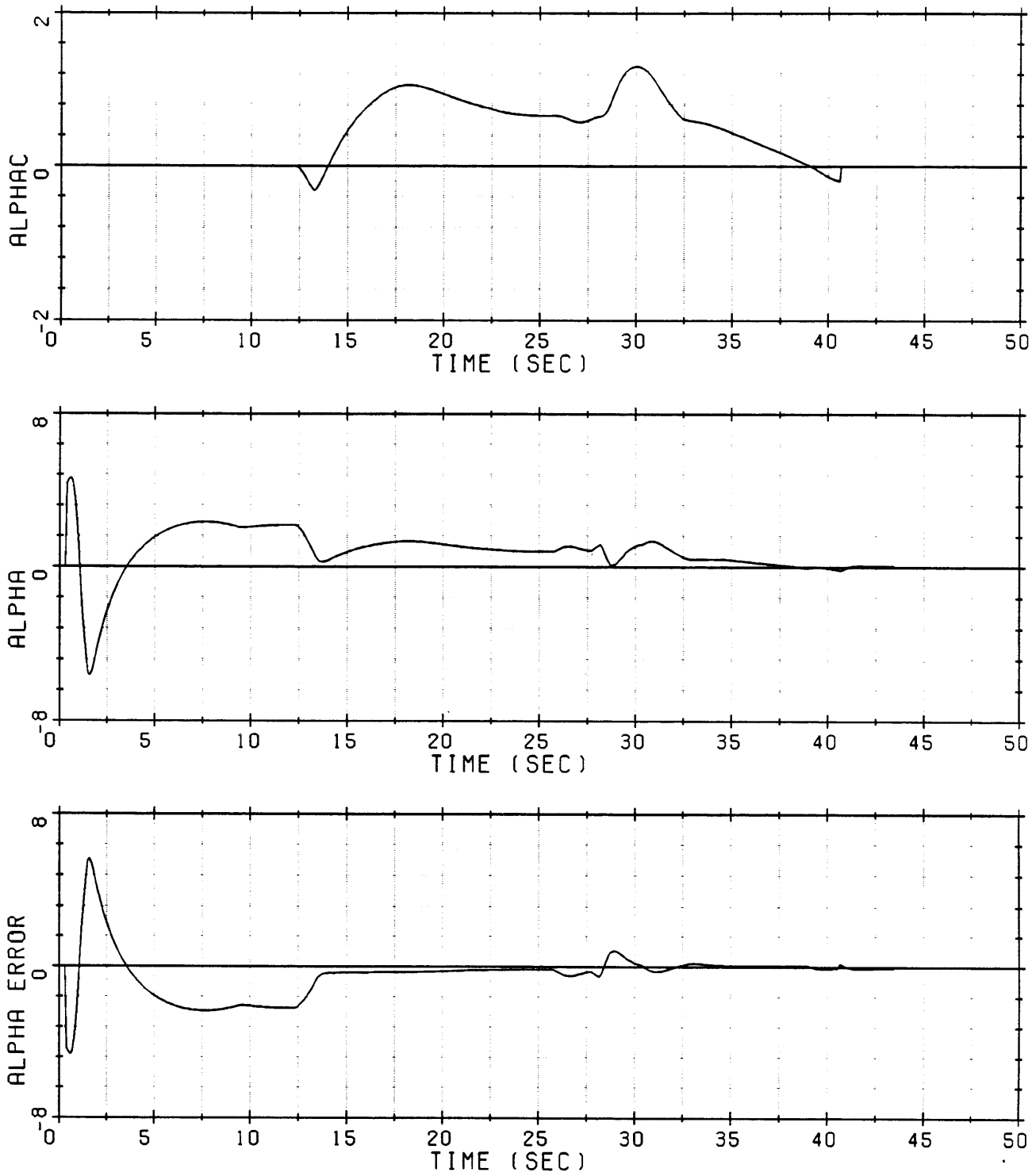

Figure 7-6. Predictive steering performance under a head wind with N_{steer} = 100. (Cont.)

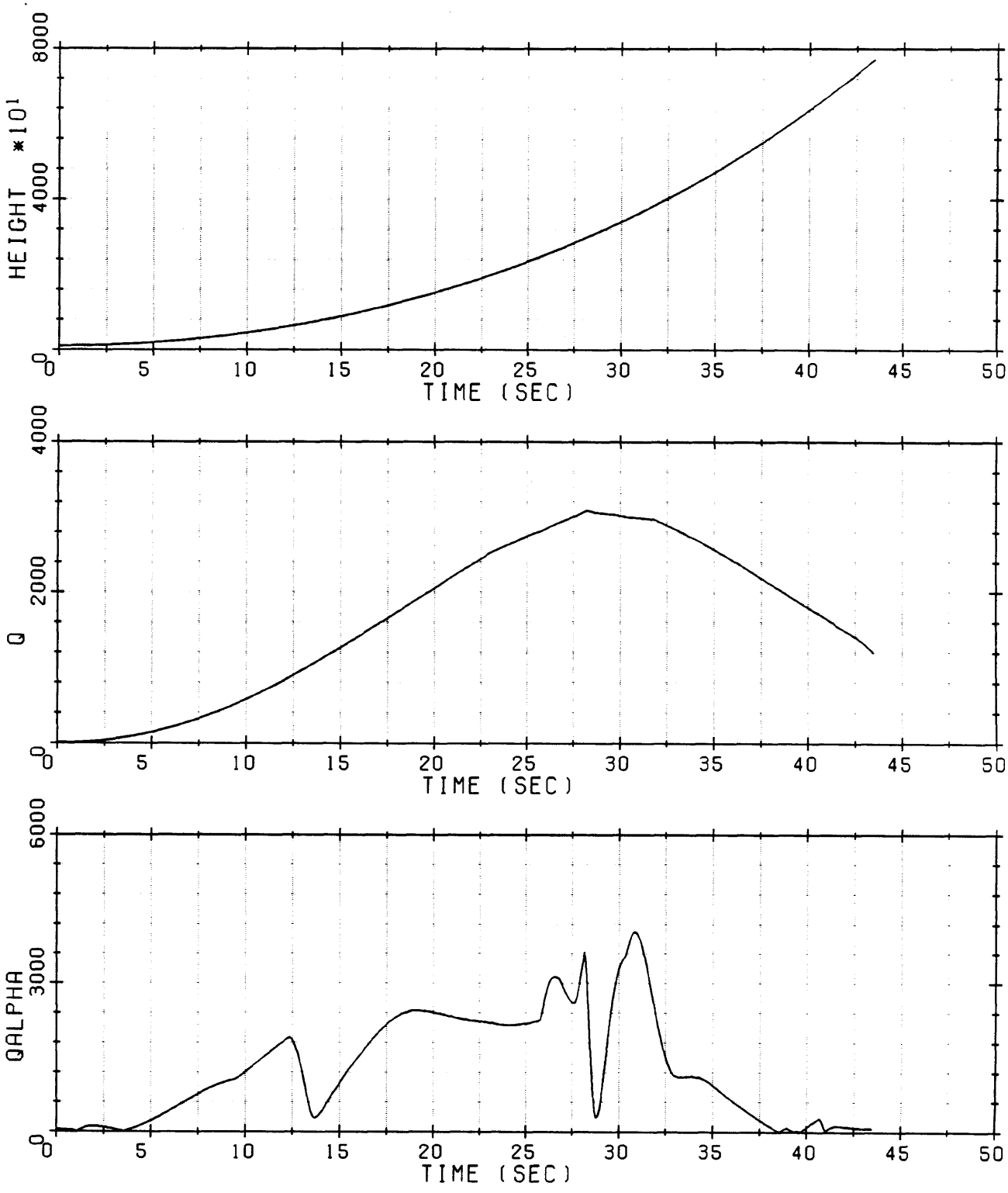

Figure 7-6. Predictive steering performance under a head wind with N_{steer} = 100. (Cont.)

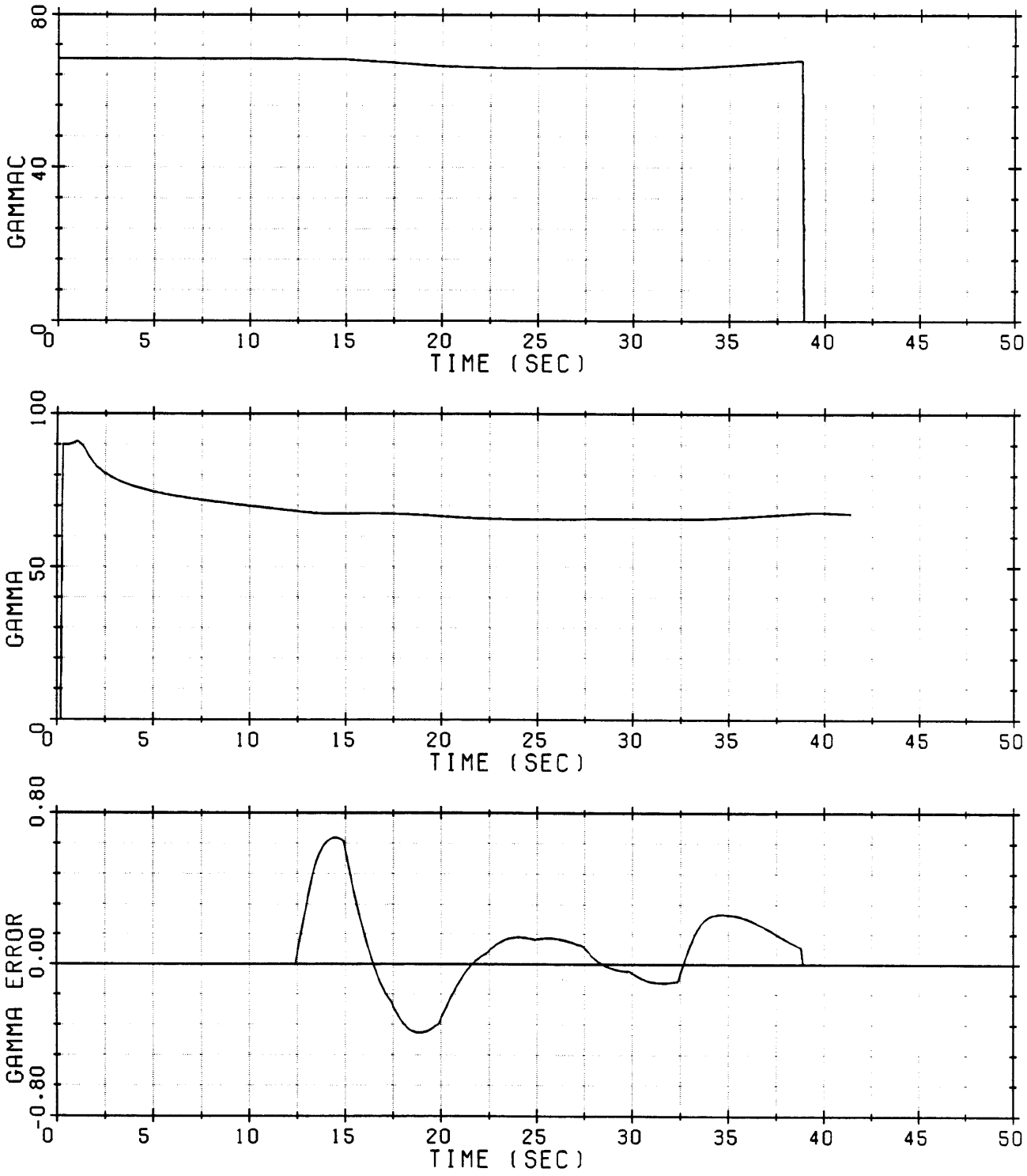

Figure 7-7. Predictive steering performance under a 10% thrust gradient with N_{steer} = 25.

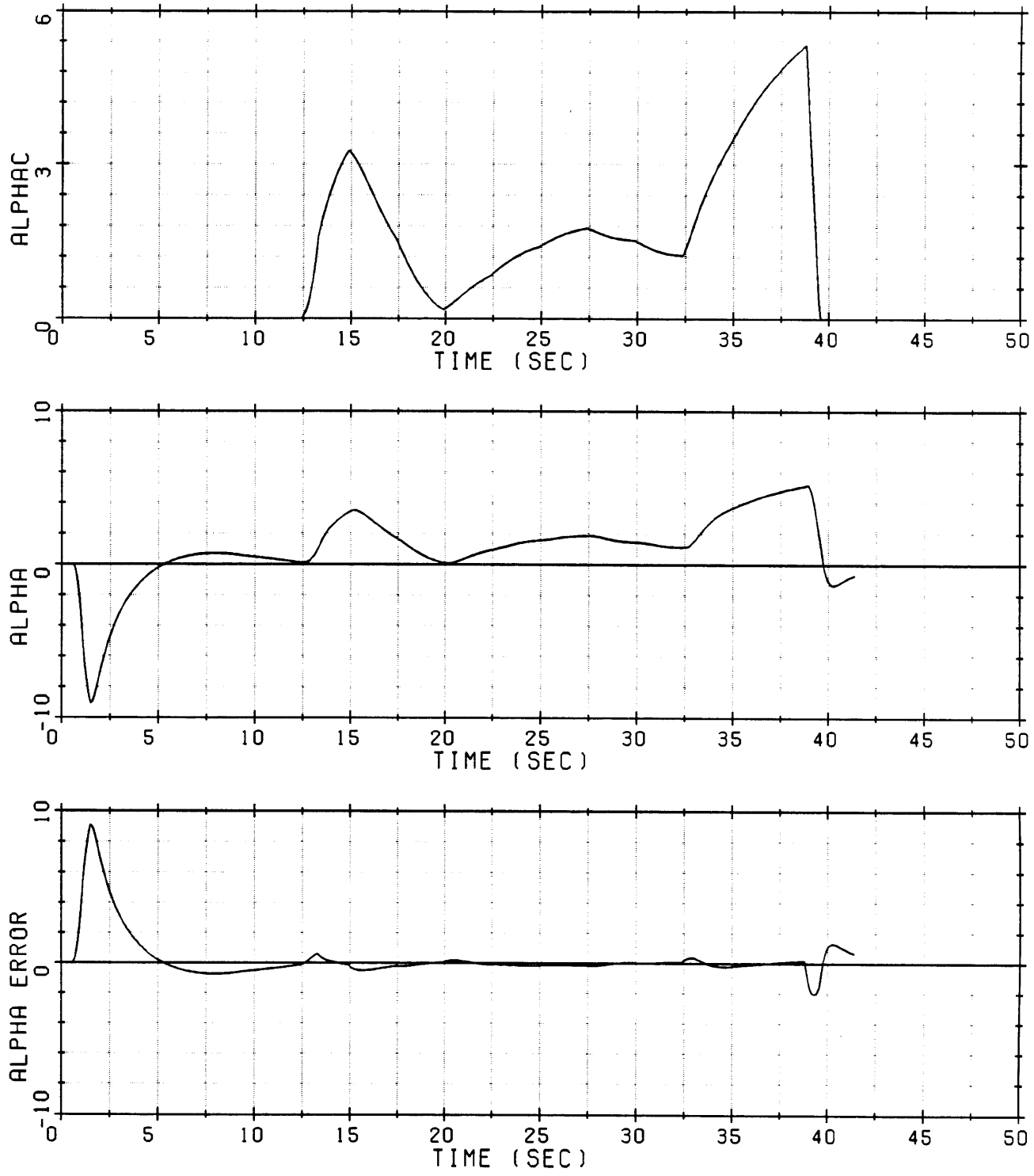

Figure 7-7. Predictive steering performance under a 10% thrust gradient with N_{steer} = 25. (Cont.)

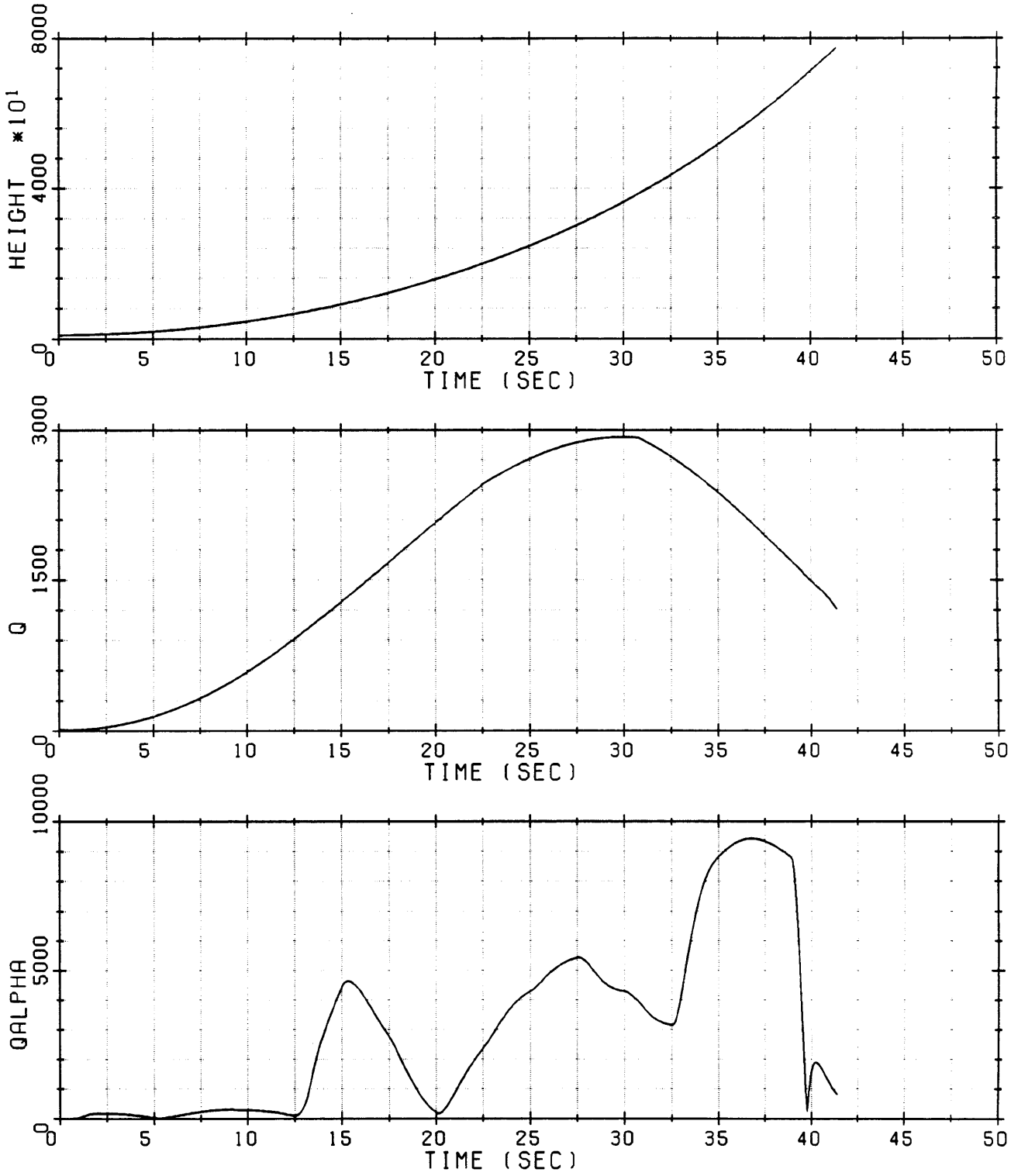

Figure 7-7. Predictive steering performance under a 10% thrust gradient with N_{steer} = 25. (Cont.)

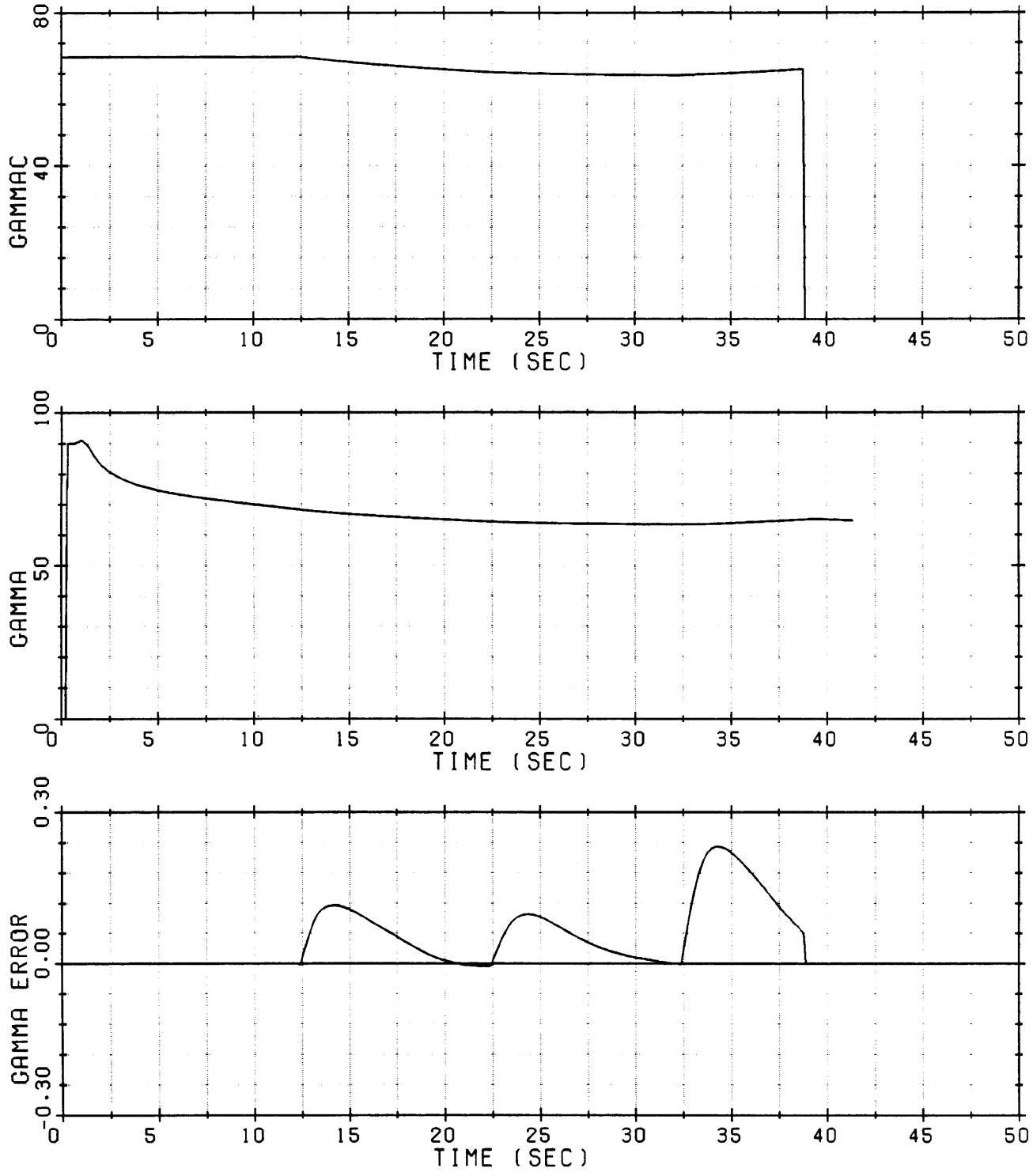

Figure 7-8. Predictive steering performance under a 10% thrust gradient with N_{steer} = 100.

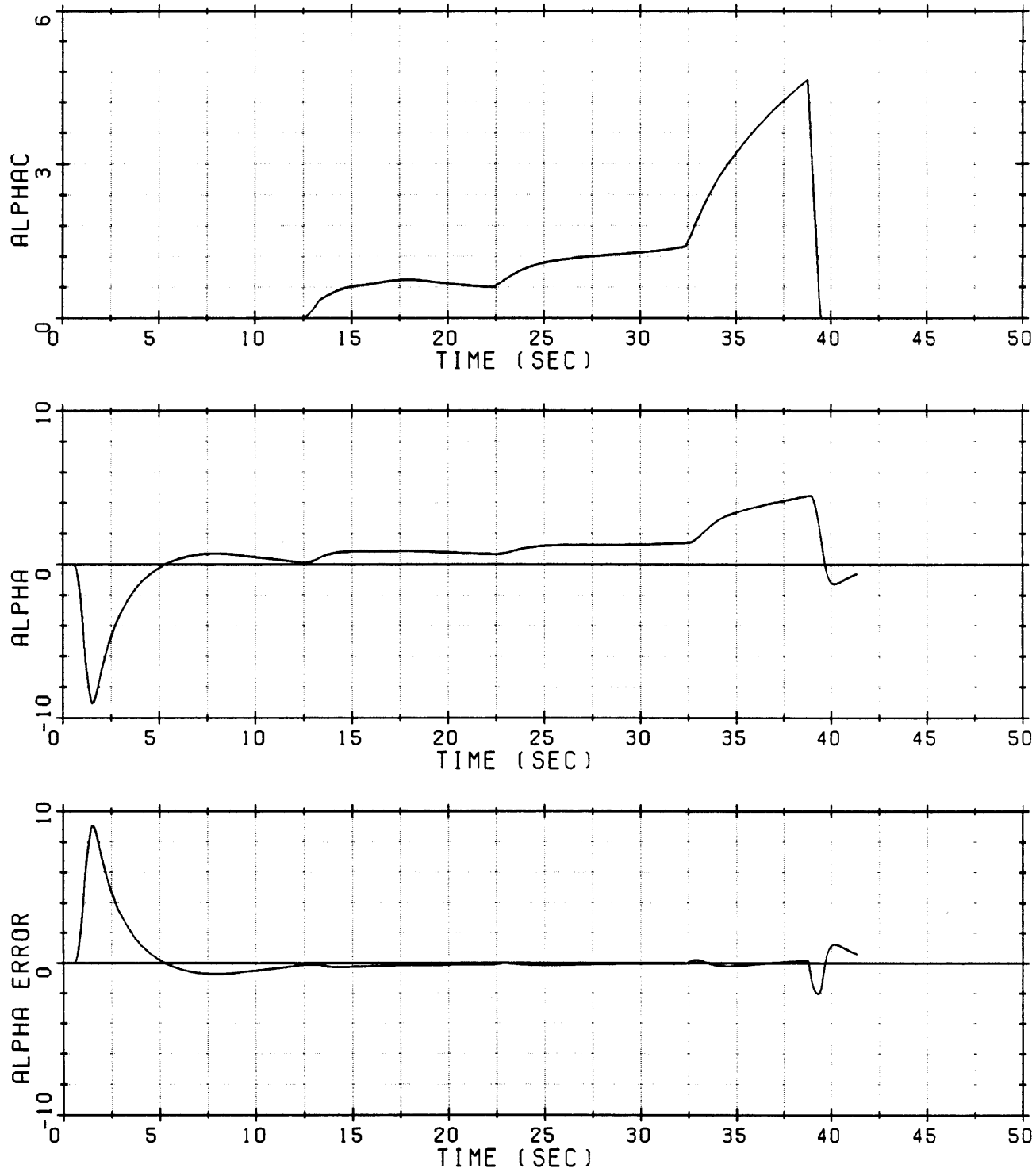

Figure 7-8. Predictive steering performance under a 10% thrust gradient with N_{steer} = 100. (Cont.)

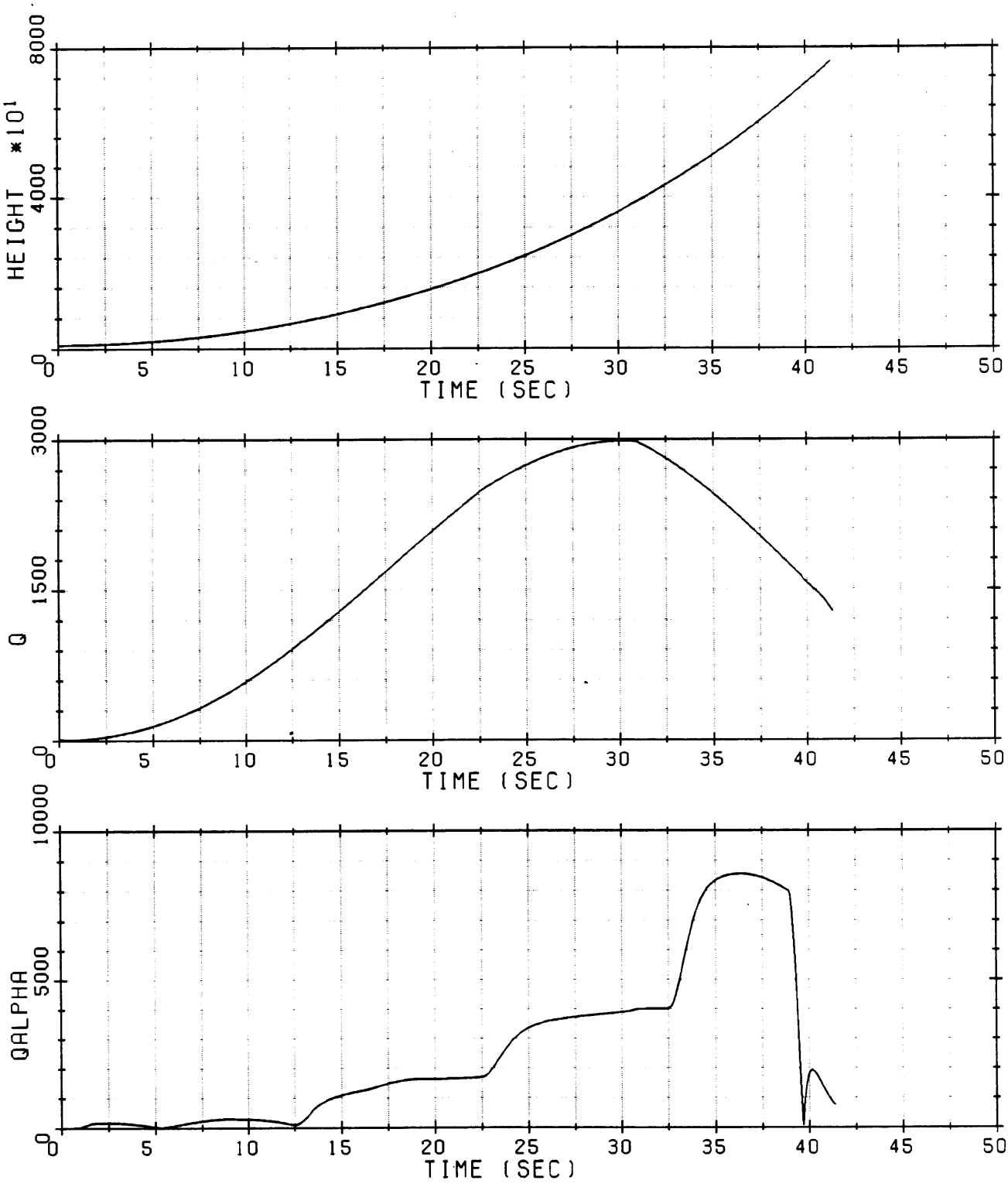

Figure 7-8. Predictive steering performance under a 10% thrust gradient with N_{steer} = 100. (Cont.)

9432 to 8562 deg lb/ft^2. However, this decrease is obtained at the expense of a large change in the terminal dynamic pressure error from 0.24 to 68.59 psf.

The curves for cases (1) and (2) indicate the possibility of achieving some smoothing of $q\alpha$ excursions at the expense of larger errors in terminal dynamic pressure. However, it is believed there are better ways of achieving further reductions in $q\alpha$ excursions than this particular approach. These other possibilities will be discussed in the final chapter.

7.8 Adaptability Performance

The primary purpose of predictive steering is to provide the boost system with the capability to adapt to off-nominal conditions that are impossible or inconvenient to represent in steering schemes based on prelaunch functionalizations. Therefore, the performance of the predictive steering method was investigated for off-nominal thrust profiles, different launch angles and winds. Also, effects on performance of assumed fixed percentage error in the axial force coefficient and atmospheric pressure were investigated. The effects of these off-nominal conditions are examined below, one at a time.

7.8.1 Off-nominal Thrust Profiles

The responses of predictive and logarithmic steering methods to off-nominal, constant thrust profiles and thrust gradients are compared in Tables 7-9, 7-10, respectively. It is seen that the predictive steering produces much lower errors in terminal dynamic pressure for unpredicted off-nominal thrust variations. However, in the case of the current implementaion of the predictive steering and of thrust, mass estimator good control of terminal dynamic pressure is achieved at the expense of larger $q\alpha$ values. Although revisions in the designs of the predictive steering and the thrust, mass estimator may be capable of

significantly reducing $q\alpha$ excursions, it is to be expected that some increase in $q\alpha$ activity is necessary to improve control of terminal q for off-nominal conditions. This should be true especially for thrust gradients which require a continual revision in γ-steering commands as the thrust changes, with resulting variations in commanded and actual angle of attack. Predictive steering system design alternatives could allow some degradation in control of terminal q in order to reduce the $q\alpha$ excursions. But in any case, it is clear that for unpredicted thrust variations the use of predictive steering will result in larger $q\alpha$ excursions than steering schemes based on prelaunch functionalization.

Table 7-9. Adaptability to off-nominal constant thrust profile.

Steering Method	Thrust Level	Max. $Q\alpha$ and (Time of Occurrence)		Q_{err}
Predictive	90%	6,957	(15.35)	-8.63
	110%	11,258	(14.71)	-9.26
Logarithmic	90%	1,523	(20.70)	-272.09
	110%	1,441	(17.08)	316.64

Table 7-10. Adaptability to thrust gradients.

Steering Method	Gradient (%)	Max. $Q\alpha$ and (Time of Occurrence)		Q_{err}
Predictive	5	5,447	(37.52)	-4.23
	10	9,406	(36.70)	0.35
Logarithmic	5	534	(21.82)	135.89
	10	419	(21.82)	278.45

The superiority of the predictive steering method in controlling terminal dynamic pressure are clear in these results. The logarithmic method does show significantly lower $q\alpha$ values but the terminal dynamic pressure errors are excessive. The values of $q\alpha$ for the logarithmic method are lower since the γ_c profile of logarithmic steering is smooth and does not have the corrective transients in γ_c produced by the predictive steering updates.

7.8.2 Launch Angles

The responses of predictive and logarithmic steering methods to off-nominal launch angles of 62° and 118° are compared in Table 7-11.

Table 7-11. Adaptability to off-nominal launch angles.

Steering Method	Thrust Level	Max. $Q\alpha$ and (Time of Occurrence)		Q_{err}
Predictive	62°	3,674	(37.65)	-9.77
	90°	3,730	(37.65)	-9.76
	118°	5,207	(15.20)	-9.99
Logarithmic	62°	606	(22.38)	3.79
	90°	647	(22.38)	-1.20
	118°	905	(20.70)	82.00

The ability of the predictive steering to adapt to off-nominal launch conditions is particularly evident for the worst case of the 118 degree launch, where the predictive steering produces a terminal q error of -9.99 psf, compared to the logarithmic steering system's error of 82 psf. As in previous simulation runs, the predictive steering accomplishes this better control of terminal q at the expense of a larger value of maximum $q\alpha$ product.

7.8.3 Added Effects of Winds

The effects of winds on the performance of the predictive and logarithmic steering methods for nominal and off-nominal launch conditions are compared in Table 7-12.

Table 7-12. Comparison of predictive vs logarithmic responses to different wind and launch conditions.

Launch χ	Winds	Steering Methods					
		Predictive			Logarithmic		
		Max. $Q\alpha$ and	Time of Occurrence	Q_{err}	Max. $Q\alpha$ and	Time of Occurrence	Q_{err}
90°	No	3730	(37.65)	-9.76	647	(22.38)	-1.20
	Tail	6305	(31.34)	-14.52	4391	(30.87)	-2.42
	Head	4992	(28.25)	-3.72	5022	(30.91)	-1.69
	XWind	4632	(37.69)	-2.18	2699	(28.99)	13.17
62°	No	3674	(37.65)	-9.77	606	(22.38)	3.79
	Tail	6303	(31.43)	-14.39	4442	(30.89)	3.20
	Head	4971	(28.29)	-3.76	4990	(30.93)	4.06
	XWind	4668	(37.69)	-2.15	2701	(29.03)	18.92
118°	No	5207	(15.20)	-9.99	905	(20.70)	82.00
	Tail	6334	(31.51)	-14.06	4261	(31.43)	81.03
	Head	5864	(15.23)	-4.03	5246	(31.42)	82.81
	XWind	5193	(15.20)	-1.53	2780	(29.52)	99.02

Table 7-12 shows that there is no major difference in the ability of the two steering schemes to control the terminal dynamic pressure q for the 90 degree nominal launch condition, with or without winds. In two cases the logarithmic steering produces the smaller error in terminal dynamic pressure, and in the other two cases the predictive steering produces the smaller error.

As pointed out in Chapter 4 winds can cause the actual dynamic pressure to differ appreciably from the estimated dynamic pressure which is used in the thrust-mass estimator. The estimated dynamic pressure, based on earth-relative velocity is used in estimating the axial aerodynamic force, which in turn is used in the estimation of thrust from measured axial acceleration. Any error in the dynamic pressure affects the estimated thrust directly and the estimated mass indirectly. Therefore, as shown in Chapter 4, head and tail winds, which produce larger changes in dynamic pressure than cross winds, cause correspondingly larger errors in estimated thrust and mass. This may be one reason why the predictive steering's terminal dynamic pressure is less for cross winds than for head and tail winds in all cases shown in Table 7-12.

7.8.4 Effects of Errors in Parameter Functionalizations

The response of the predictive steering method to errors in C_A and P functionalizations are given in Table 7-13. These results were obtained from the simulation runs performed in Chapter 4 where the thrust-mass estimator was evaluted.

Table 7-13. Effects of atmospheric estimate errors on predictive steering performance.

Environmental Variations		Max. $Q\alpha$ and (Time of Occurrence)		Q_{err}
CA/CA_{nom}	PA/PA_{nom}			
1.0	1.0	3730.22	(37.65)	-9.76
1.05	1.0	3289.74	(37.05)	-21.36
1.0	1.5	3548.04	(37.67)	-18.86

As can be seen in Table 7-13 these errors approximately double the Q_{err} value that was achieved for the no error case. This is not significant since it constitutes less than 2% of the desired dynamic pressure. There is no appreciable effect on the maximum $q\alpha$ value. Therefore, predictive steering can tolerate small errors in the functionalization of these parameters.

CHAPTER 8

CONCLUSIONS AND RECOMMENDATIONS

8.1 Conclusions

This study has revealed potential advantages and problems of predictive steering as applied to the first stage of a solid rocket booster that is targeting a specified dynamic pressure at staging. The main purpose of predictive steering is to provide greater flexibility in adapting to off-nominal inflight conditions. These conditions could be in the form of wind, thrust variations, off-nominal launch angles, etc. Simulation results revealed that the predictive steering offered no benefits over prelaunch functionalized steering in response to the wind disturbances investigated. However, simulations showed that the predictive steering adapted well to a 10% thrust gradient to control the dynamic pressure at staging to within 0.35 psf, as compared to 278.45 psf for a prelaunch functionalized steering. The use of predictive steering also showed significant improvement in the control of the terminal dynamic pressure when compared to a prelaunch functionalized steering method that does not specifically compensate for large changes in boost launch angle. For example, for a change in launch angle from a nominal 90° to a value of 118° the predictive steering method produced an error in terminal dynamic pressure of -10.00 psf, compared to 82.00 psf for the functionalized steering method based on a 90° launch angle.

The major problem encountered in applying the predictive steering approach came from the large sensitivity of the steering commands to the effects of errors in the estimated thrust. As a result of this sensi-

tivity even small errors in estimated thrust produced appreciable transient excursions in $q\alpha$. Although parceling out the predictive correction in the commanded flight path angle kept these excursions below the arbitrary design limit of 12,000 deg lb/ft^2 selected in this thesis, there appear to be a number of major modifications of both the steering and its associated thrust-mass estimator that could offer greater reductions in the $q\alpha$ excursions. These modifications are discussed below.

In general, the predictive steering method is superior to the fixed functionalized steering method in applications where flexibility is required in adapting to off-nominal flight conditions.

8.2 Recommendations

There are a number of possible revisions in the predictive steering and in the thrust-mass estimator employed by the predictive steering that might reduce transient excursions in $q\alpha$. Some of these revisions might also improve the control of terminal dynamic pressure, and others would reduce $q\alpha$ excursions at the expense of slightly larger errors in the terminal dynamic pressure.

Four possible revisions of the thrust-mass estimator are suggested for future study:

First, the estimated angle of attack might be utilized as follows to improve the estimated dynamic pressure. Assuming that the wind is nearly horizontal, the wind velocity vector can be deduced approximately from the difference between the estimated angle of attack and the computed angle of attack with respect to earth-relative velocity. This estimated wind velocity can then be subtracted from the earthrelative vehicle velocity to obtain the air-relative vehicle velocity, which can be squared and multiplied by estimated air mass density to obtain a better estimate of dynamic pressure. This revision might reduce $q\alpha$ excursions and terminal q errors when there are major wind disturbances. Of course a direct aerodynamic sensing of the dynamic pressure could be used in lieu of this improved estimation approach.

The second revision would be to divide the estimated thrust based on x-axis acceleration by the cosine of the estimated average engine nozzle deflection over each steering cycle. The benefits of this correction for effects of engine deflections could be small except possibly under some launch conditions or wind conditions that could produce large deflections.

The third suggested revision would be to introduce some smoothing into the thrust-mass estimator. This could be done by comparing the estimated thrust presently produced with the nominal thrust computed from the estimated mass. This thrust difference could then be passed through a low-pass filter and then added to the computed nominal thrust value. This filtered estimate may be of some value in reducing transient fluctuations in thrust estimation errors, and the accompanying transient in $q\alpha$ excursions. However, the filtering of gamma command updates of the predictive steering might accomplish similar results. Since the response of estimated mass to transient errors in estimated thrust is inherently slow, the unfiltered thrust estimation might still be used for mass estimation.

The fourth suggested revision of the thrust-mass estimator would be to suspend updates of the estimated thrust when passing through the unit Mach number where the present functionalization of C_A is not accurate. An alternative to this revision would be to improve the functionalization of C_A in this Mach number region, but since the vehicle spends very little time in the vicinity of the critical Mach number, temporarily suspending further updates of the estimated thrust might be an acceptable solution.

There are probably a great number of ways to revise the predictive steering itself to reduce the transient excurions in $q\alpha$ resulting from thrust estimation errors. One of these is to change the basic method of altering the boost trajectory to meet desired end conditions (which in this thesis was a desired terminal dynamic pressure). For example,

instead of computing a new gamma value that would produce a zero-angle-of-attack trajectory leading to the desired end state, the predictive steering simulation could compute the small perturbation in the gamma rate from the gravity turn value that would achieve the desired end state. This alternative approach, which could include limiting or even shaping of the gamma rate perturbation, would spread out the effects of any given thrust estimation error over the remaining trajectory, possibly resulting in reduction in transient $q\alpha$ excursions. This and other approaches might be considered in an effort to achieve an optimum trade-off between maximum $q\alpha$ value and maximum deviation from the desired end state resulting from worst case off-nominal conditions.

LIST OF REFERENCES

1. Bonnice, W. F., Steering of a Boost Vehicle to a Desired Flight Path Angle Trajectory Using Angle of Attack Control, Master of Science Thesis, 1983, Massachusetts Institute of Technology, C. S. Draper Laboratory Report CSDL-T-802.

2. Fader, L. R., Altitude Steering of a Boost Vehicle, Master of Science Thesis, 1985, Massachusetts Institute of Technology, C.S. Draper Laboratory Report CSDL-T-875.

3. Dailey, J. F., Steering and Roll Rate Control of a Boost Vehicle in the Atmosphere, Master of Science Thesis, 1985, Massachusetts Institute of Technology, C. S. Draper Laboratory Report CSDL-T-895

4. Whitaker, H. P., Autonetics Kick Maneuver, Oct 3, 1985, Draper Intra-Lab Memo, Memo # FC-85-2.

5. Simmons, G. F., Differential Equations with Applications and Historical Notes, McGraw-Hill, Inc.(1972)

6. Leondes, C. T., Guidance and Control of Aerospace Vehicles, McGraw-Hill, Inc. (1963)

APPENDIX A

DERIVATION OF ESTIMATED THRUST, MASS, AND TIME RELATIONSHIPS

The nominal vacuum thrust profile can be altered to simulate off-nominal profiles that give the same total impulse and burnout mass, using relationshps that are derived below. As mentioned previously, specific impulse and gravity are assumed constant.

The data for simulating a given vacuum thrust profile is assumed to be provided in terms of a stored table of values of thrust* and mass for a given set of discrete times. The mass values in this table are derived from the thrust and time values assuming that the thrust varies linearly between time points and that the mass flow rate is given by

$$\dot{m} = \frac{-F}{I_{sp}\, g} \qquad \text{(A.1)}$$

where

F = instantaneous vacuum thrust level

I_{sp} = constant specific impulse

g = gravitational constant

The discrete thrust, mass, time values yield simulated profiles as shown in Figure A-1 for the nominal thrust case.

*All thrust values referred to in this Appendix are vacuum thrust values.

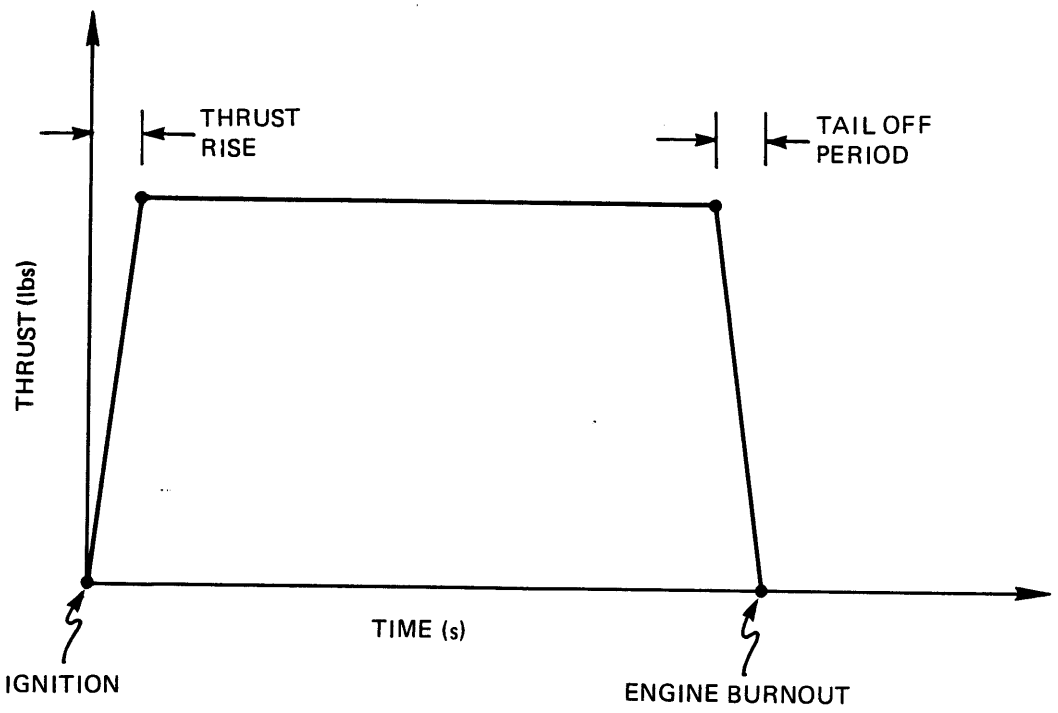

Figure A-1a. Thrust vs time profile of the nominal thrust profile. (Not to scale.)

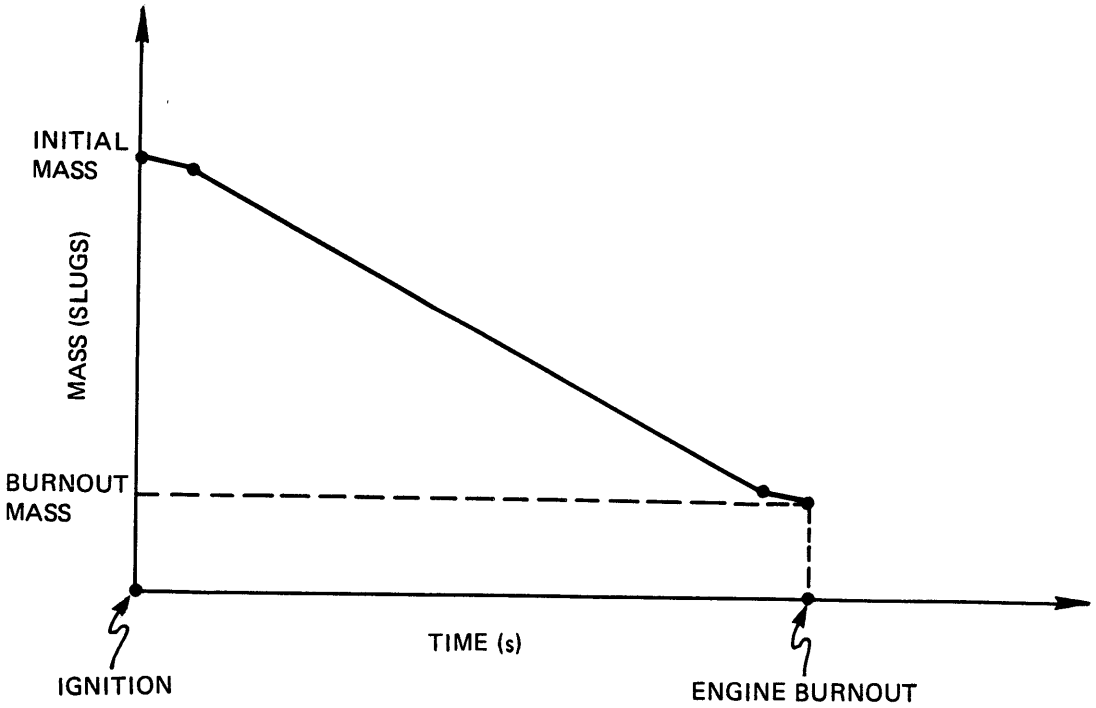

Figure A-1b. Mass vs time profile of the nominal thrust profile. (Not to scale.)

The derivation of expressions for the mass points in terms of thrust, time values is as follows: First, integrating Eq. (A.1) from t_{i-1} to t_i yields the change in mass during that interval.

$$\int_{i-1}^{i} m\,dt = m_i - m_{i-1} = \frac{-1}{I_{sp}\,g} \int_{i-1}^{i} F\,dt \qquad (A.2)$$

For the assumed linearly varying thrust, the thrust impulse during this interval is the average thrust value during the interval multiplied by the time interval

$$\int_{i-1}^{i} F\,dt = 1/2(F_i + F_{i-1})(t_i - t_{i-1}) \qquad (A.3)$$

Substituting Eq. (A.3) into Eq. (A.2) yields

$$m_i - m_{i-1} = \left(\frac{-1}{2\,I_{sp}\,g}\right)(F_i + F_{i-1})(t_i - t_{i-1}) \qquad (A.4)$$

Which can be rearranged to

$$m_i = m_{i-1} - \left(\frac{-1}{2\,I_{sp}\,g}\right)(F_i + F_{i-1})(t_i - t_{i-1}) \qquad (A.5)$$

Eq. (A.5) gives the relationship that is utilized to compute mass values from tabulated thrust and time values.

The stored values of thrust and mass versus discrete times are modified in the simulation as follows to describe the effects of (1) a higher or lower than nominal rocket grain temperature, resulting in correspondingly higher or lower thrust and (2) a temperature gradient in the rocket grain which results in a thrust level which varies linearly with expended mass. The following relationships treat the stored sets of n discrete time, thrust, and mass values as three n-dimensional vectors.

First, in the case of a uniform grain temperature that is different from the nominal temperature, a multiplicative factor, KBURN2, is introduced to scale the entire nominal thrust profile, represented by the vector $\overline{F}_{nominal}$ to obtain the off-nominal vector,

$$\overline{F}_{off\text{-}nominal} = KBURN2\ \overline{F}_{nominal} \tag{A.6}$$

Since the thrust vector has been modified the time vector must also be modified to retain the same total impulse. Elements of the new time vector can be computed from the following relationship obtained from Eq. (A.5)

$$t_i = t_{i-1} - 2\ g\ I_{sp}(m_i - m_{i-1})/(F_{i-1} + F_i) \tag{A.7}$$

Second, in the case of a temperature gradient the representation of a thrust versus mass dependency is simplified by

(1) Assuming that the original discrete thrust values at each original mass value is multiplied by a factor that increases linearly with expended mass and

(2) Assuming that the thrust level varies linearly with time between the modified discrete values.

According to the assumption of (1), the new thrust value $\bar{F}_{i_{grad}}$ for each mass values m_i is computed as follows for a thrust factor that varies from an initial value of unity to a final value of 1 + DELK.

$$F_{i_{grad}} = F_{i_{nom}} \left\{1 + DELK(m_0 - m_i)/(m_0 - m_f)\right\} \tag{A.8}$$

where:

$F_{i_{nom}}$ = current nominal thrust profile

m_0 = initial vehicle mass

m_i = current vehicle mass

m_f = vehicle burnout mass

Once the new thrust values have been obtained from the above relationship, the assumption of (2) allows the new discrete time values to be obtained from Eq. (A.7).

APPENDIX B

ZERO ANGLE OF ATTACK TRAJECTORY EQUATIONS OF MOTION

The zero angle of attack, "gravity turn" trajectory is used because it yields minimal aerodynamic forces normal to the vehicle. These normal forces (in combination with the normal component of thrust required to counter the torque produced by the aerodynamic normal force) can cause the vehicle to have large bending moments. For an ideal zero angle of attack trajectory in a no-wind environment, the vehicle x-body axis remains coincident with the vehicle earth-relative velocity vector throughout the trajectory as illustrated in Figure B-1. In this case, the aerodynamic component of force normal to the x-body axis (and the velocity vector) is zero. The thrust vector deflection is controlled by the angle of attack control loop to produce the small component of force normal to the x-body axis sufficient to maintain the vehicle attitude rate equal to the flight path angle rate, $\dot{\gamma}$. The normal component of force is negligible, compared to the gravity force and will be assumed zero in the derivation that follows.

To derive the equations of motion, it is convenient to define two coordinate systems:

(1) An earth-centered system with y-axis perpendicular to the trajectory plane.

(2) A "velocity vector" system with x-axis along the velocity vector, y-axis perpendicular to the trajectory plane, and z-axis formed from the cross product of the x and y axes.

The systems are shown in Figure B-2. For the purposes of this derivation, the motion of the earth in inertial space is assumed to have

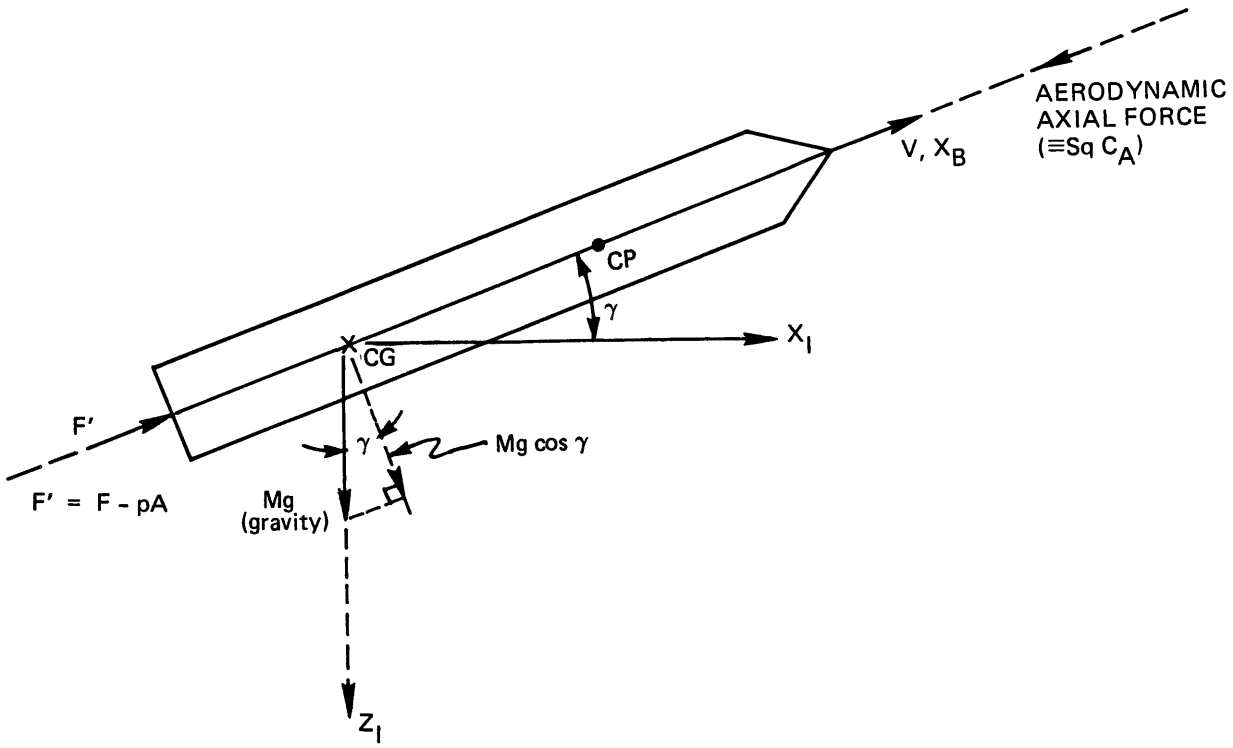

Figure B-1. Pitch plane forces for a zero angle of attack trajectory.

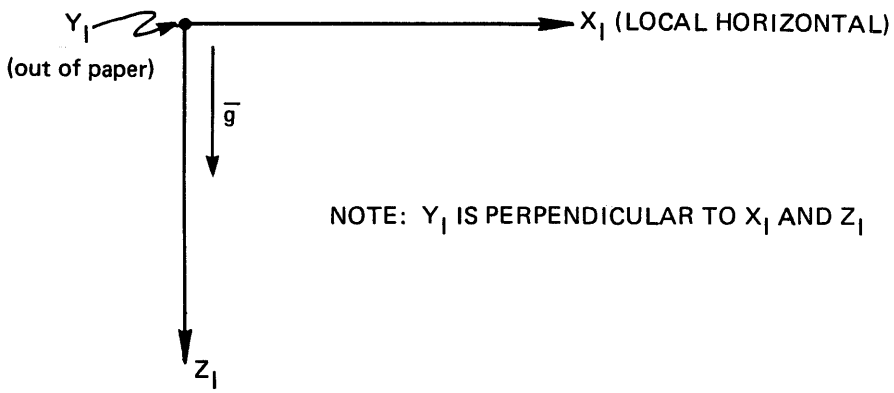

Figure B-2a. Earth-centered reference frame.

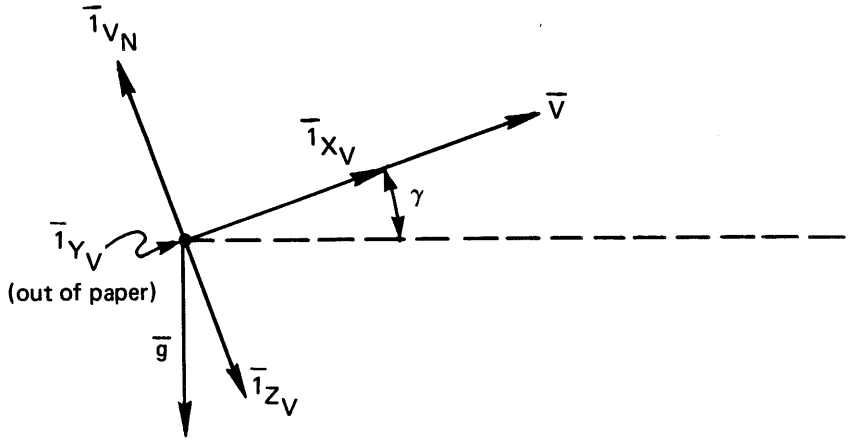

NOTE: THE $\bar{1}_{Y_V}$ VECTOR IS DEFINED TO BE PERPENDICULAR TO THE $\bar{V}$ AND $\bar{g}$ VECTORS.

Figure B-2b. Velocity vector frame.

a negligible effect on the acceleration of the vehicle in inertial space. The earth-centered system, therefore, is defined to be the reference inertial system.

The angular rotation rate of the velocity vector system with respect to the earth-centered reference system is a vector of magnitude $|\dot{\gamma}|$ which for a positive $\dot{\gamma}$ in the pitch plane lies along the positive $\bar{1}_{y_v}$ axis. The equations of motion of the vehicle c.g. that determine the trajectory are obtained by equating the following two expressions for linear acceleration of the c.g.

(1) The acceleration vector obtained by taking the derivative (with respect to the earth-centered reference system) of the velocity vector.

(2) The acceleration vector obtained by dividing the net force vector by mass. The forces acting on the c.g. consist of thrust, aerodynamic axial force and gravity.

The derivative of the pitch-plane velocity taken with respect to the earth-centered reference system is given by the coriolis relationship

$$\bar{a} = \frac{d}{dt}\Big]_E \bar{V} = \frac{d}{dt}\Big]_V \bar{V} + (\dot{\gamma}\, \bar{1}_{y_v}) \times (V\, \bar{1}_{x_v}) \qquad (B.1)$$

where the subscripts E and V indicate that derivatives are taken with respect to the earth-centered and velocity-vector system respectively.

Therefore,

$$\bar{a} = \dot{V}\, \bar{1}_{x_v} + \dot{\gamma}\ V\, \bar{1}_{z_v} \qquad (B.2)$$

or

$$\bar{a} = \dot{V}\, \bar{1}_{x_v} + \dot{\gamma}\, V\, \bar{1}_{v_n} \qquad (B.3)$$

where as shown in Figure B-1, $\bar{1}_{v_n}$ is the unit vector normal to the velocity vector in the direction opposite to $\bar{1}_z$.

The acceleration vector obtained by dividing the net force vector by mass is given by the expression

$$\bar{a} = \frac{1}{m} \{(F' \cos \delta - S\, q\, C_A)\, \bar{1}_{x_v} - (F' \sin \delta + g \cos \gamma)\, \bar{1}_{v_n}\} \qquad (B.4)$$

In this expression, the thrust F' is equal to the vacuum thrust F corrected for the effects of the atmospheric pressure p acting on the nozzle and A:

$$F' = F - pA \qquad (B.5)$$

As indicated in the beginning of this appendix, the term (F' sinδ) is negligible compared to (mg cosγ)for the zero angle of attack trajectory and is assumed to be zero. Also, (F' cosδ) can be approximated by F'.

Therefore,

$$\bar{a} = \frac{1}{m} \{(F' - S\ q\ C_A)\ \bar{i}_x - m\ g\ \cos\gamma\ \bar{i}_v \} \tag{B.6}$$

Equating the coefficients of $\bar{i}_{x_v}$ in Eq. (B.3) and (B.6)

$$\dot{V} = \frac{1}{m} (F - S\ q\ C_A) \tag{B.7}$$

Equating the coefficients of $\bar{i}_{v_n}$ in Eq. (B.3) and (B.6)

$$\dot{\gamma}\ V = -g\ \cos\gamma \tag{B.8}$$

Therefore,

$$\dot{\gamma} = -g\ \cos\gamma/V \tag{B.9}$$

Eq. (B.7) and (B.9) are the equations of motion of the zero angle of attack trajectory.

The predictive simulation utilizes two additional equations: First is the equation relating the time rate of change of mass to vacuum thrust,

$$\dot{m} = -\frac{F}{I_{sp}\ g} \tag{B.10}$$

where I_{sp} is the specific impulse, assumed constant over the entire boost phase. Second is the equation for the rate of change of the altitude H,

$$\dot{H} = V \sin\gamma \tag{B.11}$$

The altitude H obtained by integration of Eq. (B.11) is used to compute the atmospheric pressure p and the atmospheric mass density ρ. The computed atmospheric pressure p, in turn, is used to compensate the vacuum thrust for the effects of atmospheric pressure in computing the thrust F as shown in Chapter 4. In addition, the mass density ρ is used with the velocity V to compute the dynamic pressure,

$$q = \frac{1}{2} \rho V^2 \tag{B.12}$$

Relationships for functionalizing p and ρ in terms of H and C_A in terms of V are described in Chapter 4.

The predictive steering simulation employs one of the three numerical integration algorithms described by Eq.s (7.2), (7.3), and (7.4) to integrate Eq.s (B.7), (B.9), (B.10), and (B.11), utilizing relationships of Chapter 4 to compute p, ρ, F and C_A, using Eq. (B.5) to compute F'; and employing Eq. (B.12) to compute the terminal dynamic pressure.

APPENDIX C

DERIVATION OF IMU CENTRIPETAL ACCELERATION

The general expression of the centripetal acceleration of the IMU about the CG point is

$$A_{cent} = \ell_{imu} \, \Omega^2_{avg} \qquad (C.1)$$

where Ω_{avg} = average angular rate over a steering cycle.

In this derivation the angular rate is assumed to vary linearly between steering update times as pictured in Figure C-1.

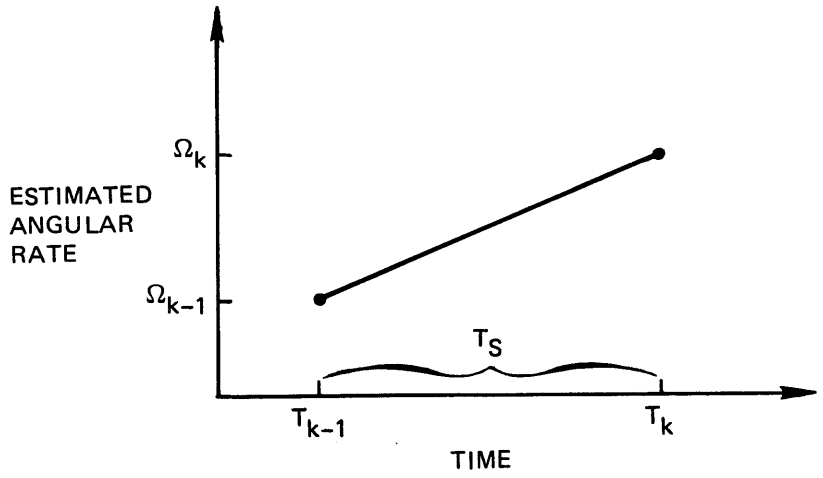

Figure C-1. Illustrating a linearly varying angular rate between k-1 and k sample points.

The angular rate at any time between steering update times is

$$\Omega = \Omega_{k-1} + \left[\frac{\Omega_k - \Omega_{k-1}}{T_s}\right] t \qquad \text{(C.2)}$$

where

Ω_{k-1}, Ω_k = the estimated angular rates at (k-1)st and kth steering sampling times.

t = arbitrary time between the (k-1)st and kth sampling times measured from the (k-1)st sampling times.

T_s = steering interval between the (k-1)st and kth sampling time

Squaring Eq. (C.2) yields,

$$\Omega^2 = \Omega_{k-1}^2 + 2\left[\frac{\Omega_k - \Omega_{k-1}}{T_s}\right] \Omega_{k-1}\, t + \left[\frac{\Omega_k^2 - 2\,\Omega_k\,\Omega_{k-1} + \Omega_{k-1}^2}{T_s^2}\right] t^2 \qquad \text{(C.3)}$$

The average squared angular rate is then obtained by integrating Eq.(C.3):

$$\Omega_{avg}^2 = \frac{1}{T_s}\int_0^{T_s} \Omega^2\, dt = \frac{1}{T_s}\int_0^{T_s} \left\{\Omega_{k-1}^2 + 2\left[\frac{\Omega_k - \Omega_{k-1}}{T_s}\right] \Omega_{k-1}\, t + \left[\frac{\Omega_k^2 - 2\,\Omega_{k-1}\,\Omega_k + \Omega_{k-1}^2}{T_s^2}\right] t^2\right\} dt$$

$$= \frac{1}{3}\left[\Omega_{k-1}^2 + \Omega_{k-1}\,\Omega_k + \Omega_k^2\right] \qquad \text{(C.4)}$$

APPENDIX D

DERIVATION OF THE RELATIONSHIP BETWEEN FLIGHT PATH ANGLE RATE, $\dot{\gamma}$ AND ANGLE OF ATTACK, α

The steering loop is designed to take advantage of an approximate proportionality between the rate of change of the flight path angle, $\dot{\gamma}$, and the angle of attack α:

$$\dot{\gamma} \simeq \frac{\alpha}{K'_{st}} \tag{D.1}$$

where K'_{st} is a function of time-varying vehicle parameters. The proportionality constant K'_{st} is employed as a factor in computing the commanded angle of attack as illustrated in the approximate model of the steering loop in Figure D-1. The effect of this use of K'_{st} is to produce a steering loop whose dynamic characteristics are nearly constant over the entire boost phase, as represented by the simplified steering loop model in Figure D-2.

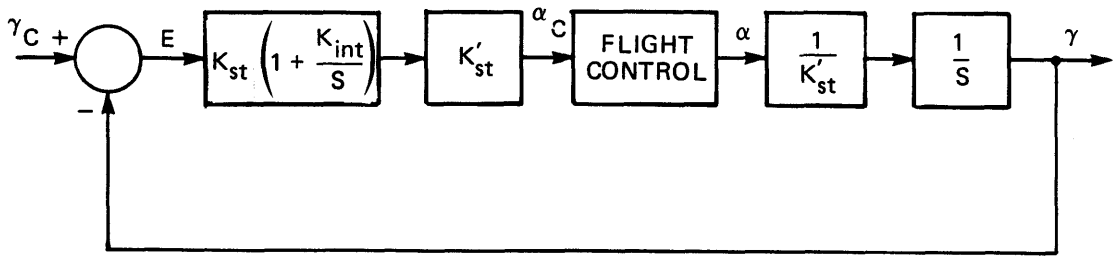

Figure D-1. Approximate steering loop model.

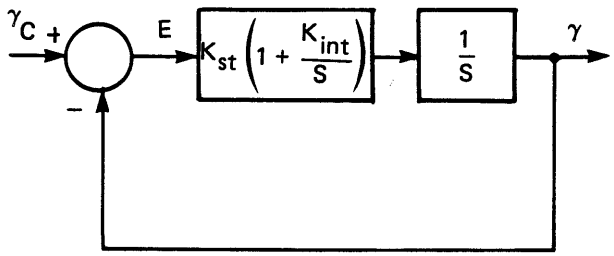

Figure D-2. Simplified steering loop model.

To derive the relationship for K'_{st}, it is convenient, first, to express the relationship between $\dot{\gamma}$ and A_{N_V}, where A_{N_V} is the component of vehicle acceleration normal to the vehicle earth-relative velocity vector produced by aerodynamic and thrust forces:

$$A_{N_V} - g \cos\gamma = V_e \dot{\gamma} \tag{D.2}$$

The acceleration A_{N_V} can also be computed as a function of the thrust and aerodynamic forces by expressing the acceleration produced by these forces in the vehicle coordinate system and then resolving this acceleration into the direction normal to the earth relative velocity vector (see Figure D-3). In the vehicle body coordinate system the acceleration produced by thrust and aerodynamic forces is given by the vector,

$$\bar{A}_b = \frac{1}{m} \begin{bmatrix} (F' \cos\delta - F_a) \\ 0 \\ (F' \sin\delta - F_n) \end{bmatrix} \tag{D.3}$$

where F_a and F_n are the axial and normal aerodynamic forces, respectively, and where F' is the vehicle thrust, obtained by compensating the vacuum thrust F for atmospheric effects:

$$F' = F - pA$$

The component of $\bar{A}_{NV}$ in the direction normal to the earth relative velocity vector is obtained by using $\sin\alpha_{nw}$ and $\cos\alpha_{nw}$ to transform $\bar{A}_b$:

$$\begin{aligned} A_{N_V} &= \frac{1}{m} \left\{ \left(F' \cos\delta - F_a\right) \sin\alpha_{nw} - \left(F' \sin\delta - F_n\right) \cos\alpha_{nw} \right\} \\ &= \frac{1}{m} \left\{ F_n \cos\alpha_{nw} - F_a \sin\alpha_{nw} + F' \sin(\alpha_{nw} - \delta) \right\} \end{aligned} \qquad \text{(D.4)}$$

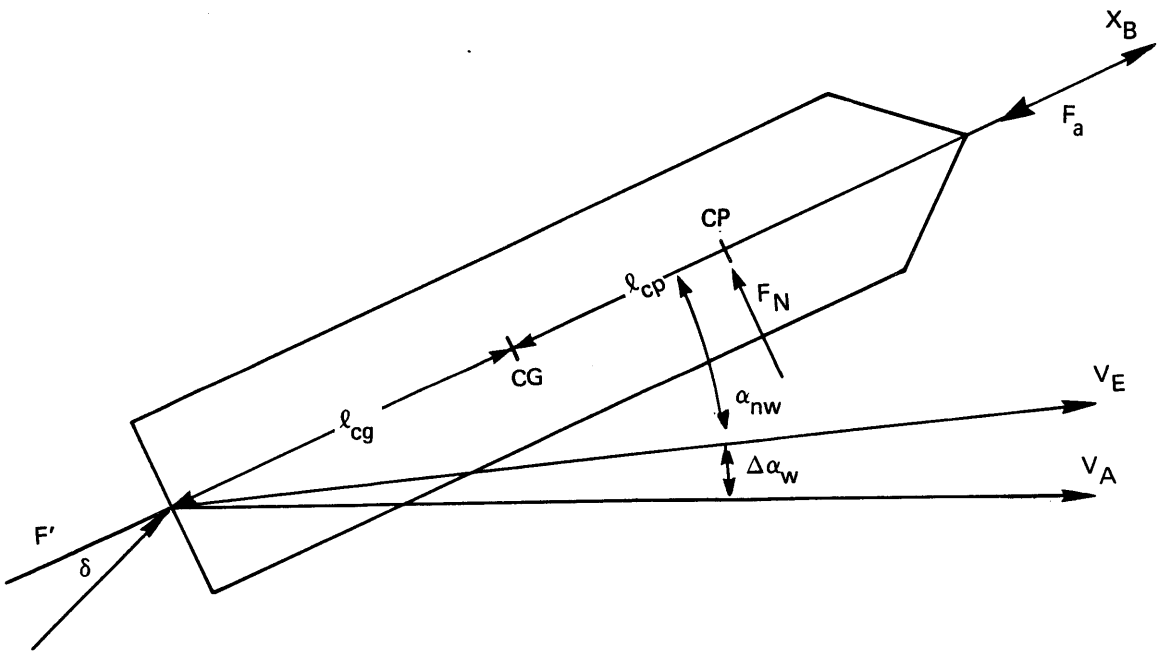

Figure D-3. Definition of force, velocity and angle of attack variables.

Using small angle assumptions,

$$A_{N_V} = \frac{1}{m} \left\{F_n - F_a \alpha_{nw} + F'(\alpha_{nw} - \delta)\right\}$$

$$= \frac{1}{m} \left\{S\ q\ C_n - S\ q\ C_a\ \alpha_{nw} + F'(\alpha_{nw} - \delta)\right\} \qquad (D.5)$$

For small values of angle of attack with respect to the air-relative velocity vector, the aerodynamic coefficient, C_n, can be approximated by:

$$C_n \approx C_{n_\alpha} (\alpha_{nw} + \Delta\alpha_w) \qquad (D.6)$$

Substituting this expression into Eq. (D.5),

$$A_{N_V} = \frac{1}{m} \left\{\left[S\ q\ C_{n_\alpha} (\alpha_{nw} + \Delta\alpha_w) - S\ q\ C_a \alpha_{nw} + F'(\alpha_{nw} - \delta)\right\} \qquad (D.7)$$

Next, the nozzle deflection, δ, in Eq. (D.7) can be related to α_{nw} and $\Delta\alpha_w$ if it is assumed that the vehicle is in a "steady state" condition in which the vehicle angular acceleration is zero. In this case, the net torque produced by the thrust and aerodynamic forces is zero. Therefore,

$$F_n\ \ell_{cp} + F' \sin\delta\ \ell_{cg} = 0 \qquad (D.8)$$

Substituting into Eq. (D.8) the relationships

$$F_n = S\ q\ C_n \approx S\ q\ C_{n_\alpha} (\alpha_{nw} + \Delta\alpha_w) \qquad (D.9)$$

$$\sin\delta \approx \delta \qquad (D.10)$$

and solving for δ,

$$\delta = - \frac{S\ q\ C_{n_\alpha}\ (\alpha_{nw} + \Delta\alpha_w)\ \ell_{cp}}{F'\ \ell_{cg}} \tag{D.11}$$

Substituting this expression into Eq. (D.7) and collecting terms in α_{nw} and $\Delta\alpha_w$,

$$A_{N_V} = \frac{1}{m} \left\{ \left[S\ q\ (C_{n_\alpha} - C_a) + F' + \frac{S\ q\ C_{n_\alpha}\ \ell_{cp}}{\ell_{cg}} \right] \alpha_{nw} + S\ q\ C_{n_\alpha} \left(1 + \frac{\ell_{cp}}{\ell_{cg}}\right) \Delta\alpha_w \right\} \tag{D.12}$$

Then, substituting into Eq. (D.12) the relationship

$$\alpha_{nw} = \alpha - \Delta\alpha_w \tag{D.13}$$

the expression for A_{N_V} becomes

$$A_{N_V} = \frac{1}{m} \left\{ \left[S\ q\ (C_{n_\alpha} - C_a) + F' + \frac{S\ q\ C_{n_\alpha}\ \ell_{cp}}{\ell_{cg}} \right] \alpha + (S\ q\ C_a - F')\ \Delta\alpha_w \right\} \tag{D.14}$$

Substituting Eq. (D.14) into Eq. (D.2) and solving for $\dot{\gamma}$,

$$\dot{\gamma} = \frac{1}{m\ V_e} \left[S\ q\ (C_{n_\alpha} - C_a) + F' + \frac{S\ q\ C_{n_\alpha}\ \ell_{cp}}{\ell_{cg}} \right] \alpha + \frac{1}{m\ V_e} (S\ q\ C_a - F')\ \Delta\alpha_w - \frac{g}{V_e} \cos\gamma \tag{D.15}$$

In general, the wind contribution to angle of attack, $\Delta\alpha_w$, is not known. Therefore, Eq. (D.15) cannot be used to determine a precise relationship between $\dot{\gamma}$ and α. However, for stability analysis one is interested in the effects on $\dot{\gamma}$ of control-induced variations in α. For this purpose one may omit the $\Delta\alpha_w$ term and consider only the deviations in $\dot{\gamma}$ and α from a quasi steady state condition, neglecting the contributions of the slow variations in the terms $\frac{1}{m V_e}(S\ q\ C_a - F')\ \Delta\alpha_w$ and $\frac{g}{V_e}\cos\gamma$. Employing these approximations, the deviations $\Delta\dot{\gamma}$ and $\Delta\alpha$ from a given trajectory resulting from control actions can be approximated by the expression

$$\Delta\dot{\gamma} = \frac{1}{m V_e}\left[S\ q\ \left(C_{n_\alpha} - C_a\right) + F' + \frac{S\ q\ C_{n_\alpha}\ \ell_{cp}}{\ell_{cg}}\right]\Delta\alpha \qquad \text{(D.16)}$$

which can be expressed as

$$\Delta\dot{\gamma} = (1/K'_{st})\ \Delta\alpha$$

where

$$K'_{st} = \frac{m V_e}{\left[S\ q\ \left(C_{n_\alpha} - C_a\right) + F' + \frac{S\ q\ C_{n_\alpha}\ \ell_{cp}}{\ell_{cg}}\right]} \qquad \text{(D.17)}$$